

UNCLASSIFIED.

~~PROSPECTIVE NASA CR~~

ANALYSIS OF THREE-COMPONENT AEROMAGNETIC DATA

by

B.K. Bhattacharyya, Principal Investigator

Lei-Kuang Leu

Distribution of this report is provided in the interest of information exchange. Responsibility for the contents resides in the authors or the organization that prepared it.

Final report

July 1, 1972 - June 30, 1973

Prepared under Contract No. ~~UCB-3519~~

NAS 2-7159

by

REGENTS OF THE UNIVERSITY OF CALIFORNIA  
BERKELEY, CALIFORNIA

for

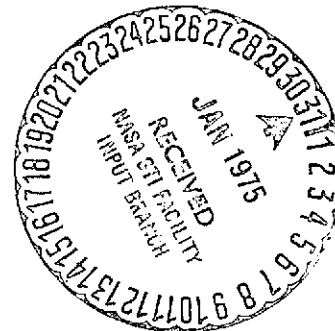
AMES RESEARCH CENTER

NATIONAL AERONAUTICS AND SPACE ADMINISTRATION

N75-15229

(NASA-CR-137593) ANALYSIS OF  
THREE-COMPONENT AEROMAGNETIC DATA Final  
Report, 1 Jul. 1972 - 30 Jun. 1973  
(California Univ.) 92 p HC \$4.75 CSCL 08N

Unclass  
D3/46 08263



### Introduction

The objective of this report is to evaluate quantitatively the relative merit of three-component magnetic data over the total field measurements. At the present time, most magnetic surveys conducted for mapping subsurface geological structures are limited to measurements of the total magnetic field. This field is composed of the main field of the earth and the anomalous field caused by crustal magnetized bodies. Since the anomalous field is normally much less in magnitude than the earth's main field, for all practical purposes it can be assumed to be measured in the direction of the main field. This kind of observation with total field magnetometer does not contain any information regarding change in direction of the anomalous field in space. This limitation of the data introduces ambiguities in the results of interpretation and does not permit a unique determination of any parameter of the causative bodies without additional geological and geophysical information. Recent theoretical studies (Bhattacharyya, 1967) indicate that if the three-component magnetic data are available, the direction and magnitude of the magnetization vector can be computed without any assumption on the geometry and orientation of the causative body.

Measurements of one single component of the magnetic field anomaly over a horizontal plane contain information about the other components. The possibility of deriving three-component data from one-component measurements was first suggested by Vestine and Davids (1945). Hughes and Pondrom (1947) showed that the vertical and horizontal anomalies can be obtained as surface integrals from the measurement of the total field anomaly. In practice, the development of a numerical method for obtaining three-component magnetic data

from measurements of one single magnetic component is based on transformation of the total-field data in the frequency domain. A method for expressing the data in terms of double Fourier series has been developed (Bhattacharyya, 1965). With the help of this method, Lourenco (1972) and Lourenco and Morrison (1973) have computed the three-components of the magnetic field from the total field data obtained over a finite area. However, the accuracy of the calculated field components depends not only on the numerical method employed but also on the assumed direction of the geomagnetic field. It is very interesting to study the effectiveness of the calculated field components in the computation of the parameters of bodies causing magnetic anomalies.

In the quantitative treatment of magnetic data, the first and second derivatives are usually evaluated. Second derivative maps are found to be very useful in approximately delineating the boundary of the causative body. The objective of the present study is to evaluate the relative merit of three-component magnetic data over total-field measurements. Estimates are to be made of the errors introduced in computing field components from total field data. The real test of the relative merit of the two sets of data is provided when they are used to determine the parameters of disturbing bodies.

In chapter 1 the numerical method and results of obtaining three field components from total field measurements, using double Fourier series expansion, are presented. The horizontal first and second derivatives of each component are obtained by the method of bicubic spline interpolation and they are also discussed in the first chapter. The total field data for this study are computed over a finite area with a  $64 \times 64$  grid points, using a theoretical model of infinite prism. The field components and their derivatives, as calculated with the total field data, are compared with the exact values and

the shortcomings of the use of the total-field data are reported.

In the second chapter of this report the expressions for moments of the anomalous field components over a finite area are given. The magnitude and direction of the magnetization vector are evaluated with the help of moments of computed and exact three-component magnetic data for various prismatic bodies. The results of calculating the magnitude and direction of the magnetization vector, using both computed and exact field component data, are discussed in this report.

The study presented in this report shows that the vertical component of the magnetic field calculated from total field observations is more accurate at higher geomagnetic latitudes than at lower latitudes. The opposite is the case for the horizontal components. The errors in determining the magnetization vector directions with the help of calculated field components are significantly large over most of the range of variation of declination and inclination of the vector. This observation demonstrates conclusively the practical limitations of computing field components from total field data even under the best of conditions. The errors, as noted before, will definitely be larger for actual field observations.

## CHAPTER 1

MAGNETIC FIELD COMPONENTS AND THEIR DERIVATIVES1. Method for computing field components

A method for computing three field components from the total magnetic field observations as described by Lourenco (1972) and Lourenco and Morrison (1973) is presented in this section. Let us adopt a Cartesian coordinate system such that in the plane of measurement the x-axis points northward, the y-axis eastward and the z-axis vertically downward, as shown in Figure 1.

The magnitude of the anomalous magnetic field vector is generally very small compared to the geomagnetic field vector. This is why the direction of the resultant of the two vectors is practically invariant over the area of measurement and is assumed to be the same as that of the geomagnetic field. If  $\Delta V$  represents the anomalous magnetic potential, at all points of free space it satisfies Laplace's equation:

$$(1-1) \quad \nabla^2 (\Delta V) = 0.$$

The total intensity anomaly in the direction of the geomagnetic field is given by the negative derivative of the anomalous magnetic potential:

$$(1-2) \quad \Delta T = - \frac{\partial}{\partial t} (\Delta V)$$

where  $\bar{t}$  is the unit vector in the direction of the geomagnetic field.

The field components are given by the following equations:

$$(1-3) \quad H_x = - \frac{\partial}{\partial x} (\Delta V)$$

$$(1-4) \quad H_y = - \frac{\partial}{\partial y} (\Delta V)$$

$$(1-5) \quad H_z = - \frac{\partial}{\partial z} (\Delta V)$$

where  $H_x$ ,  $H_y$  and  $H_z$  are the field components along the x, y, and z directions respectively.

Since both  $\Delta V$  and  $\Delta T$  satisfy Laplace's equation, the expression for the total field anomaly may be written in the following way in terms of a finite harmonic series expansion:

$$(1-6) \quad \Delta T(x, y, z) = \sum_{n=-\frac{N}{2}}^{\frac{N}{2}} \sum_{m=-\frac{M}{2}}^{\frac{M}{2}} W_{Tmn} \exp \left[ -2\pi \left( \frac{m^2}{L_x^2} + \frac{n^2}{L_y^2} \right)^{1/2} z \right] \exp \left[ 2\pi i \left( \frac{mx}{L_x} + \frac{ny}{L_y} \right) \right]$$

where  $L_x$ ,  $L_y$  are the fundamental wavelengths along x and y axes respectively and  $W_{Tmn}$  is the discrete Fourier Transform of  $\Delta T$ .

In practice, the total magnetic field  $\Delta T(x, y, 0)$  is represented in terms of a grid of discrete values

$$\begin{aligned} \Delta T_{jk} &= \Delta T(j\Delta, k\Delta), \\ \text{for } j &= 0, 1, \dots, M-1 \\ k &= 0, 1, \dots, N-1 \end{aligned}$$

where  $\Delta$  = grid interval.

From the discrete data array  $\Delta T_{jk}$ , we obtain the discrete Fourier transform

$$(1-7) \quad W_{Tmn} = \frac{1}{MN} \sum_{j=0}^{M-1} \sum_{k=0}^{N-1} \Delta T_{jk} \exp \left[ -2\pi i \left( \frac{j m}{M} + \frac{k n}{N} \right) \right].$$

$H_x(x, y, z)$ ,  $H_y(x, y, z)$  and  $H_z(x, y, z)$  can also be represented analytically in terms of a finite harmonic series expansion

$$(1-8) \quad \begin{Bmatrix} H_x \\ H_y \\ H_z \end{Bmatrix} = \sum_{m=-\frac{M}{2}}^{\frac{M}{2}} \sum_{n=-\frac{N}{2}}^{\frac{N}{2}} \begin{Bmatrix} W_{xmn} \\ W_{ymn} \\ W_{zmn} \end{Bmatrix} \exp \left[ -2\pi \left( \frac{m^2}{L_x^2} + \frac{n^2}{L_y^2} \right)^{1/2} z \right] \exp \left[ 2\pi i \left( \frac{mx}{L_x} + \frac{ny}{L_y} \right) \right].$$

where  $W_{xmn}$ ,  $W_{ymn}$ ,  $W_{zmn}$  are the discrete Fourier transforms of  $H_x$ ,  $H_y$  and  $H_z$  respectively.

Introducing (1-6) and (1-8) into the equations (1-3), (1-4), and (1-5), we get the following relationships

$$(1-9) \quad W_{xmn} = \frac{i F_m}{g_{mn}} W_{Tmn}, \quad W_{ymn} = \frac{i F_n}{g_{mn}} W_{Tmn}$$

$$\text{and } W_{zmn} = \frac{p_{mn}}{g_{mn}} W_{Tmn},$$

where  $F_m$  and  $F_n$ , angular frequencies along x and y axes respectively, are given by

$$F_m = 2\pi m / L_x, \quad F_n = 2\pi n / L_y.$$

$p_{mn}$  is given by

$$p_{mn} = 2\pi \left[ \frac{m^2}{L_x^2} + \frac{n^2}{L_y^2} \right]^{1/2} = \left[ F_m^2 + F_n^2 \right]^{1/2}$$

and  $g_{mn}$  is given by

$$g_{mn} = \gamma' p_{mn} + i (\alpha' F_m + \beta' F_n)$$

where  $\alpha'$ ,  $\beta'$  and  $\gamma'$  are the direction cosines of the geomagnetic field.

It is to be noted that the expressions for  $W_{xmn}$ ,  $W_{ymn}$ , and  $W_{zmn}$  are undefined when m and n are simultaneously equal to zero. Therefore  $W_{x00}$ ,  $W_{y00}$ , and  $W_{z00}$  have to be calculated by other means as shown in the following paragraphs.

The Fourier transform  $W(u,v)$  of a function of two variables  $F(x,y)$  is given by:

$$W(u,v) = \iint_{-\infty}^{\infty} F(x,y) \exp \left[ -2\pi i (ux + vy) \right] dx dy,$$

where u and v are the wavenumbers in the x and y directions respectively.

From the above equation, we can obtain the following equation

$$W(0,0) = \iint_{-\infty}^{\infty} F(x,y) dx dy.$$

It can be shown (Bhattacharyya, 1967) that

$$\iint_{-\infty}^{\infty} F(x, y) dx dy = W(0, 0) = 0.$$

Similarly we have  $W_x(0, 0) = W_y(0, 0) = W_z(0, 0) = 0$ .

In practice, it is impossible to perform the integral over an infinite plane and so the integral of the above equation will never be exactly equal to zero. Rewriting the equation in summation forms in terms of a finite grid spacing, we have

$$W_{x00} = \frac{1}{MN} \sum_{j=0}^{M-1} \sum_{k=0}^{N-1} H_{xjk}$$

$$W_{y00} = \frac{1}{MN} \sum_{j=0}^{M-1} \sum_{k=0}^{N-1} H_{yjk}$$

$$W_{z00} = \frac{1}{MN} \sum_{j=0}^{M-1} \sum_{k=0}^{N-1} H_{zjk}$$

Choosing the origin of the Cartesian coordinates at the lower left of the map and assuming that  $H_{xjk}$ ,  $H_{yjk}$ ,  $H_{zjk}$  tend to zero along the boundary, from equation (1-8) we get the following equation:

$$(1-10) \quad \left. \begin{aligned} W_{x00} &= - \sum_{n=-N/2}^{N/2} \sum_{m=-M/2}^{M/2} W_{xmn} \\ W_{y00} &= - \sum_{n=-N/2}^{N/2} \sum_{m=-M/2}^{M/2} W_{ymn} \\ W_{z00} &= - \sum_{n=-N/2}^{N/2} \sum_{m=-M/2}^{M/2} W_{zmn} \end{aligned} \right\} \text{except } m = n = 0.$$

Thus  $H_x$ ,  $H_y$  and  $H_z$  can be obtained from equations (1-8), (1-9) and (1-10) if the Fourier series expansion of the total field observations is available.



## 2. Evaluation of field components

In this section, the accuracy in calculating the field components from the total field data by the method described in the previous section will be examined with the help of a theoretical model.

The model chosen is an infinite prismatic body as shown in Figure 1. The dimensions and the declination and inclination of the magnetization vector of the prism are:

$$2a = 16, 2b = 8, h = 3, I = 20^\circ, D = 0^\circ, I_0 = 60^\circ, D_0 = 45^\circ,$$

where  $2a$  and  $2b$  are the horizontal dimensions along  $x$  and  $y$  axes respectively,  $h$  is the depth to the top of the body.  $I$  and  $D$  are respectively the inclination and declination of the geomagnetic field respectively. It is assumed that the prism is uniformly magnetized and the intensity of magnetization is unity.

The exact values of the field components of the prism are computed from the following equations (Bhattacharyya, 1964).

$$(1-11) \quad \begin{aligned} H_x &= I_p \left[ -\alpha \tan^{-1} \frac{\epsilon \eta}{\epsilon^2 + \gamma_0^2 h + h^2} - \beta \log(\gamma_0 + h) - \frac{\gamma}{2} \log \frac{\gamma_0 + \gamma}{\gamma_0 - \gamma} \right] \epsilon_u \begin{vmatrix} \eta_u \\ \eta_l \end{vmatrix}, \\ H_y &= I_p \left[ -\alpha \log(\gamma_0 + h) - \beta \tan^{-1} \left( \frac{\epsilon \eta}{\eta^2 + \gamma_0^2 h + h^2} \right) - \frac{\gamma}{2} \log \frac{\gamma_0 + \epsilon}{\gamma_0 - \epsilon} \right] \epsilon_u \begin{vmatrix} \eta_u \\ \eta_l \end{vmatrix}, \\ H_z &= I_p \left[ -\frac{\alpha}{2} \log \left( \frac{\gamma_0 + \gamma}{\gamma_0 - \gamma} \right) - \frac{\beta}{2} \log \left( \frac{\gamma_0 + \epsilon}{\gamma_0 - \epsilon} \right) + \gamma \tan^{-1} \left( \frac{\epsilon \eta}{\gamma_0 h} \right) \right] \epsilon_u \begin{vmatrix} \eta_u \\ \eta_l \end{vmatrix}, \end{aligned}$$

where  $\epsilon_l = -a - x$

$$\epsilon_u = a - x$$

$$\eta_l = -b - y$$

$$\eta_u = b - y \text{ and } \gamma_0 = (\epsilon^2 + \eta^2 + h^2)^{1/2}$$

$I_p$  is the intensity of magnetization of the prism and  $\alpha, \beta, \gamma$  are the direction cosines of the magnetization vector.

The total field component is given by

$$(1-12) \quad \Delta T = \alpha' H_x + \beta' H_y + \gamma' H_z$$

where  $\alpha'$ ,  $\beta'$ ,  $\gamma'$  are the direction-cosines of the geomagnetic field.

In practice, the total field anomaly is represented as discrete samples over a finite area. The discrete Fourier transform of these sample values is calculated with the help of the fast Fourier transform (FFT) computer algorithm (Cooley and Tukey, 1965).

The anomalous field and its components were computed on a  $64$  by  $64$  array of points with a unit grid interval. All of these computations were carried out with the help of a CDC 6400 computer in the Computer Center, University of California, Berkeley.

Figures 2 and 3 show the exact and computed values respectively of the x-component of the field. The rectangle in broken lines represents the horizontal cross-section of the prism. The large square contains  $64$  by  $64$  sample points. On the left hand side of each diagram are indicated the declination and inclination of the geomagnetic field. Triangle represents the point of maximum value of the field.

The anomalies in the two figures are practically identical. The differences in the anomalies are noticeable when the field component is about one-half of its maximum value. The exact field attenuates slightly faster than the computed field.

Figures 4 and 5 show the exact and computed values respectively of the y-component of the field. Both the figures are practically identical. However, the computed field in this case falls off a little faster than the exact field and the discrepancies in the two figures become noticeable at small values of the field component.

The characteristics of Figures 6 and 7 showing the exact and computed values of the z-component are also the same as those in the above two figures. The disparity between the two figures can be seen only when the magnitude falls

off to about one-sixth of the maximum value.

Figures 8 to 10 are the profiles along the N-S and E-W directions through the maximum response points. In each figure the exact and computed fields are marked by symbols (1) and (2) respectively. The horizontal axis of each figure represents the relative position on x and y directions. The vertical axis shows the magnitude of the field component along the profile. These profiles are useful for comparing the exact and computed fields in detail. As noted in the figures, the anomalies match remarkably well near the central parts where the magnitudes are high. However, in other regions there is noticeable discrepancy. For the particular model chosen, the match between the exact and computed values is the worst in the case of  $H_y$ .

The prismatic model in Figure 1 is assumed to be located at a high geomagnetic latitude,  $I_0 = 60^\circ$ . If the model is placed at lower latitudes, it can be safely concluded that the differences between exact and computed z-component field will increase. However, because of the change in the characteristics of the anomaly with geomagnetic latitude, the accuracy in the computation of the horizontal components cannot be predicted with confidence.

In order to study the effect of the variation of the geomagnetic field alone, all the parameters of the model in Figure 1 are kept fixed and only  $I_0$  and  $D_0$  are changed to  $30^\circ$  and  $15^\circ$  respectively. Figures 11 - 13 present the profiles of exact and computed X, Y, Z field components along the N - S and E - W directions through the maximum response points. A comparison of Figures 8 - 10 and 11 - 13 indicates an increase in discrepancy between the exact and computed values of the field components.

Figures 14 - 16 show the profiles of the field components for a model with the following parameters:

$$2a = 8, 2b = 4, h = 3, I = 40^\circ, D = 45^\circ, I_0 = 30^\circ, D_0 = 15^\circ$$

The objective for the choice of this model has been to determine changes in the accuracy of the computed field components due to variation in the geomagnetic field as well as in the horizontal dimensions of the prism. The effect of higher inclination of the magnetization vector compensates to a certain degree that of the lower geomagnetic latitude in the present example. By comparing Figure 8 with Figure 14 and Figure 9 with Figure 15 we find that for x- and y- components of the field, better results are obtained in the present case than in the first case. However, for the z- component, the differences between exact and computed field values near the central part of the anomaly are higher in Figure 16 than in Figure 10.

### 3. Horizontal Gradients of Field Components:

In the previous section, we discussed the method for obtaining the field components from total field measurements using finite harmonic series expansion. This section deals with the comparison of the horizontal gradients of the computed field components with the exact field gradients. Spatial filters were not used for this computation because the first horizontal derivative has an imaginary response in the frequency domain.

Bhattacharyya (1969) used bicubic splines representing a given set of magnetic observations for calculating the horizontal derivatives. This method is used to compute the derivatives of components. A brief treatment of this method is given in the following paragraphs.

If a function  $g(x,y)$  with two variables  $x$  and  $y$  is given at every mesh point of a grid system, such as

$$i = 0, 1, 2, \dots, M,$$

$$j = 0, 1, 2, \dots, N,$$

then the piecewise bicubic spline function has the following form:

$$(1-13) \quad g_{ij} = \sum_{m=0}^3 \sum_{n=0}^3 a_{mn}^{ij} (x - x_{i-1})^m (y - y_{j-1})^n,$$

where  $x_{i-1} \leq x \leq x_i$  and  $y_{j-1} \leq y \leq y_j$ . The horizontal derivatives can be easily computed if the coefficients  $a_{mn}^{ij}$  are available.

To determine the coefficients  $a_{mn}^{ij}$ , it is required to know the derivatives at the boundary points of each rectangular cell, i.e.,

$$(1-14) \quad p_{ij} = g_x(x_i, y_j),$$

$$(1-15) \quad q_{ij} = g_y(x_i, y_j),$$

$$(1-16) \quad \delta_{ij} = g_{xy}(x_i, y_j).$$

The parameters  $p$ ,  $q$  and  $s$  can be evaluated by the following steps:

(i) calculation of  $p_{ij}$

For each of the lines  $j = 0, 1, 2, \dots, N$ , the first derivatives  $p_{ij}$  should satisfy the equation.

$$(1-17) \quad p_{i+1,j} + 4p_{ij} + p_{i-1,j} = 3(g_{i+1,j} - g_{i-1,j}),$$

$$i = 1, 2, \dots, M-1;$$

At boundaries, when  $i = 0$  and  $i = M$ , the following condition holds:

$$(1-18) \quad g_{xx}(x_i, y_j) = 0, \quad \begin{matrix} i = 0, M; \\ j = 0, 1, 2, \dots, N. \end{matrix}$$

(ii) calculation of  $q_{ij}$

The equations for calculating  $q$  are similar to those of  $p$ . The equation is

$$(1-19) \quad q_{i,j+1} + 4q_{ij} + q_{i,j-1} = 3(g_{i,j+1} - g_{i,j-1}),$$

$$j = 1, 2, \dots, N-1; \quad i = 0, 1, 2, \dots, M.$$

The required condition at boundaries is

$$(1-20) \quad g_{yy}(x_i, y_j) = 0, \quad i = 0, 1, \dots, M; \quad j = 0, N.$$

(iii) Calculation of  $s_{ij}$

For computing  $s_{ij}$ , the values of  $p$  and  $q$  in equation (1-17) and (1-19) are used.

(a) For  $j = 0, N$

$$(1-21) \quad \Delta_{i+1,j} + 4 \Delta_{ij} + \Delta_{i-1,j} = 3 (q_{i+1,j} - q_{i-1,j}),$$

$$i = 1, 2, \dots, M-1.$$

(b) For  $i = 0, 1, \dots, M$

$$(1-22) \quad \Delta_{i,j+1} + 4 \Delta_{ij} + \Delta_{i,j-1} = 3 (p_{i,j+1} - p_{i,j-1}),$$

$$j = 1, 2, \dots, N-1.$$

(c) For  $i = 0, M$  and  $j = 0, N$

$$(1-23) \quad g_{xxy} (x_i, y_j) = 0.$$

The above steps are necessary for computing  $p$ ,  $q$ , and  $s$ . The detailed treatment is presented by Bhattacharyya (1969).

With the help of the values of  $p$ ,  $q$ , and  $s$ , it is easy to compute the coefficients of the piecewise bicubic splines. It is also very straightforward to calculate the derivatives at each mesh-point,  $x = x_i - 1$ ,  $y = y_j - 1$ .

The equations for computing the exact values of the first horizontal derivatives are obtained directly from equation (1-11) and they are given below:

$$(1-24) \quad \frac{\partial H_x}{\partial x} = I_p \left[ \alpha \frac{\eta (r_0 h - \epsilon^2)}{r_0 (\epsilon^2 + h^2) (r_0 + h)} + \beta \frac{\epsilon}{r_0 (r_0 + h)} - \gamma \frac{\epsilon \eta}{r_0 (\epsilon^2 + h^2)} \right]_{\epsilon_l}^{\epsilon_u} \left| \eta_u \right|_{\eta_l},$$

$$(1-25) \quad \frac{\partial H_y}{\partial x} = I_p \left[ \alpha \frac{\epsilon}{r_0 (r_0 + h)} + \beta \frac{\eta}{r_0 (r_0 + h)} + \gamma \frac{1}{r_0} \right]_{\epsilon_l}^{\epsilon_u} \left| \eta_u \right|_{\eta_l},$$

$$(1-26) \quad \frac{\partial H_z}{\partial x} = I_p \left[ -\alpha \frac{\epsilon \eta}{r_0 (\epsilon^2 + h^2)} + \beta \frac{1}{r_0} - \gamma \frac{\eta h}{r_0 (\epsilon^2 + h^2)} \right]_{\epsilon_l}^{\epsilon_u} \left| \eta_u \right|_{\eta_l},$$

and

$$(1-27) \quad \frac{\partial H_x}{\partial y} = I_p \left[ \alpha \frac{\epsilon}{r_0 (r_0 + h)} + \beta \frac{\eta}{r_0 (r_0 + h)} + \gamma \frac{1}{r_0} \right]_{\epsilon_l}^{\epsilon_u} \left| \eta_u \right|_{\eta_l},$$

$$(1-28) \quad \frac{\partial H_y}{\partial y} = I_p \left[ \alpha \frac{\eta}{r_0 (r_0 + h)} - \beta \frac{\epsilon (\eta^2 - r_0 h)}{r_0 (r_0 + h) (\eta^2 + h^2)} - \gamma \frac{\epsilon \eta}{r_0 (\eta^2 + h^2)} \right]_{\epsilon_l}^{\epsilon_u} \left| \eta_u \right|_{\eta_l}.$$

$$(1-29) \quad \frac{\partial H_z}{\partial y} = I_p \left[ \frac{\alpha}{r_0} - \beta \frac{\epsilon \gamma}{r_0 (\gamma^2 + h^2)} - \gamma \frac{\epsilon h}{r_0 (\gamma^2 + h^2)} \right]_{\epsilon_l}^{\epsilon_u} \left[ \eta_l \right]^{\eta_u}$$

#### 4. Results and Conclusions

The exact values of the horizontal derivatives of the field components are calculated with the help of equations (1-24) - (1-29). The field components are also obtained from total field observations with the method described in the previous section. These values of the field components are used to determine  $g_{ij}$  and p, q, and s. Then the bicubic spline coefficients in (1-13) are calculated. These coefficients yield the values of the horizontal derivatives of the computed field components.

The exact and computed values of the horizontal derivatives for the prismatic model in Figure 1 are obtained at equispaced points of a rectangular 64 x 64 grid system over a horizontal plane.

Figures 17 and 18 show the exact and computed solutions of  $\frac{\partial H_x}{\partial x}$  respectively. These two diagrams are almost identical. Some differences between the two solutions are noticeable when the magnitude falls off to about one-seventh of the maximum response. Fig. 19 shows the N - S and E - W profiles of exact and computed solutions. The profiles run through the point of maximum response. The E - W profile shows the excellent match of exact and computed solutions. However, there are appreciable differences between the solutions on the N - S profile. At the edges, the computed values on the N - S profiles do not vary smoothly.

Since  $\vec{\nabla} \times \vec{H} = 0$  in the plane of observation, we have

$$(1-30) \quad \frac{\partial H_y}{\partial x} = \frac{\partial H_x}{\partial y},$$



$$(1-31) \quad \partial H_z / \partial x = \partial H_x / \partial z,$$

$$(1-32) \quad \partial H_z / \partial y = \partial H_y / \partial z.$$

Because of the above relations, it is not necessary to calculate all the horizontal gradients of the field components.

Figures 20 and 21 show the exact and computed values respectively of  $\partial H_x / \partial y$ . Figure 22 shows the computed solution of  $\partial H_y / \partial x$ . These three figures are almost identical. It is interesting to note the closeness of the computed solutions of  $\partial H_x / \partial y$  and  $\partial H_y / \partial x$ . This characteristic can also be seen from the profiles in Figures 23 and 24. All the previous diagrams show the discrepancies between the exact and computed solutions after the magnitudes of the derivatives fall off to one-tenth of their maximum amplitudes. The N - S profiles contain more discrepancies than the E - W profiles do. For the N - S profile, the computed solution of  $\partial H_x / \partial y$  is not as smooth as the computed solution of  $\partial H_y / \partial x$ .

Figures 25 and 26 show the exact and computed solutions of  $\partial H_z / \partial x$  respectively. Figure 27 shows the N - S and E - W profiles. All these three diagrams indicate that the values are practically identical except in regions where the values are less than one-tenth of the maximum amplitude. The profiles also indicate that the values of the exact and computed derivatives are in better harmony in the case of the E - W profiles than they are in the case of the N - S profiles.

The exact and computed solutions of  $\partial H_y / \partial y$  are shown in Figures 28 and 29 respectively. The profiles along the N - S direction and E - W direction are shown in Figure 30. Similar quantities are plotted in Figures 31, 32, and 33 for  $\partial H_z / \partial y$ . The results in these diagrams are the same as those in the previous figures. A study of all the plots presented here show that of all the derivatives the computed  $\partial H_z / \partial y$  has the best match with the exact values.

## 5. Second Horizontal Derivatives of Field Components

The bicubic spline coefficients, as computed in the previous section for determining the horizontal gradients of field components, are also used to calculate the second horizontal derivatives. Data for the dimensions and magnetization of the prismatic body are given in section 1 of this chapter.

For the three components of the field, nine second horizontal derivatives can be calculated. However, it is known from the derivation in section three that  $\frac{\partial H_x}{\partial y} = \frac{\partial H_y}{\partial x}$ . From this relationship we can derive:

$$(1-33) \quad \frac{\partial^2 H_x}{\partial x \partial y} = \frac{\partial^2 H_y}{\partial x^2}$$

$$(1-34) \quad \frac{\partial^2 H_y}{\partial x \partial y} = \frac{\partial^2 H_x}{\partial y^2}$$

Therefore, only seven horizontal derivatives have to be calculated. However, because of the possibility of inaccuracies in computation, all the nine second horizontal derivatives have been calculated.

The exact values of the second horizontal derivatives are derived directly from equation (1-11). The equation of these exact values are given below:

$$(1-35) \quad \frac{\partial^2 H_x}{\partial x^2} = I_p \left[ \alpha \left( \frac{\epsilon \eta h (2\gamma_c^2 + \epsilon^2 + h^2)}{\gamma_c^3 (\epsilon^2 + h^2)^2} - \frac{\epsilon \eta (2\gamma_c + h)}{\gamma_c^3 (\gamma_c + h)^2} \right) + \right. \\ \left. \beta \frac{\epsilon^2 (2\gamma_c + h) - \gamma_c^2 (\gamma_c + h)}{\gamma_c^3 (\gamma_c + h)^2} - \gamma \frac{\eta h^2 (\epsilon^2 - \gamma_c^2) + \eta \epsilon^2 (\epsilon^2 + \gamma_c^2)}{\gamma_c^3 (\epsilon^2 + h^2)^2} \right] \begin{matrix} \epsilon_u \\ \epsilon_l \end{matrix} \begin{matrix} \eta_u \\ \eta_l \end{matrix}$$

$$(1-36) \quad \frac{\partial^2 H_y}{\partial x^2} = I_p \left[ \alpha \frac{\epsilon^2 (2\gamma_c + h) - \gamma_c^2 (\gamma_c + h)}{\gamma_c^3 (\gamma_c + h)^2} + \beta \frac{\epsilon \eta (2\gamma_c + h)}{\gamma_c^3 (\gamma_c + h)^2} + \gamma \frac{\epsilon}{\gamma_c^3} \right] \begin{matrix} \epsilon_u \\ \epsilon_l \end{matrix} \begin{matrix} \eta_u \\ \eta_l \end{matrix}$$

$$(1-37) \quad \frac{\partial^2 H_z}{\partial x^2} = I_p \left[ -\alpha \frac{\eta h^2 (\epsilon^2 - \gamma_c^2) + \eta \epsilon^2 (\gamma_c^2 + \epsilon^2)}{\gamma_c^3 (\epsilon^2 + h^2)} + \beta \frac{\epsilon}{\gamma_c^3} - \right. \\ \left. \gamma \frac{\epsilon \eta h (2\gamma_c^2 + \epsilon^2 + h^2)}{\gamma_c^3 (\epsilon^2 + h^2)^2} \right] \begin{matrix} \epsilon_u \\ \epsilon_l \end{matrix} \begin{matrix} \eta_u \\ \eta_l \end{matrix}$$

$$(1-38) \quad \frac{\partial^2 H_x}{\partial y^2} = I_p \left[ \alpha \frac{\epsilon \eta (2r_0 + h)}{r_0^3 (r_0 + h)^2} + \beta \frac{\eta^2 (2r_0 + h) - r_0^2 (r_0 + h)}{r_0^3 (r_0 + h)^2} + \right.$$

$$(1-39) \quad \left. \gamma \frac{\eta}{r_0^3} \right]_{\epsilon_l}^{\epsilon_u} \left| \eta_l \right|^{\eta_u},$$

$$(1-40) \quad \frac{\partial^2 H_y}{\partial y^2} = I_p \left[ \alpha \frac{\eta^2 (2r_0 + h) - r_0^2 (r_0 + h)}{r_0^3 (r_0 + h)^2} - \beta \left( \frac{\epsilon \eta (2r_0 + h)}{r_0^3 (r_0 + h)^2} - \frac{\epsilon \eta h (2r_0^2 + \eta^2 + h^2)}{r_0^3 (\eta^2 + h^2)^2} \right) - \gamma \frac{\epsilon \eta^2 (2r_0^2 + \eta^2 + h^2) - r_0^2 \epsilon (\eta^2 + h^2)}{r_0^3 (\eta^2 + h^2)^2} \right]_{\epsilon_l}^{\epsilon_u} \left| \eta_l \right|^{\eta_u},$$

$$\frac{\partial^2 H_z}{\partial y^2} = I_p \left[ \alpha \frac{\eta}{r_0^3} - \beta \frac{\epsilon \eta^2 (2r_0^2 + \eta^2 + h^2) - r_0^2 \epsilon (\eta^2 + h^2)}{r_0^3 (\eta^2 + h^2)^2} - \right.$$

and

$$\left. \gamma \frac{\epsilon \eta h (2r_0^2 + \eta^2 + h^2)}{r_0^3 (\eta^2 + h^2)^2} \right]_{\epsilon_l}^{\epsilon_u} \left| \eta_l \right|^{\eta_u},$$

$$(1-41) \quad \frac{\partial^2 H_z}{\partial x \partial y} = I_p \left[ \alpha \frac{\epsilon}{r_0^3} + \beta \frac{\eta}{r_0^3} + \gamma \frac{h}{r_0^3} \right]_{\epsilon_l}^{\epsilon_u} \left| \eta_l \right|^{\eta_u}$$

## 6. Results and Conclusions

Figures 34 and 35 show the exact and the computed values of  $\partial^2 H_x / \partial x^2$ . It is apparent from Figure 35 that only about one-third of the calculated values which cover the central part of the contoured map, is reliable. However, even in this central part, the discrepancies between exact and computed values are appreciable. Figure 36 presents the N - S and E - W profiles of the computed and exact values. The profiles give a clear picture of how the computed solution of  $\partial^2 H_x / \partial x^2$  behaves and why along the boundaries of Figure 35 no contour was drawn. Since the amplitudes of second derivatives fall off sharply, the smallest amplitude of reliable data is about one-sixth of the maximum amplitude. Some differences can be observed even at the center of the diagram.

Figures 37 and 38 show the exact and computed values of  $\partial^2 H_y / \partial x^2$ .

Some differences between computed and exact fields are noticeable, even in the central part of the diagram. The computed map is not exactly symmetrical. The two diagrams show good similarity until the amplitude of the computed field falls off to about one-fourth of its maximum amplitude. Figure 39 shows the computed values of  $\partial^2 H_x / \partial x \partial y$ . As we pointed out before,  $\partial^2 H_x / \partial x \partial y$  is theoretically equal to  $\partial^2 H_y / \partial x^2$ . However, the computed values of  $\partial^2 H_y / \partial x^2$  are not exactly equal to those of  $\partial^2 H_x / \partial x \partial y$ . Furthermore, the computed  $\partial^2 H_x / \partial x \partial y$  is closer to the exact values than computed  $\partial^2 H_y / \partial x^2$ . This characteristic is clearly indicated in the N - S and the E - W profiles shown in Figures 40 and 41. These two diagrams also indicate the occurrence of the maximum value at different points. For the computed solution, the maximum amplitude of computed  $\partial^2 H_y / \partial x^2$  occurs at the point  $x = -8, y = -4$ , whereas that of  $\partial^2 H_x / \partial x \partial y$ , at  $x = -8, y = 3$ .

Figures 42 and 43 present the exact and computed values of  $\partial^2 H_z / \partial x^2$  respectively. The fields of  $\partial^2 H_z / \partial x^2$  contain two distinct anomalies, one located at the south end and the other at the north end of the prism. The computed values are close to the exact values only near these anomalies. These anomalies are also present in Figure 44.

Figures 45 and 46 show the exact and computed values of  $\partial^2 H_x / \partial y^2$ . These two diagrams are practically identical except for small values of the contours. The N - S and E - W profiles of  $\partial^2 H_x / \partial y^2$  are presented in Figure 48. As mentioned in section 5,  $\partial^2 H_x / \partial y^2$  is theoretically equal to  $\partial^2 H_y / \partial x \partial y$ . Therefore, Figure 45 also represents the exact map of  $\partial^2 H_y / \partial x \partial y$ . The computed solution of  $\partial^2 H_y / \partial x \partial y$  is shown in Figure 47. Again Figures 45 and 47 are identical. Figure 49 shows the N - S and E - W profiles of  $\partial^2 H_y / \partial x \partial y$ . The computed  $\partial^2 H_y / \partial x \partial y$  is very close to the exact values.

The exact and computed values of  $\partial^2 H_y / \partial y^2$  are presented in Figures 50 and 51. The difference between the two diagrams becomes obvious when the amplitude drops to about one-tenth of the maximum. Figure 52 shows the N - S and E - W profiles through the maximum. These profiles also indicate the inaccuracies of the computed fields around the boundaries when the amplitude becomes relatively small.

Figures 53 and 54 show the exact and computed values of  $\partial^2 H_z / \partial y^2$ . Some differences between the two diagrams are noticeable when the amplitude drops to about one-eighth of the maximum value. The computed field generally does not falloff as sharply as the exact field. Figure 55 shows the N - S and E - W profiles.

Figures 56 and 57 present the exact and computed values of  $\partial^2 H_z / \partial x \partial y$ . The characteristics of these diagrams are very similar to those observed in the previous figures. The profiles through the maximum are shown in Figure 58.

## 7. Concluding Remarks

In this chapter, the results of investigation on the accuracy of computing field components from total field observations have been presented. It is found that even for a simple model such as a prismatic body, the computed field components and their derivatives are accurate only in regions surrounding the maximum amplitudes. As the amplitudes of the various derived fields start to decay, the errors in computation increase.

In the case of actual measurements of the total field, the accuracy in computing field components will be much inferior to that obtained in this study. The gradients and second horizontal derivatives of the computed components will show large errors. These errors will also be responsible for inaccuracies in the computation of parameters of causative bodies. It can, therefore, be safely

concluded that measurements of field components, if and when possible, is much preferable to the calculation of these components with the help of total field observations.

## Chapter 2: Calculation of the Magnetization Vector

In the previous chapter, the magnetic field components along three mutually orthogonal directions were obtained from the total field measurements. These components are used to determine the direction-cosines and the magnitudes of the magnetization vectors associated with causative bodies. These unknown parameters are also computed with exact values of the field components due to prismatic bodies. A comparison of the values of the parameters, as obtained from exact and computed field components, is useful to evaluate the need for measurements of field components.

### 1. Method for the determination of the magnetization vector

The method adopted in this study for the determination of the magnetization vector is essentially based on the theoretical treatment of this subject by Bhattacharyya ( 1967).

Let us assume that over the volume occupying the magnetized masses the magnetic dipole moment per unit volume has a fixed direction but variable magnitude. If the direction is supposed to have an inclination  $I$  and declination  $D$ , and if the direction cosines are denoted by  $\alpha$ ,  $\beta$ , and  $\gamma$ , we have

$$\begin{aligned} M_i &= M_o \cos I \cos D = M_o \cdot \alpha, \\ (2-1) \quad M_j &= M_o \cos I \sin D = M_o \cdot \beta, \\ M_k &= M_o \sin I = M_o \cdot \gamma. \end{aligned}$$

Let us assume that the total magnetic moment of the magnetized mass in volume  $V_o$  be denoted by

$$(2-2) \quad M_T = \int_{V_o} M_o \, dv_o.$$

It can be easily shown that

$$(2-3) \quad M_x^x = \iint_{-\infty}^{\infty} x H_x dx dy = 2\pi \gamma M_T = \iint_{-\infty}^{\infty} y H_y dx dy$$

$$(2-4) \quad M_z^x = \iint_{-\infty}^{\infty} x H_z dx dy = 2\pi \alpha M_T$$

$$(2-5) \quad M_z^y = \iint_{-\infty}^{\infty} y H_z dx dy = 2\pi \beta M_T$$

$$(2-6) \quad \iint_{-\infty}^{\infty} x H_y dx dy = \iint_{-\infty}^{\infty} y H_x dx dy = 0$$

$$(2-7) \quad \alpha^2 + \beta^2 + \gamma^2 = 1$$

The declination and inclination of magnetization vector can be easily expressed as

$$(2-8) \quad D = \arccos \left( \alpha / \sqrt{\alpha^2 + \beta^2} \right)$$

$$(2-9) \quad I = \arcsin \gamma$$

Thus in the case of three-component data, the magnitude and direction of the magnetization vector can be evaluated with the help of equation (2-3) to (2-9).

As a matter of fact, only the moments of  $H_z$  and  $H_x$  in the above equations are used here. From equation (2-3) it is easy to see that we can use the moment of  $H_y$  instead of  $H_x$ . Thus it can be concluded that  $H_z$  together with only one of the two horizontal components is sufficient for calculating the magnitude and direction of the magnetization vector.



Now, let us assume that the total available range of integration in the x direction runs from  $X = -M\Delta/2$  to  $X = M\Delta/2$  and in the y direction, from  $Y = -N\Delta/2$  to  $Y = N\Delta/2$  when the origin of the coordinate system is placed somewhere near the center of the anomaly, where

M is the total number of samples along the x axis,

N is the total number of samples along the y axis,

$\Delta$  is the interval between the samples.

Therefore, from equation (2-3), (2-4) and (2-5) we can write

$$(2-10) \quad 2\pi\gamma M_T \approx \int_{-X}^X \int_{-Y}^Y x H_x dx dy = M_x^x$$

$$(2-11) \quad 2\pi\alpha M_T \approx \int_{-X}^X \int_{-Y}^Y x H_z dx dy = M_z^x$$

$$(2-12) \quad 2\pi\beta M_T \approx \int_{-X}^X \int_{-Y}^Y y H_z dx dy = M_z^y$$

The integrals (2-10) - (2-12) are of the type

$$\int_{-X}^X \int_{-Y}^Y f(x, y) dx dy.$$

Using the trapezoidal rule we have

$$(2-13) \quad F(x) = \int_{-Y}^Y f(x, y) dy \approx \Delta \left[ \frac{1}{2} f_{x0} + \sum_{n=1}^{N-1} f_{xn} + \frac{1}{2} f_{xN} \right].$$

Then using the same trapezoidal rule for the integrals  $F(x)$ , we have

$$(2-14) \quad \int_{-X}^X F(x) dx \approx \Delta \left[ \frac{1}{2} F_0 + \sum_{m=1}^{M-1} F_m + \frac{1}{2} F_M \right]$$

Assuming that  $f(x, y)$  tends smoothly to a very small value along the boundary, we can obtain the following approximation from (2-13) and (2-14):

$$(2-15) \quad \int_{-X}^X \int_{-Y}^Y f(x, y) dx dy \approx \Delta^2 \sum_{m=1}^M \sum_{n=1}^N f_{mn},$$

where  $f_{mn} = f$  (ms, ns)

By assuming unit grid spacing and with equalities replacing the approximation signs, the reasonable computational versions of equation (2-10) to (2-12) are given by

$$(2-16) \quad M_x^x = \sum_{m=1}^M \sum_{n=1}^N x_m H_{xmn} = 2\pi\gamma M_T,$$

$$(2-17) \quad M_z^x = \sum_{m=1}^M \sum_{n=1}^N x_m H_{zmn} = 2\pi\alpha M_T,$$

$$(2-18) \quad M_z^y = \sum_{m=1}^M \sum_{n=1}^N y_n H_{zmn} = 2\pi\beta M_T.$$

With the availability of digital computers, the numerical calculation of the above equation is not very time-consuming.

## 2. Calculations and Results

Lourenco (1972) has calculated the magnitude and direction of the magnetization vector using exact and computed values of three-component magnetic data for different types of theoretical models.

In the present study also, a rectangular prismatic body is chosen as the model and the magnetization of the body is assumed to be arbitrary. The parameters selected for the model are given below:

$$2a = 16, 2b = 8, h_t = 6, h_b = 10, I_p = 1.$$

The following two cases are then studied for examining the influence of the geomagnetic field on the calculation of the directions of the magnetization vector:

$$(i) \quad I_o = 60^\circ \text{ and } D_o = 45^\circ$$

$$(ii) \quad I_o = 30^\circ \text{ and } D_o = 15^\circ.$$

For the magnetization vector, the inclination is initially fixed at  $20^\circ$  and the declination is varied from  $0^\circ$  to  $80^\circ$  at steps of  $10^\circ$ . Then with the help of exact and computed field components, the direction and intensity of the magnetization vector are determined with the method described in the previous section. Studies have also been conducted for the case when the declination is  $0^\circ$  and the inclination changes at steps of  $10^\circ$  from  $0^\circ$  to  $80^\circ$ . Exact and computed field components are obtained over a  $64 \times 64$  grid for the calculation of moments.

The results of calculation are given in tables (2-1) and (2-2). In these two tables,  $D$ ,  $I$  and  $I_p$  are the assumed values of declination, inclination, and intensity of magnetization;  $D_1$ ,  $I_1$  and  $I_{p1}$  are calculated values for exact three-component magnetic data;  $D_2$ ,  $I_2$  and  $I_{p2}$  are obtained from computed field components for the case,  $I_o = 60^\circ$  and  $D_o = 45^\circ$ ; and  $D_3$ ,  $I_3$  and  $I_{p3}$  are also obtained from computed field components for  $I_o = 30^\circ$  and  $D_o = 15^\circ$ .

The deviation of declination which is the difference between the assumed and computed values of declination, is shown in Figures 59 and 60 as functions of inclination and declination respectively of the magnetization vector. In Figure 59, the declination has been kept fixed as shown in Table 2-1. Figure 60 corresponds to Table 2-2.

Two characteristics of the curves in Figs. 59 and 60 are to be noted. First, the computed values of declination deviate with increasing error from the correct values as the inclination of the magnetization vector increases. Second, errors are significantly larger for lower geomagnetic latitudes. A comparison of the two curves for  $I_o = 60^\circ$ ,  $D_o = 45^\circ$  and  $I_o = 30^\circ$ ,  $D_o = 15^\circ$  shows that the computed declinations vary by about  $3 - 5^\circ$  over the entire range of variation of the direction of the magnetization vector.

Figures 61 and 62 present the deviation of the computed values of inclination from the correct values as functions of inclination and declination respectively. In this case also, errors in computation increase as the geomagnetic latitude of the observation point is decreased. Errors in values obtained from computed field components decrease with increasing inclination and declination of the magnetization vector, become zero and then start to increase with opposite signs. No explanation is available for this particular characteristic of the errors.

Tables 2-1 and 2-2 show that the computed intensities of magnetization are practically constant for all possible directions of the magnetization vector and differ by a constant from the correct value. This difference is mainly due to the limited area of observations chosen for the calculation of moments.

### 3. Concluding Remarks

The moments calculated from three-component magnetic data are not affected by changes in inclination or declination of the magnetization vector. Perhaps moments could have been calculated with greater accuracy by choosing larger areas with increase in data points.

With exact values of field components the error in calculated declinations is always less than two degrees and the computed inclinations are within  $1^\circ$  of the exact values. The computed field components, as expected, give rise to greater errors and these errors increase with reduction in geomagnetic latitude.

The calculations presented in this report show rather conclusively the superiority of exact components over computed components in determining the magnetization vector with a reasonable accuracy.

Table 2-1

$D = 0^\circ, I_p = 1$

I	$D_1$	$I_1$	$I_{p1}$	$D_2$	$I_2$	$I_{p2}$	$D_3$	$I_3$	$I_{p3}$
0	0.002	0.795	0.665	0.80	5.211	0.645	4.153	7.391	0.561
10	0.083	10.786	0.666	1.194	14.058	0.658	4.618	18.178	0.584
20	0.173	20.760	0.666	1.606	22.629	0.665	5.100	28.112	0.609
30	0.276	30.720	0.667	2.067	31.079	0.668	5.633	37.297	0.632
40	0.403	40.672	0.667	2.619	39.552	0.663	5.265	45.888	0.650
50	0.576	50.620	0.667	3.344	48.194	0.654	7.080	54.063	0.663
60	0.841	60.571	0.667	4.411	57.143	0.640	8.256	62.001	0.667
70	1.347	70.530	0.666	6.284	66.519	0.623	10.251	69.875	0.658
80	2.856	80.498	0.666	10.853	76.383	0.605	14.769	77.830	0.667

Table 2-2

$I = 20^\circ, I_p = 1$

D	$D_1$	$I_1$	$I_{p1}$	$D_2$	$I_2$	$I_{p2}$	$D_3$	$I_3$	$I_{p3}$
0	0.173	20.706	0.666	1.606	22.629	0.665	5.100	28.112	0.609
10	9.962	20.793	0.666	11.494	22.184	0.668	16.149	27.341	0.619
20	20.090	20.790	0.667	21.265	21.627	0.670	26.639	26.306	0.632
30	30.197	20.754	0.667	30.933	20.983	0.670	36.529	25.119	0.645
40	40.374	20.688	0.668	40.518	20.274	0.670	45.857	23.878	0.656
50	50.317	20.596	0.669	50.051	19.524	0.668	54.714	22.658	0.665
60	60.324	20.486	0.670	59.566	18.752	0.665	63.223	21.511	0.670
70	70.299	20.362	0.670	69.100	17.978	0.659	71.520	20.470	0.670
80	80.247	20.232	0.670	78.689	17.222	0.654	79.748	19.555	0.665
90	89.982	20.100	0.670	88.365	16.493	0.647	88.055	18.777	0.654

### References

- Bhattacharyya, B.K., 1964, Magnetic anomalies due to prism shaped bodies with arbitrary polarization: *Geophysics*, v. 29, p. 517-531.
- \_\_\_\_\_, 1965, Two-dimensional harmonic analysis as a tool for magnetic interpretation: *Geophysics*, v. 30, p. 829-851 .
- \_\_\_\_\_, 1967, Some general properties of potential fields in space and frequency domain: A Review: *Geoexploration*, v. 5, p. 127-143.
- \_\_\_\_\_, 1969, Bicubic spline interpolation as a method for treatment of potential field data: *Geophysics*, v. 34, p. 402-423.
- Cooley, J.W., and Tukey, J.W., 1965, An algorithm for the machine calculation of complex Fourier Series: *Math of Computation*, v. 19, no. 90, p. 297-301.
- Hughes, D.S., and Pondroms, W.L., 1947, Computation of vertical magnetic anomalies from total magnetic field measurements: *Am. Geophys. Union Trans.*, v. 28, p. 193-197.
- Iufer, E., 1971, A new-fully-automated airborne vector magnetometer: Symposium on treatment and interpretation of aeromagnetic data, University of California, Berkeley.
- Lourenco, J.S., 1972, Analysis of three-component magnetic data, Ph. D. thesis, University of California, Berkeley.
- Lourenco, J.S. and Morrison, H.F., 1973, Vector magnetic anomalies derived from measurements of a single component of the field: *Geophysics*, v. 38, p. 359-368
- Vestine, E.H., and Davids, N., 1945, Analysis and interpretation of geomagnetic anomalies: *Terrestrial Magnetism and Atmospheric Electricity*, v. 50, p. 1-36.

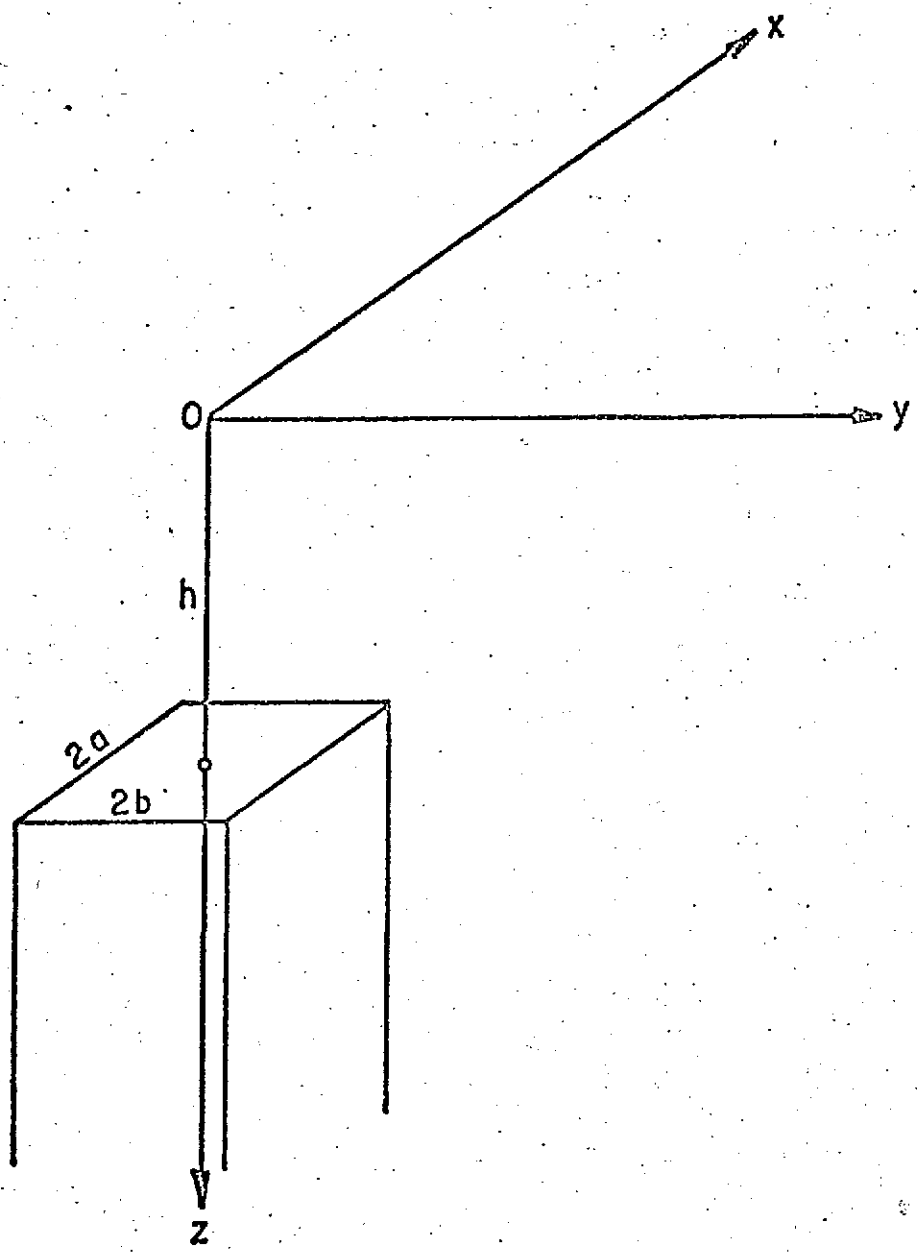


Figure I

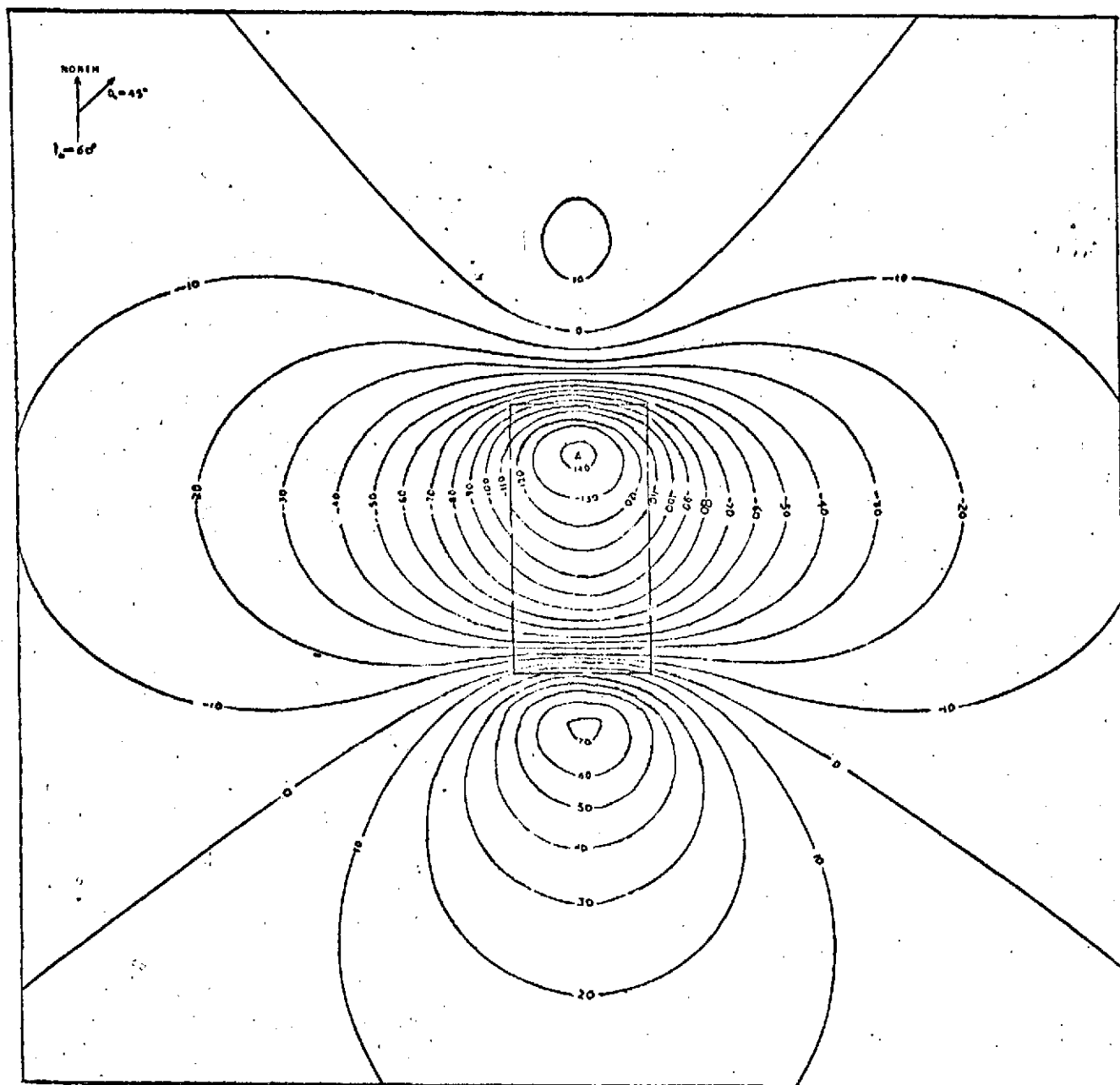


Figure 2



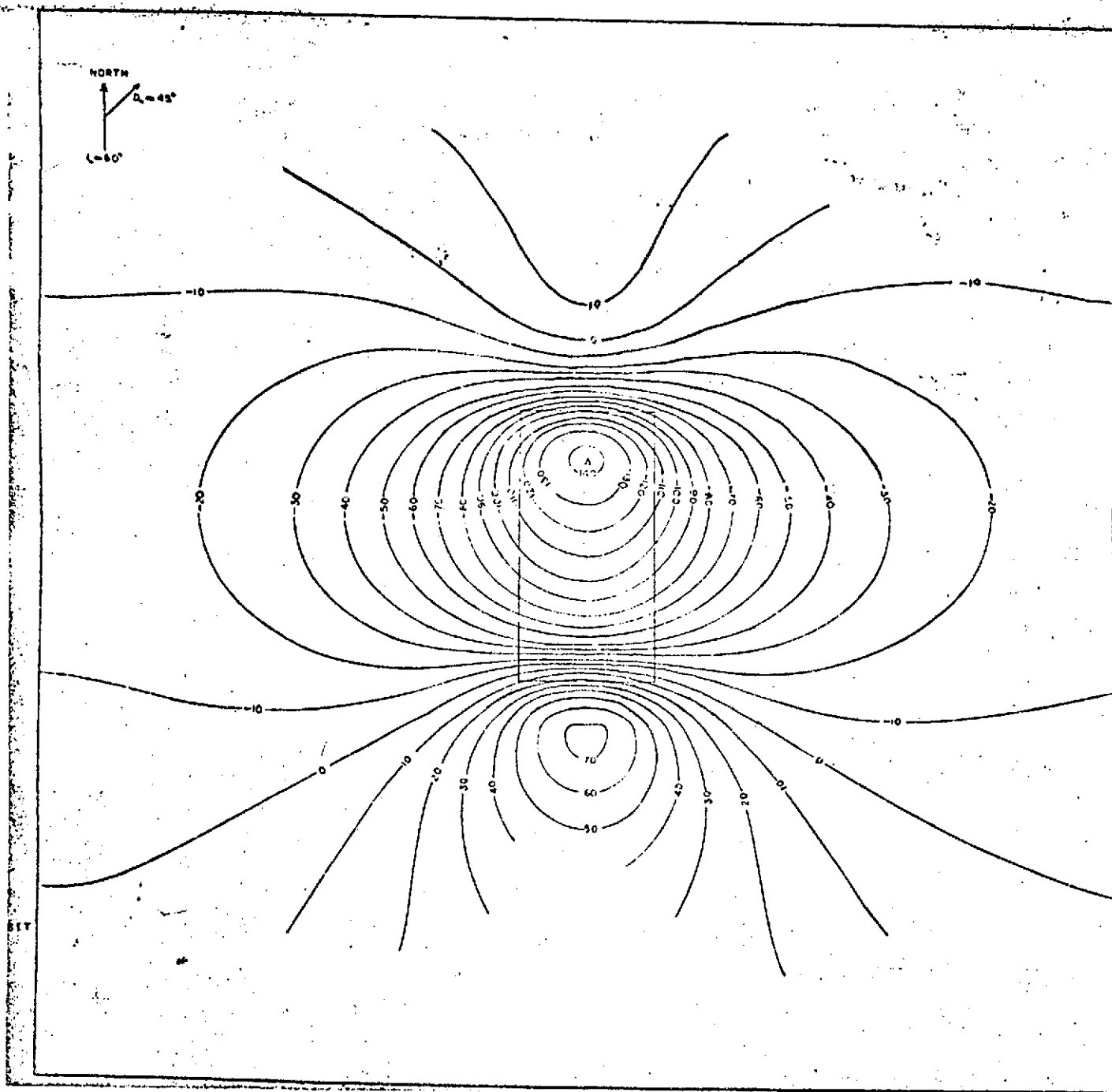


Figure 3

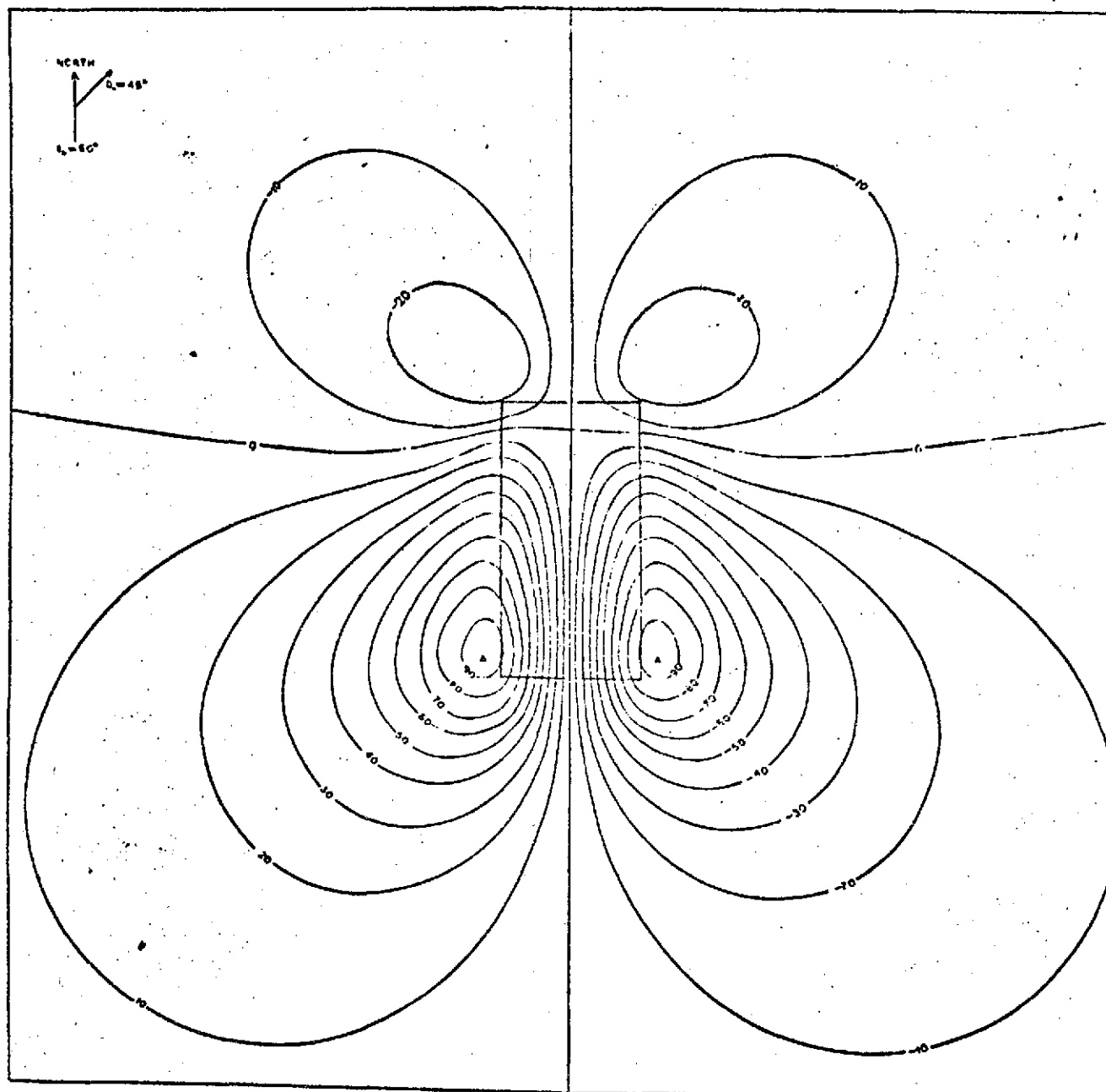


Figure 4

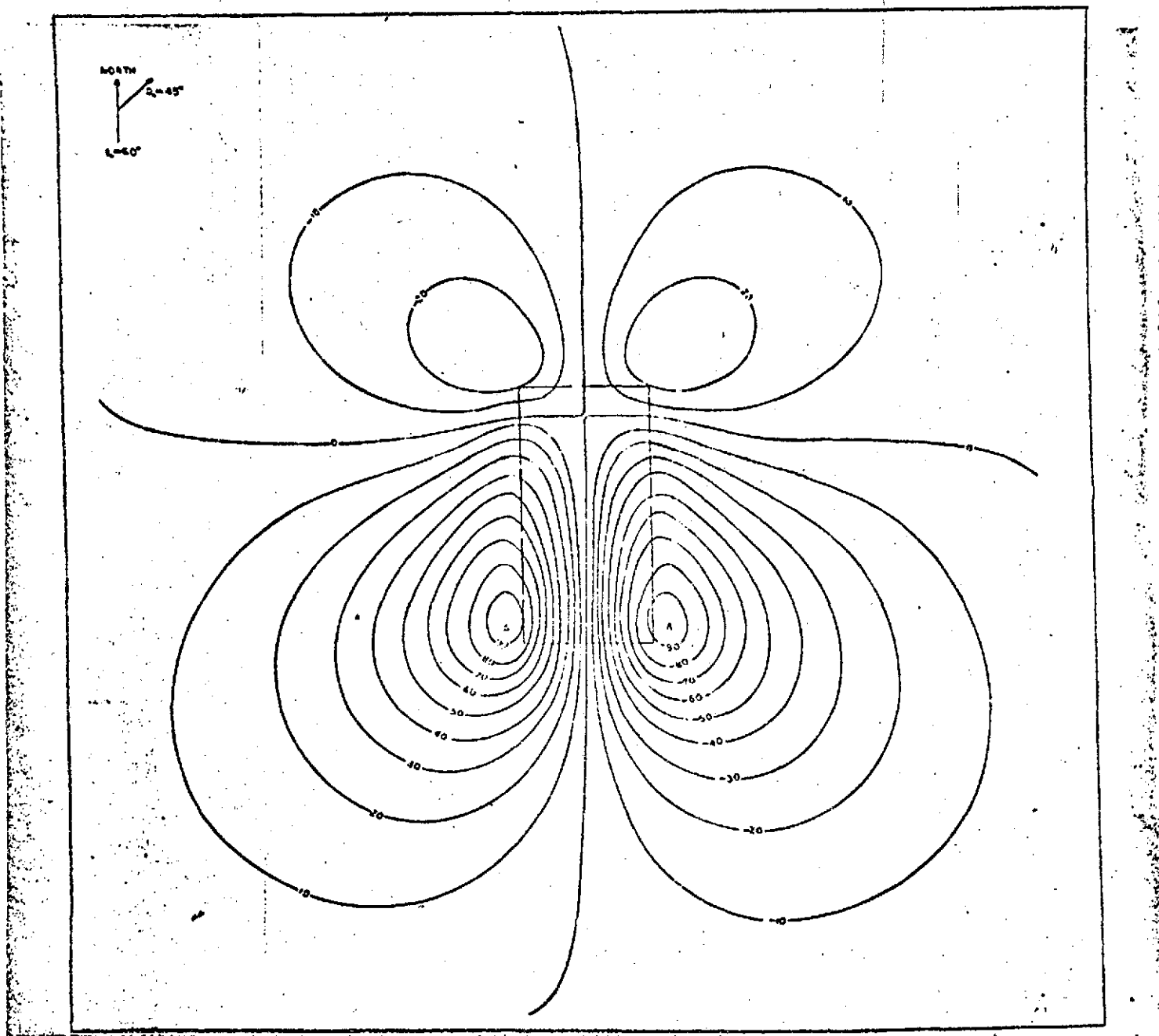


Figure 5

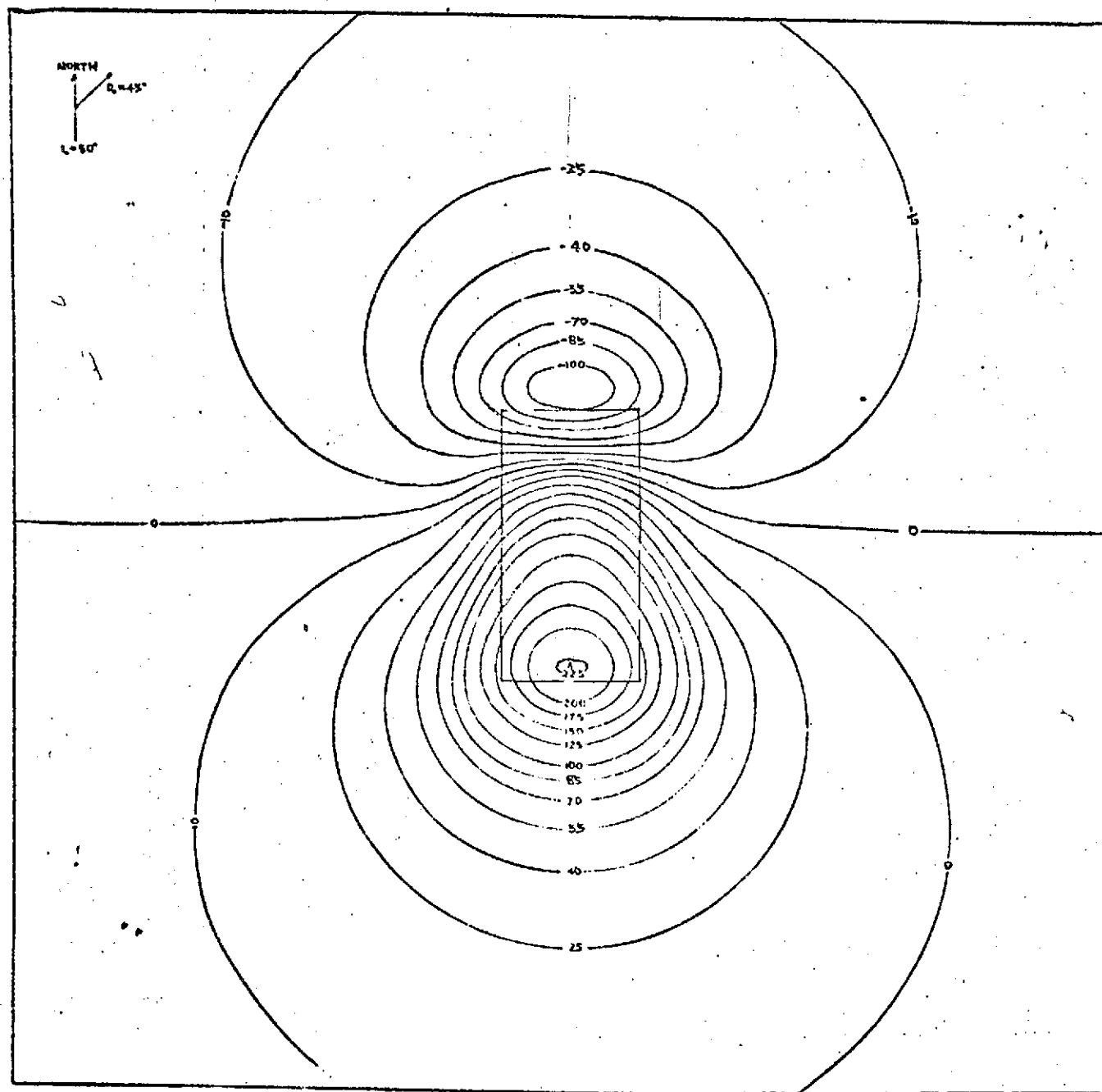


Figure 6

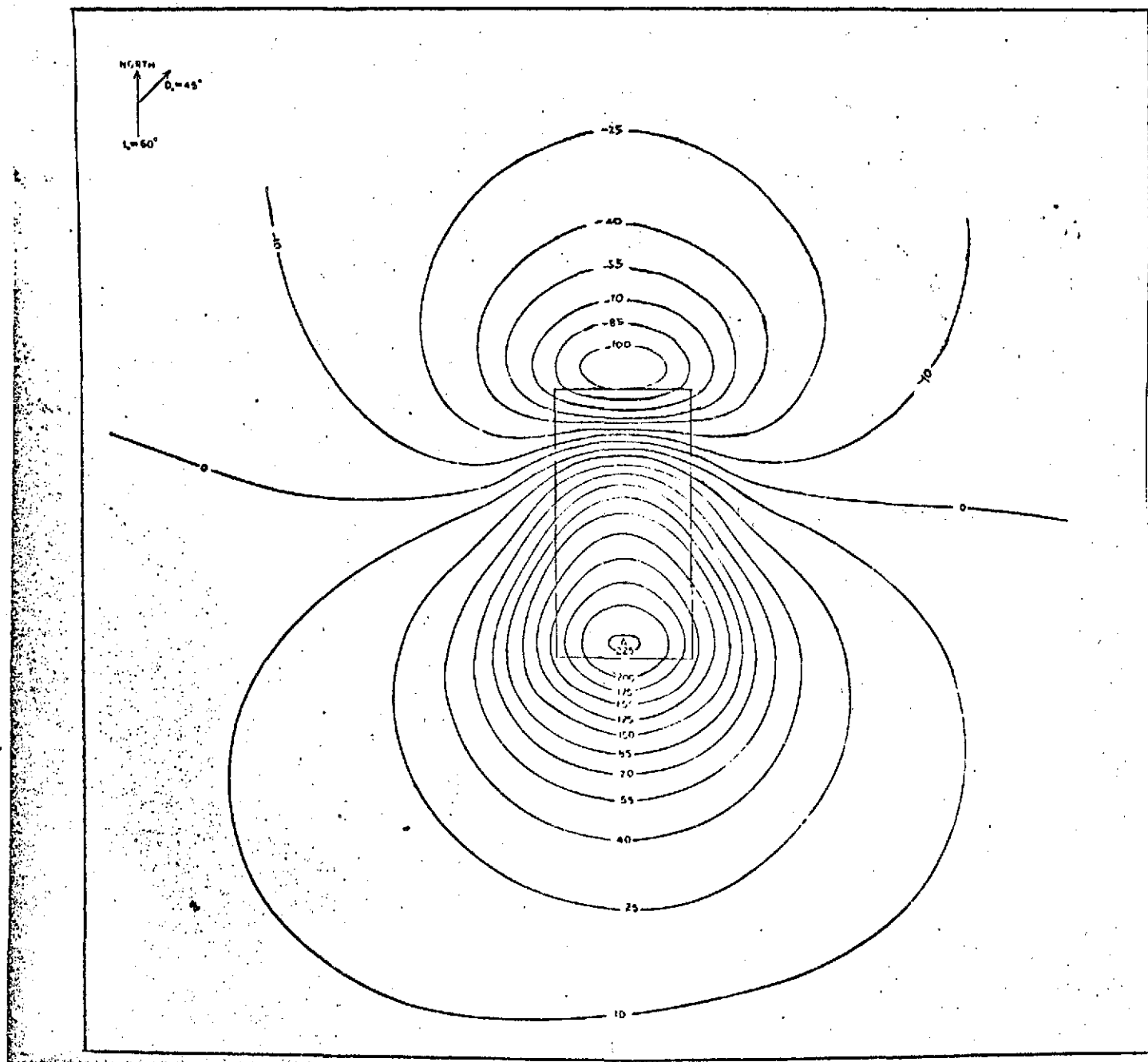


Figure 7

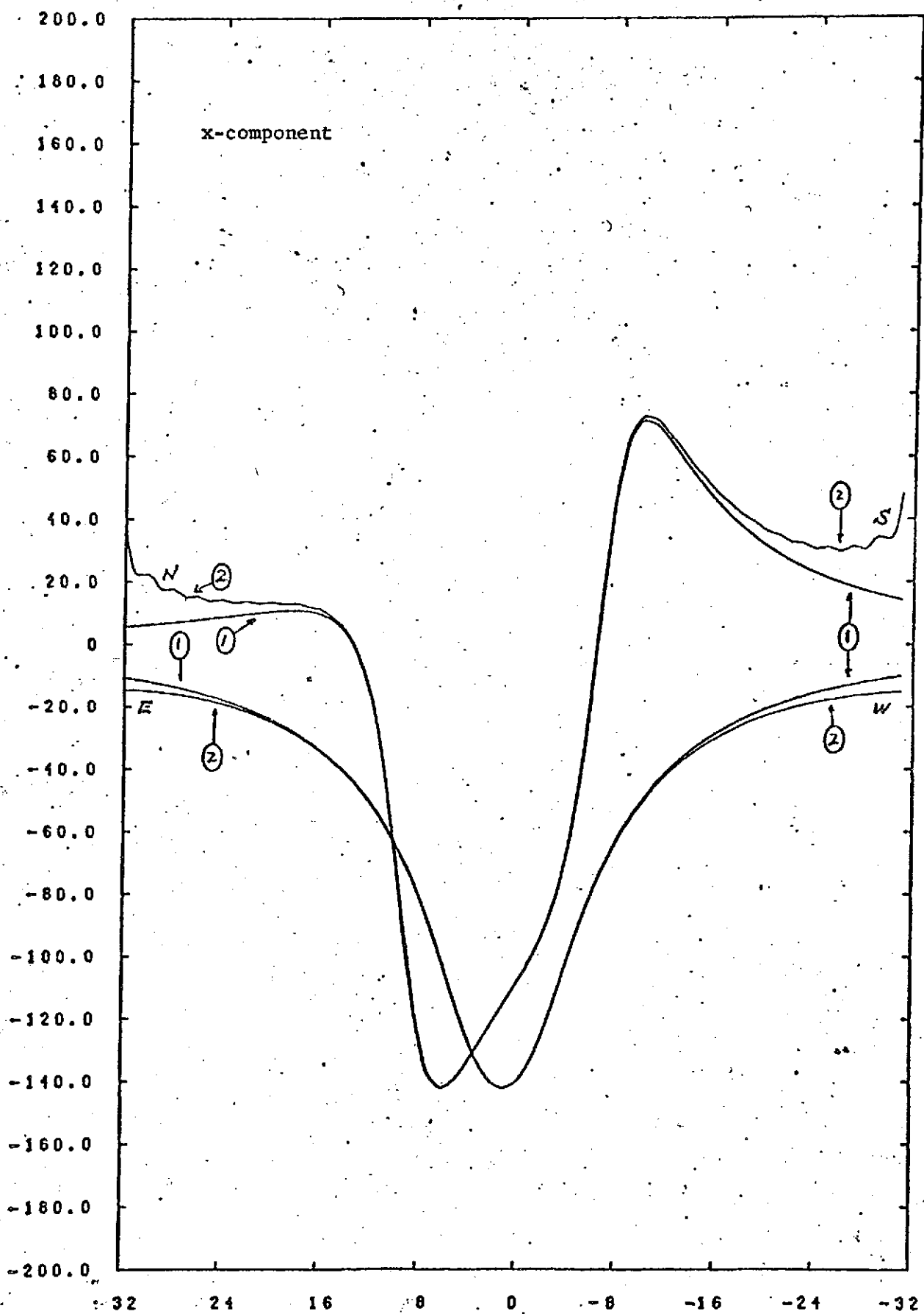


Figure 8

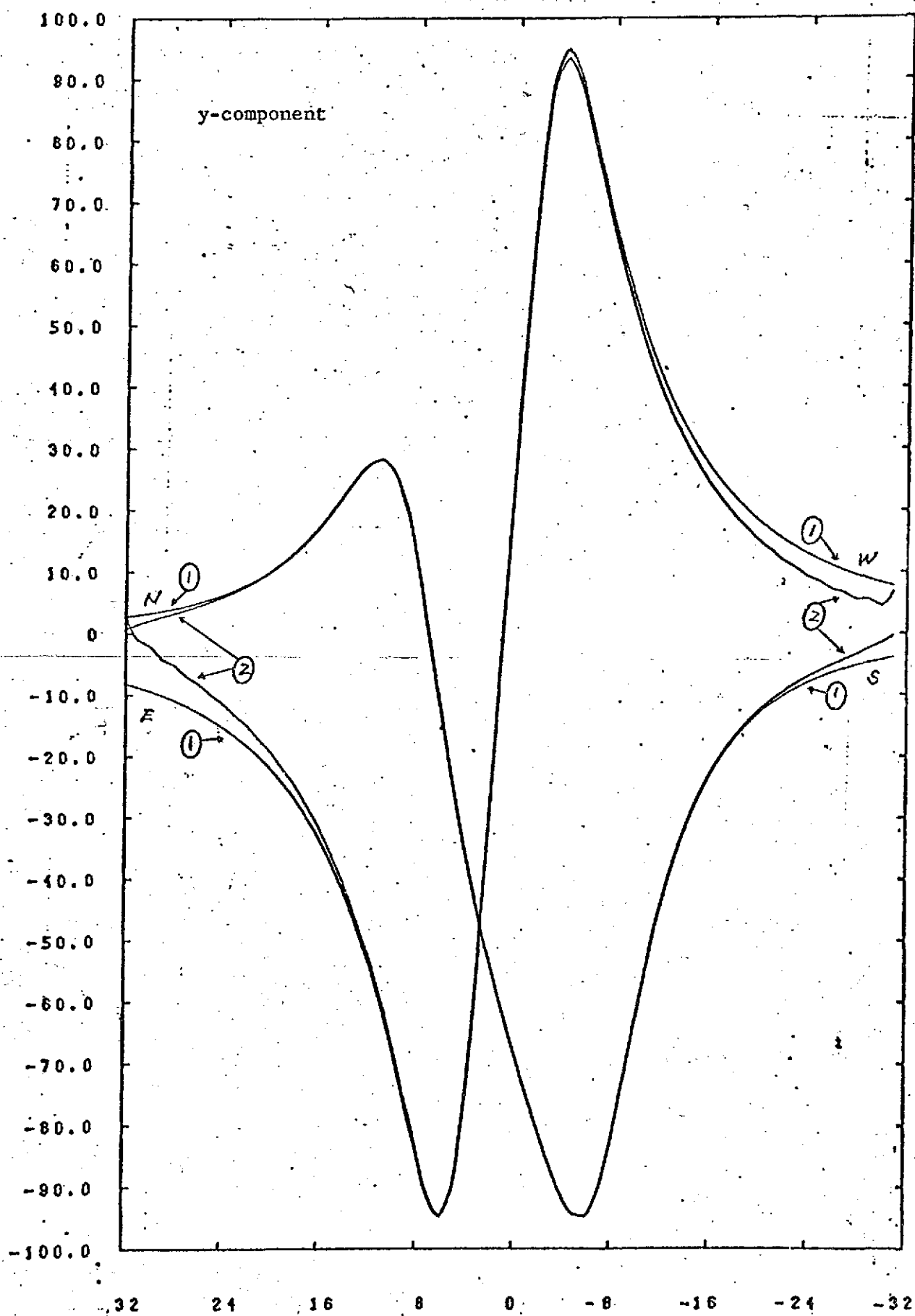
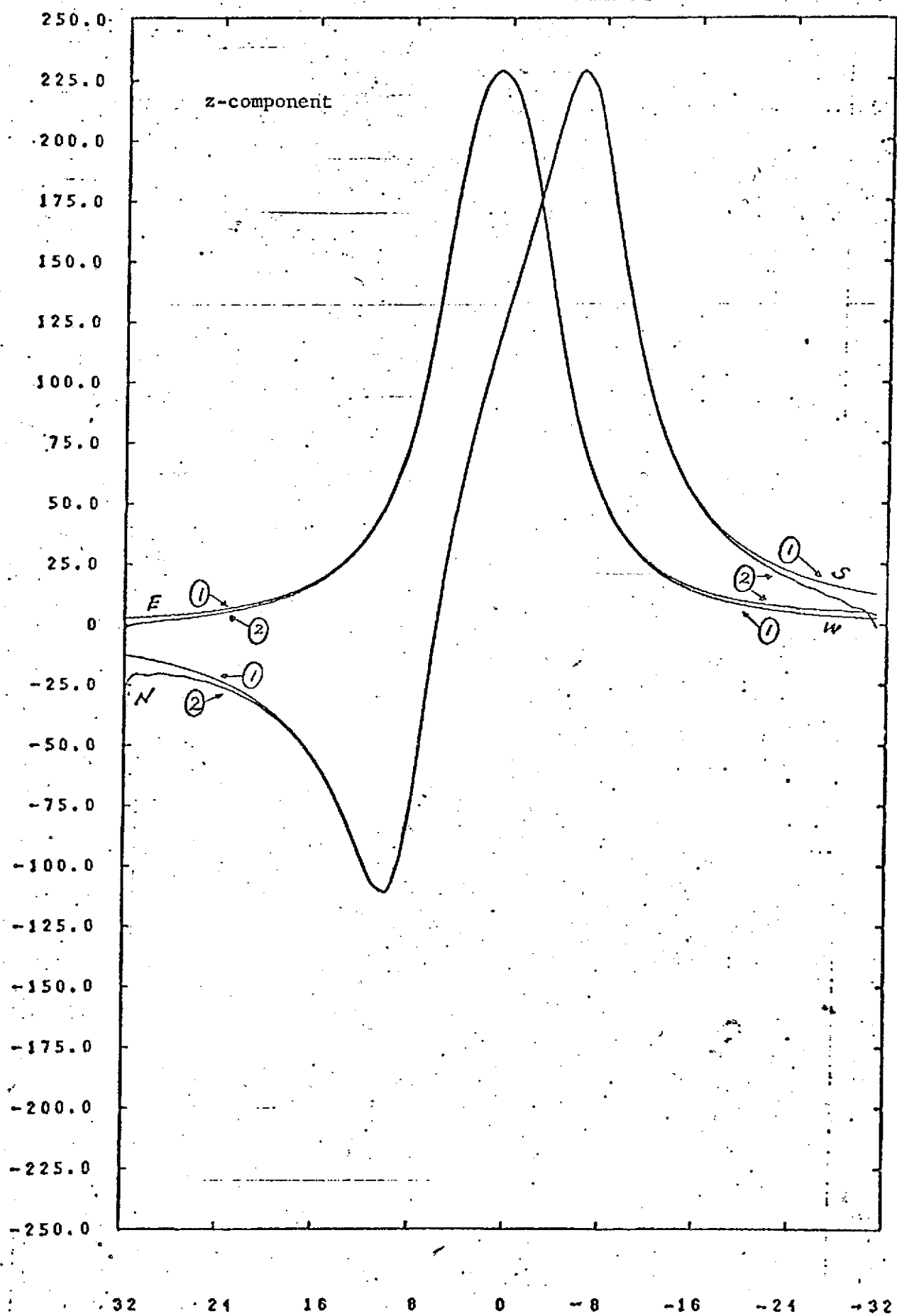


Figure 9





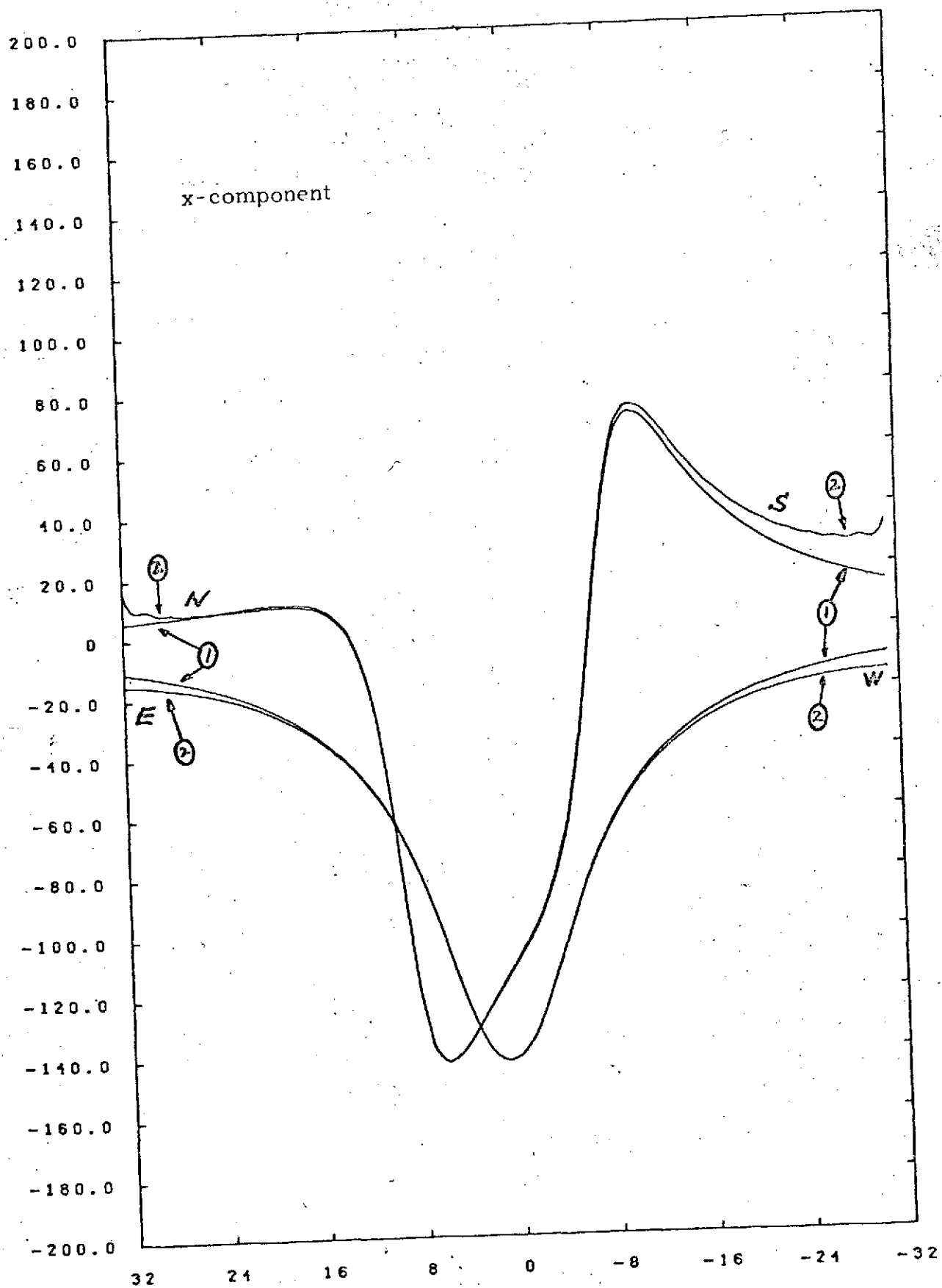


Figure 11

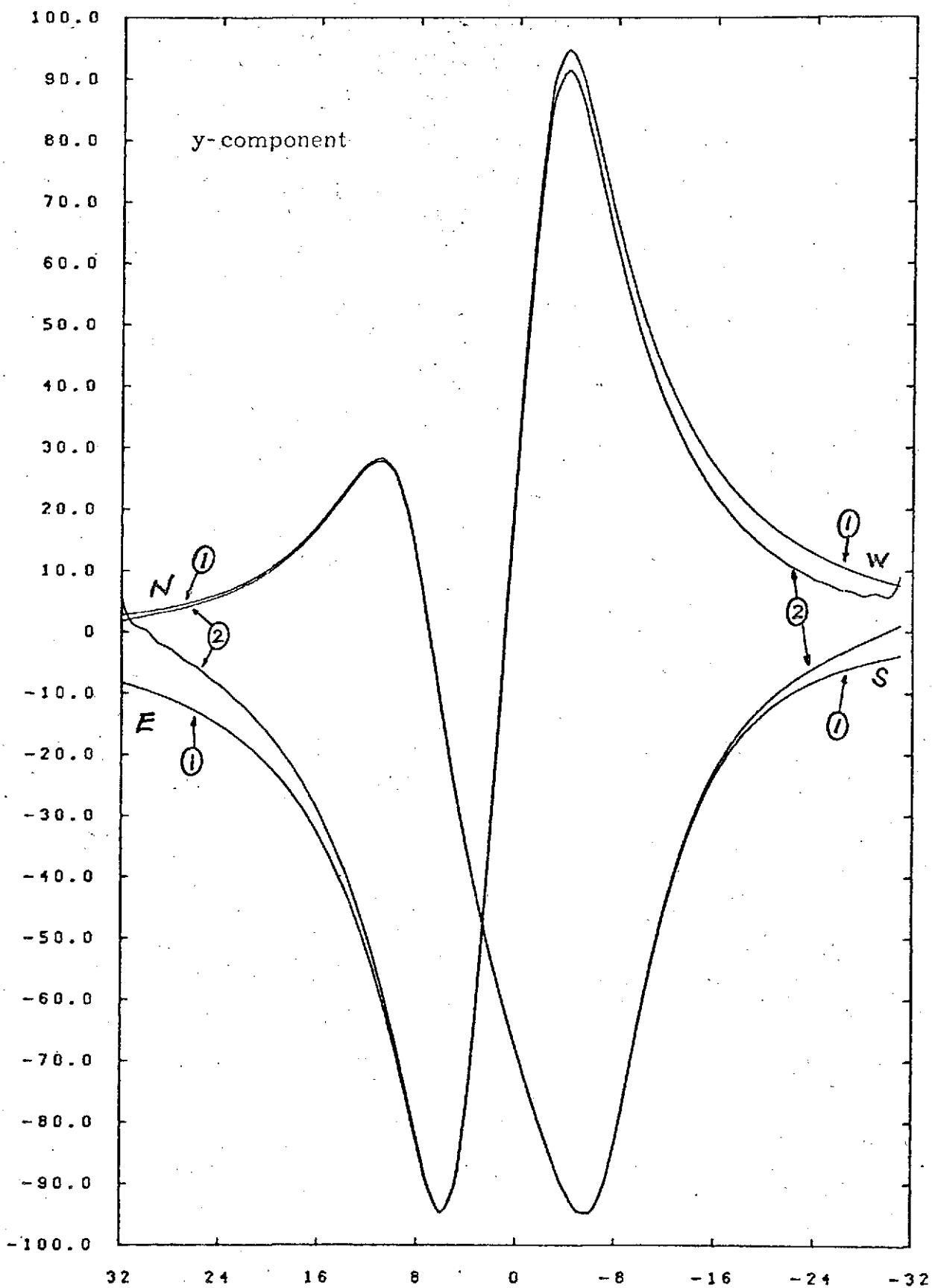


Figure 12

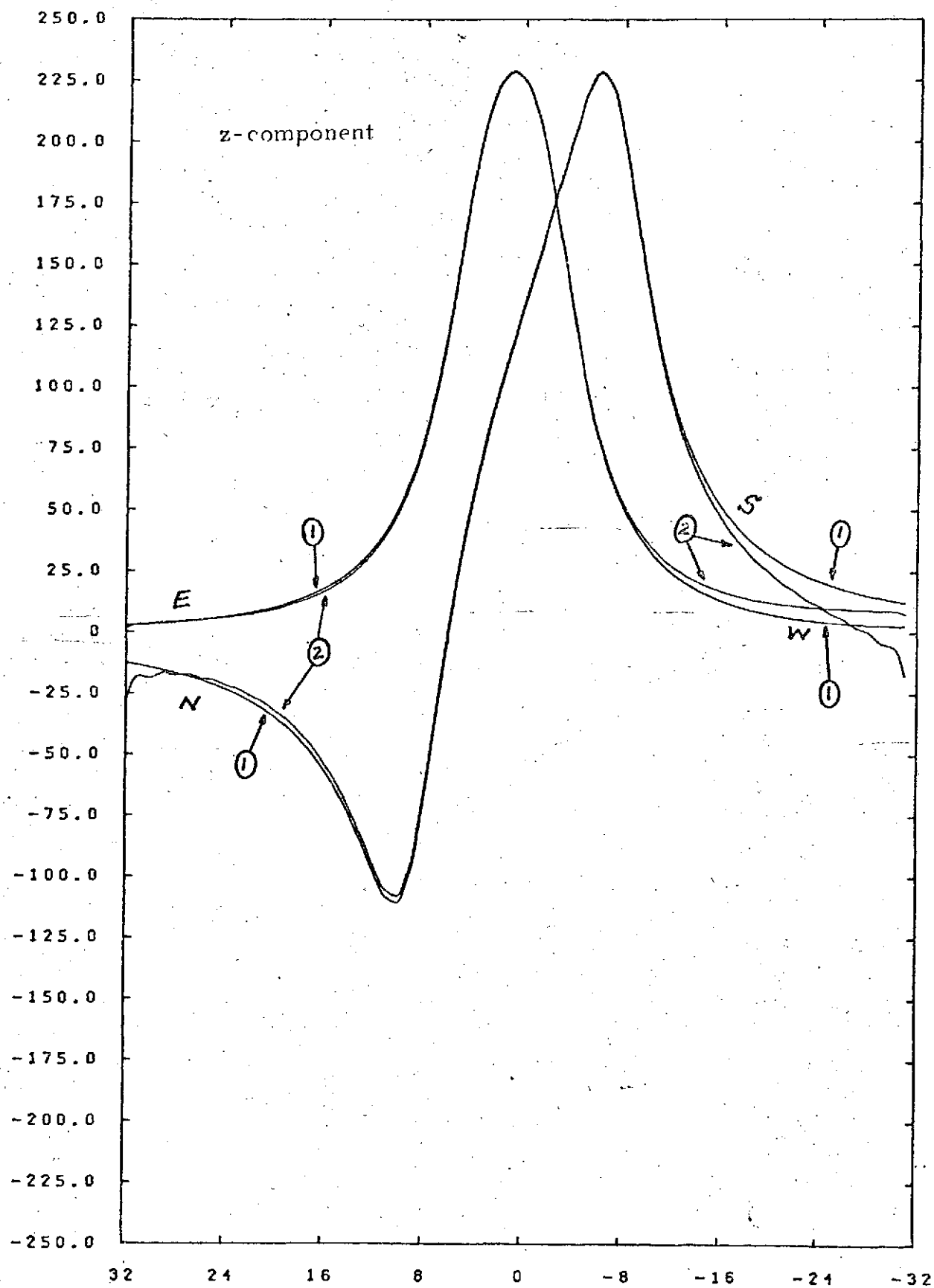


Figure 13

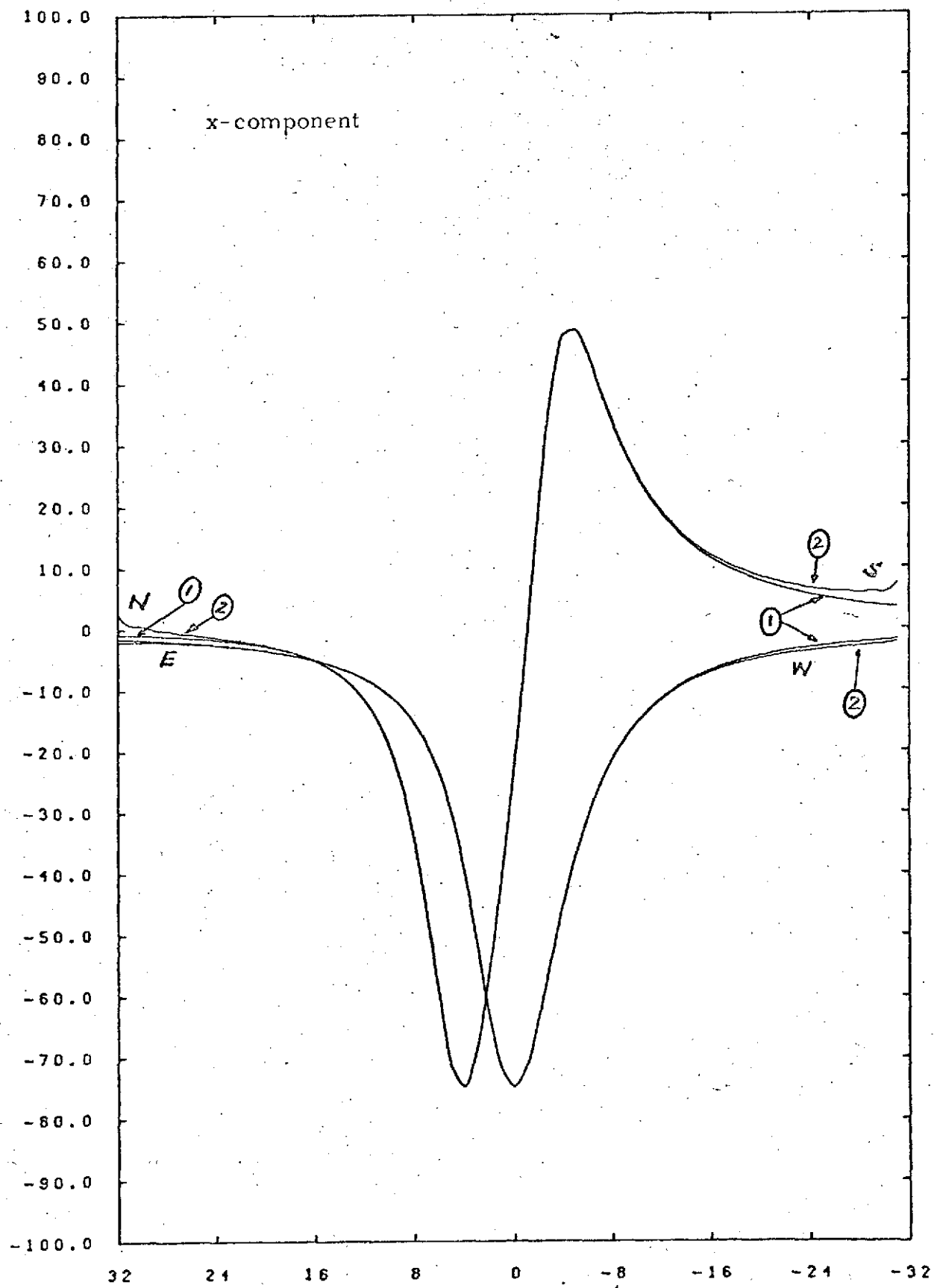


Figure 14

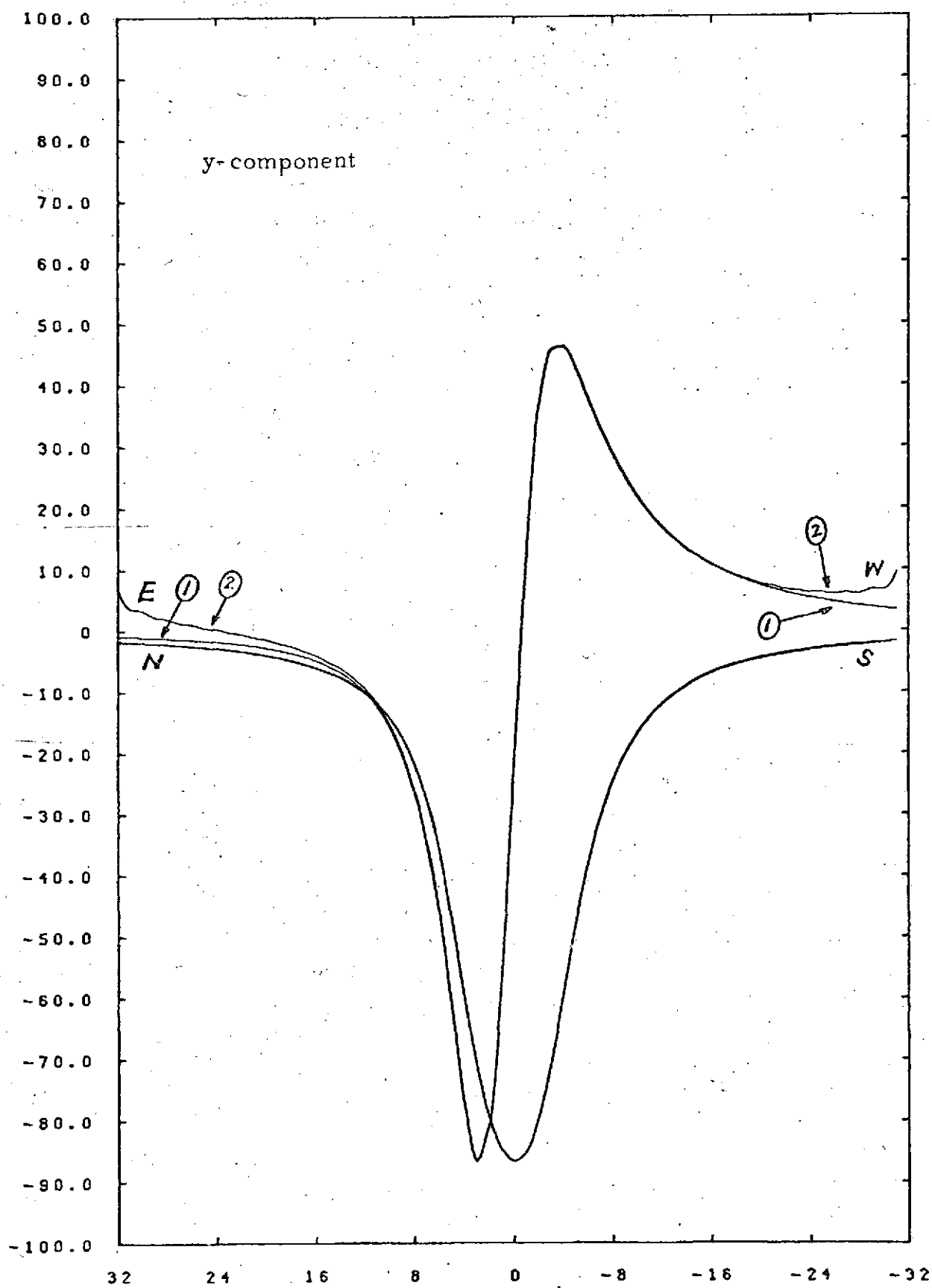


Figure 15

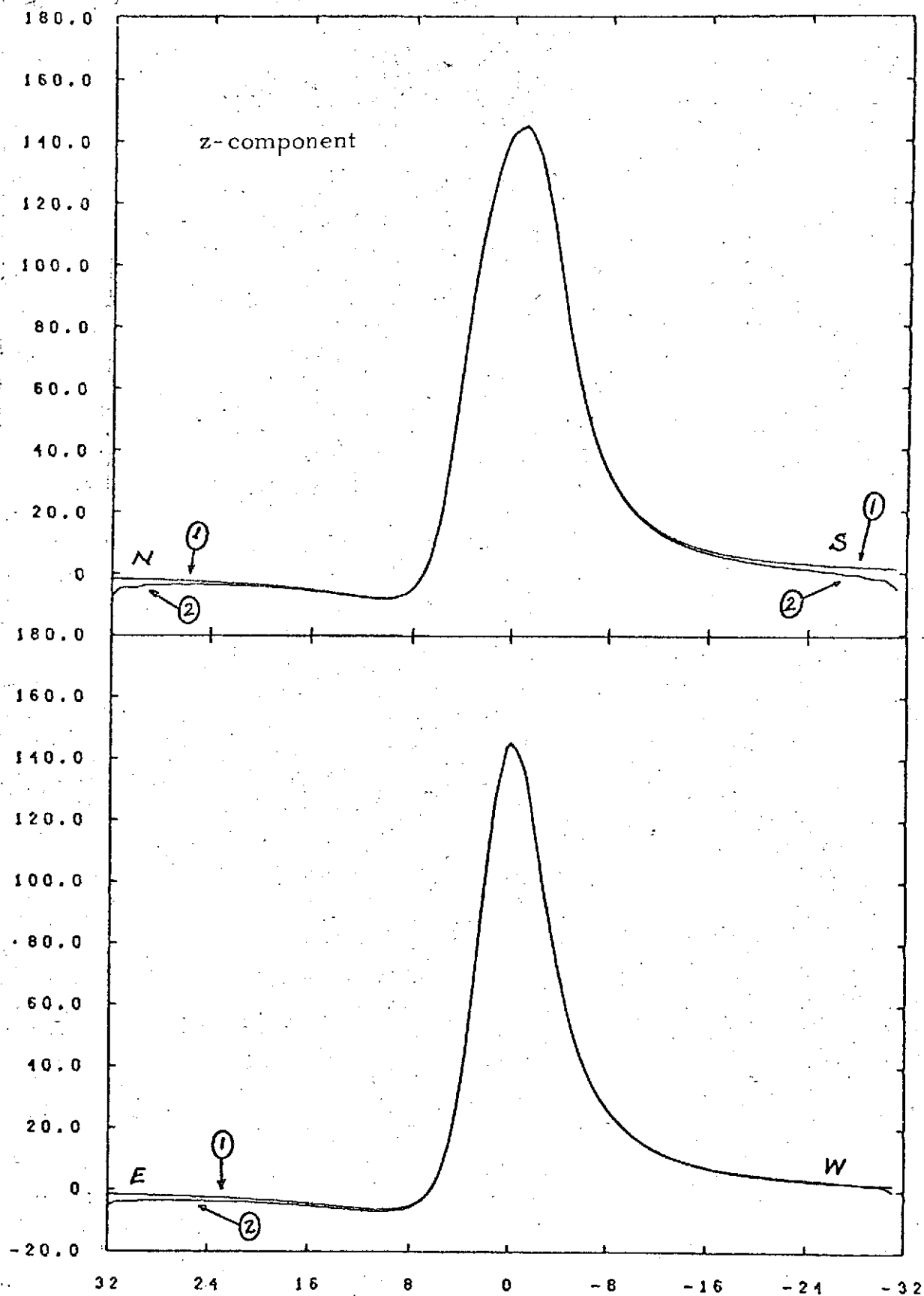


Figure 16

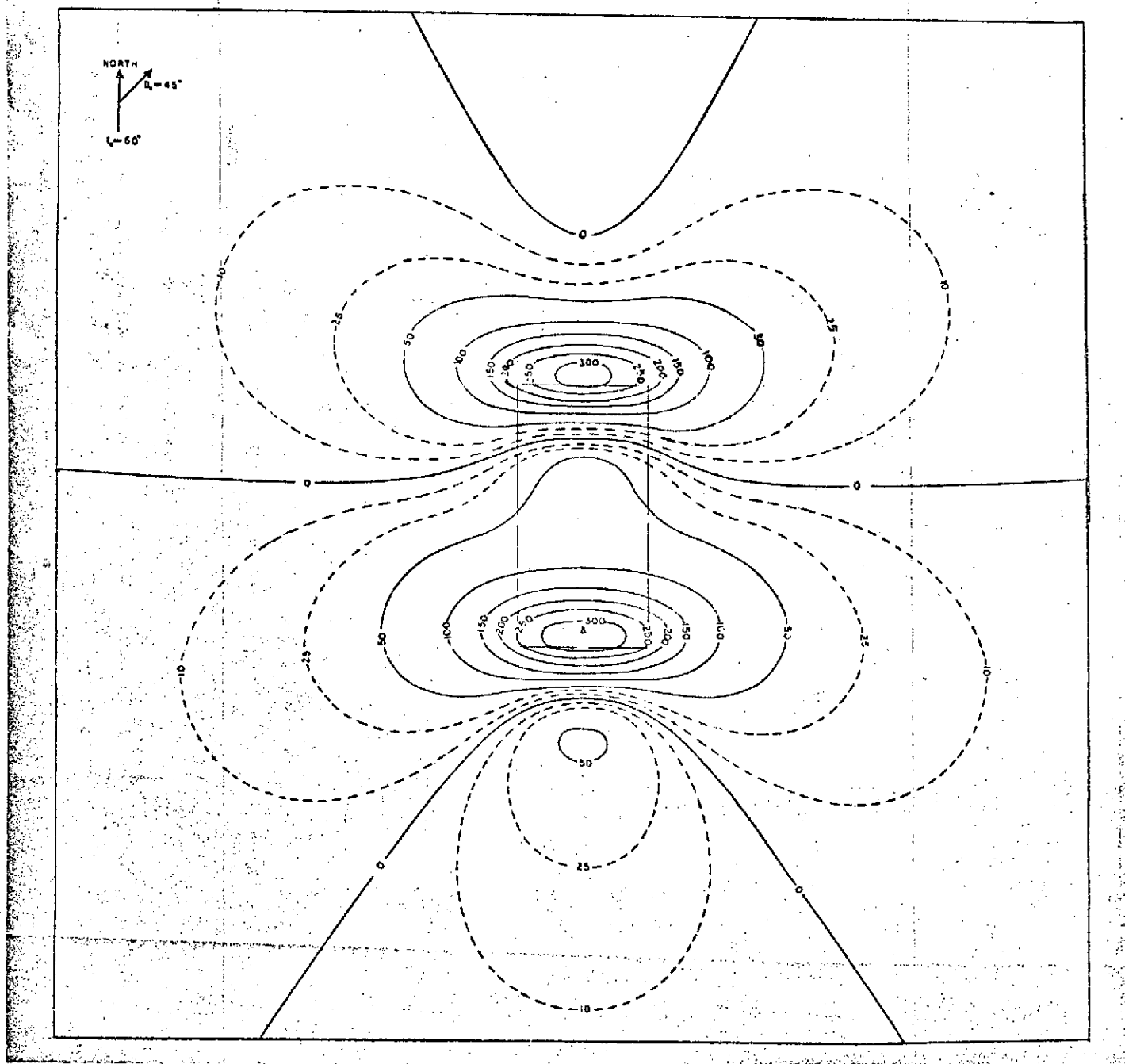


Figure 17

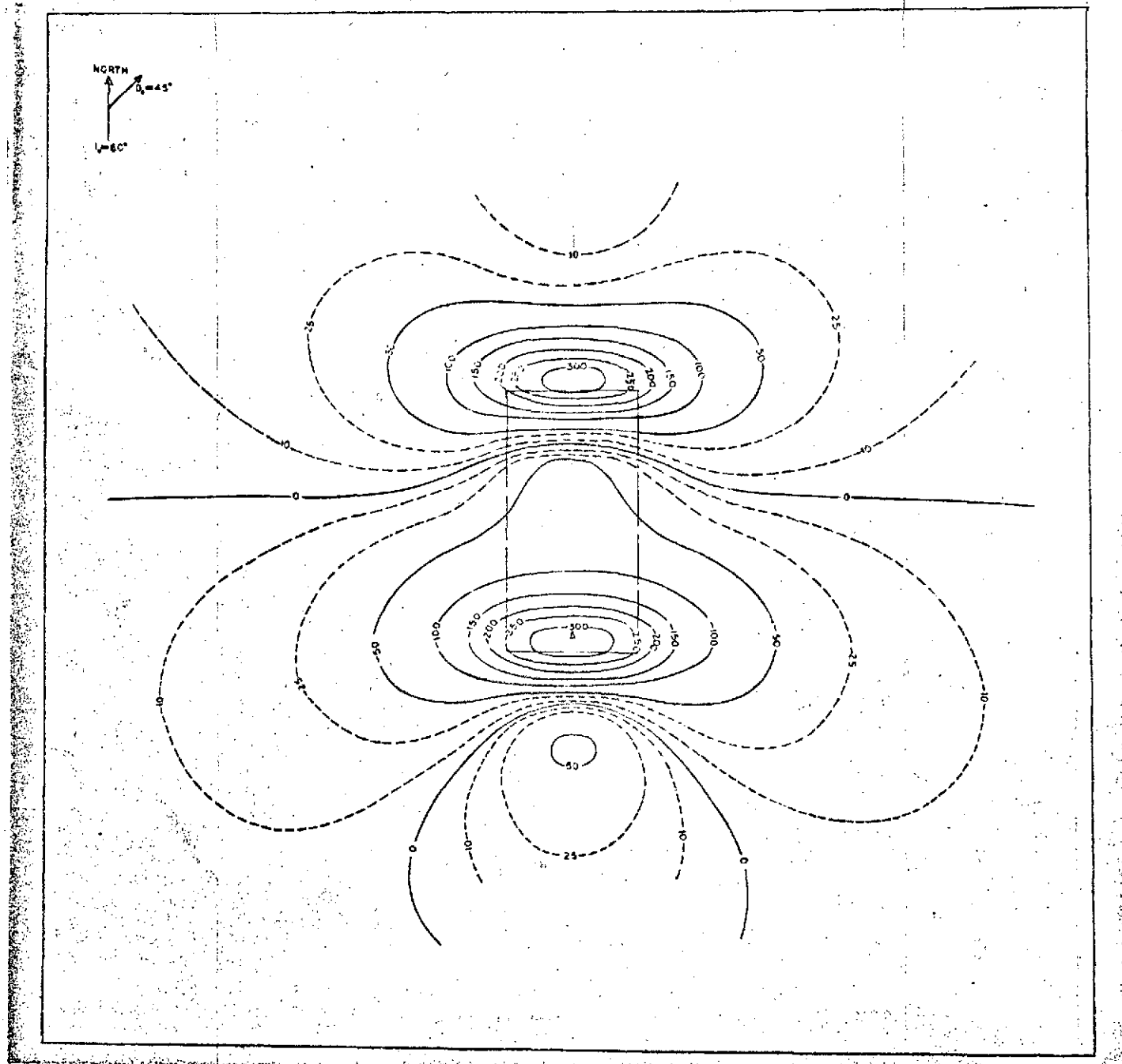


Figure 18



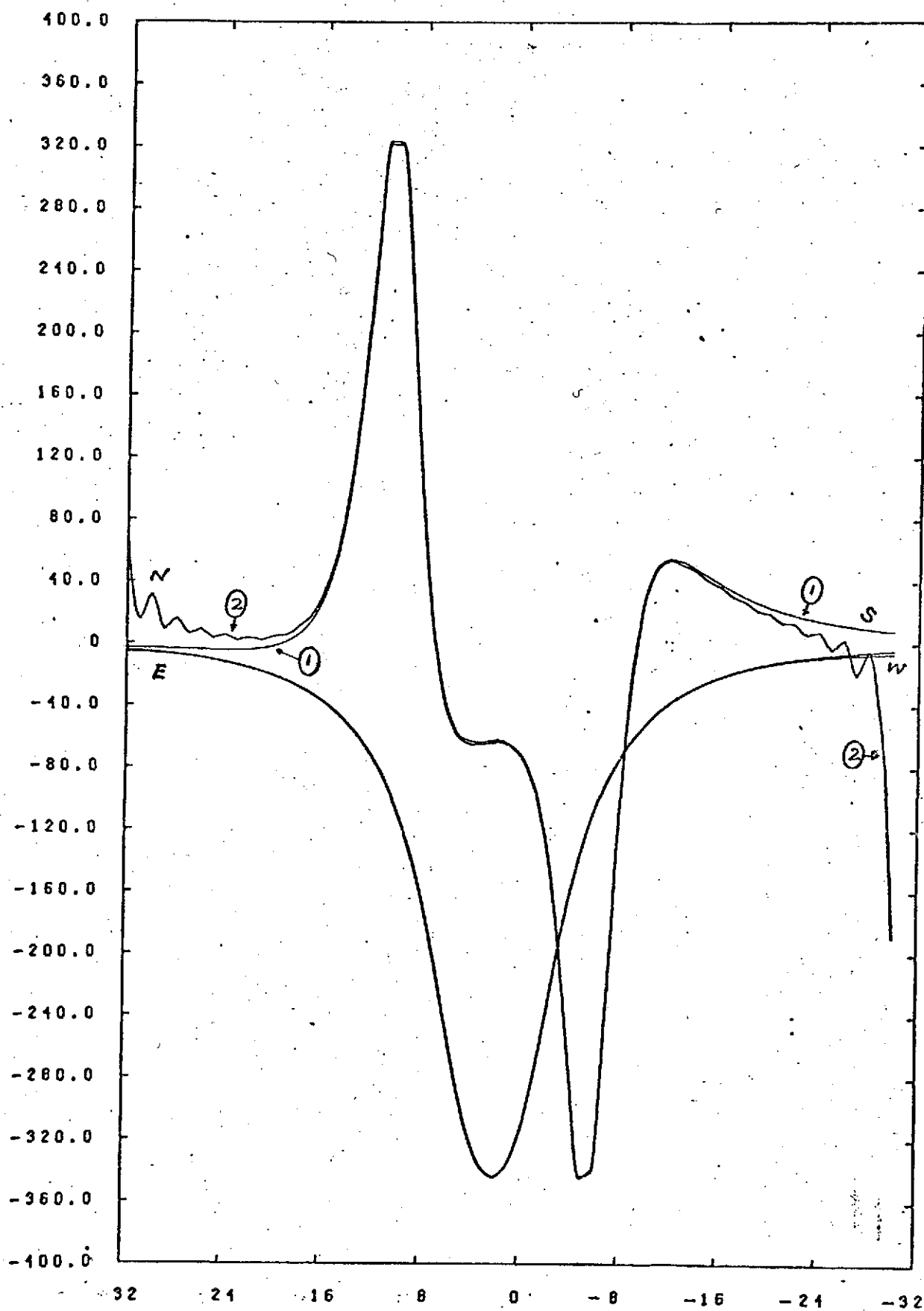


Figure 19

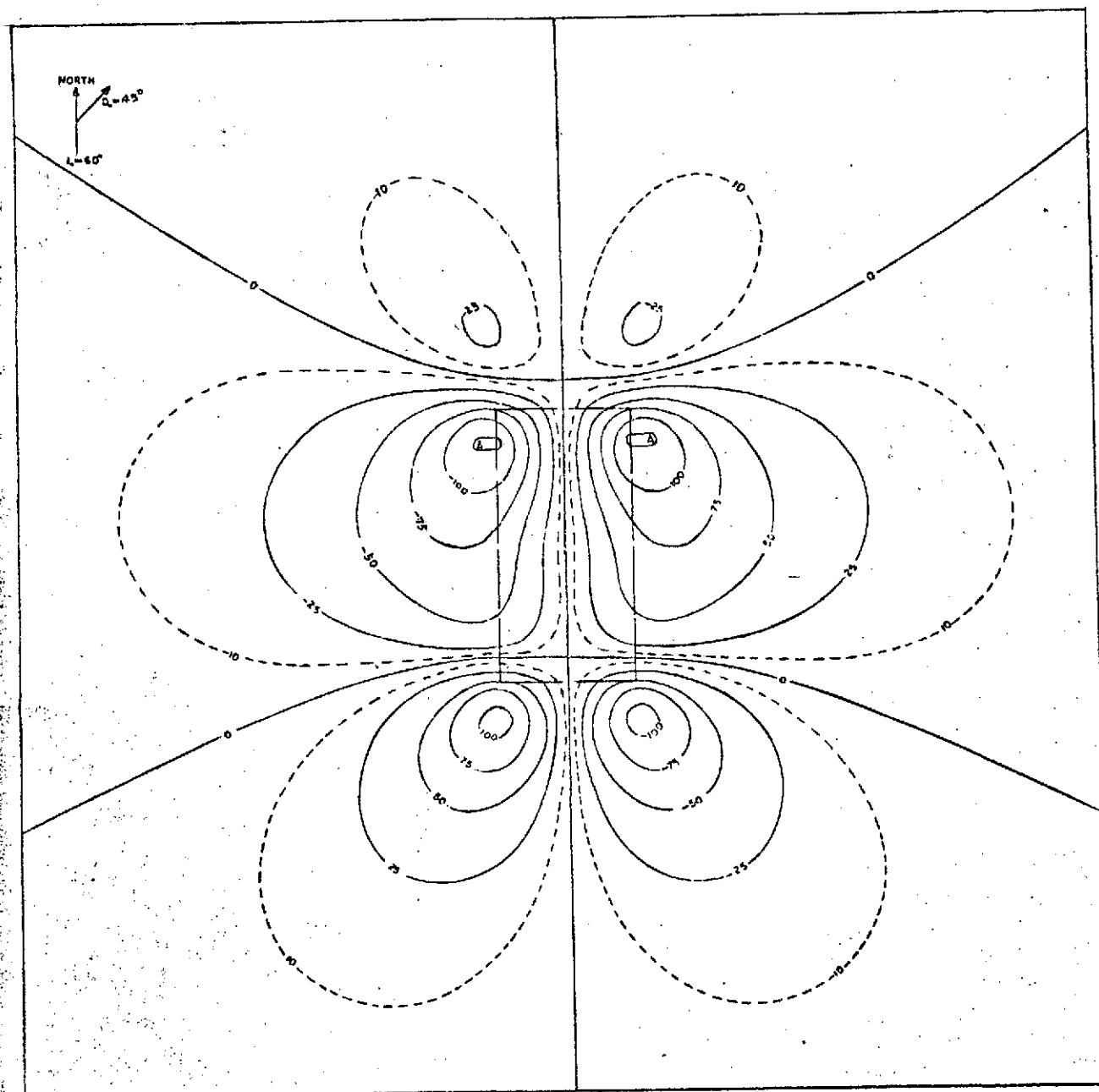


Figure 20

REPRODUCIBILITY OF THE  
ORIGINAL PAGE IS POOR.

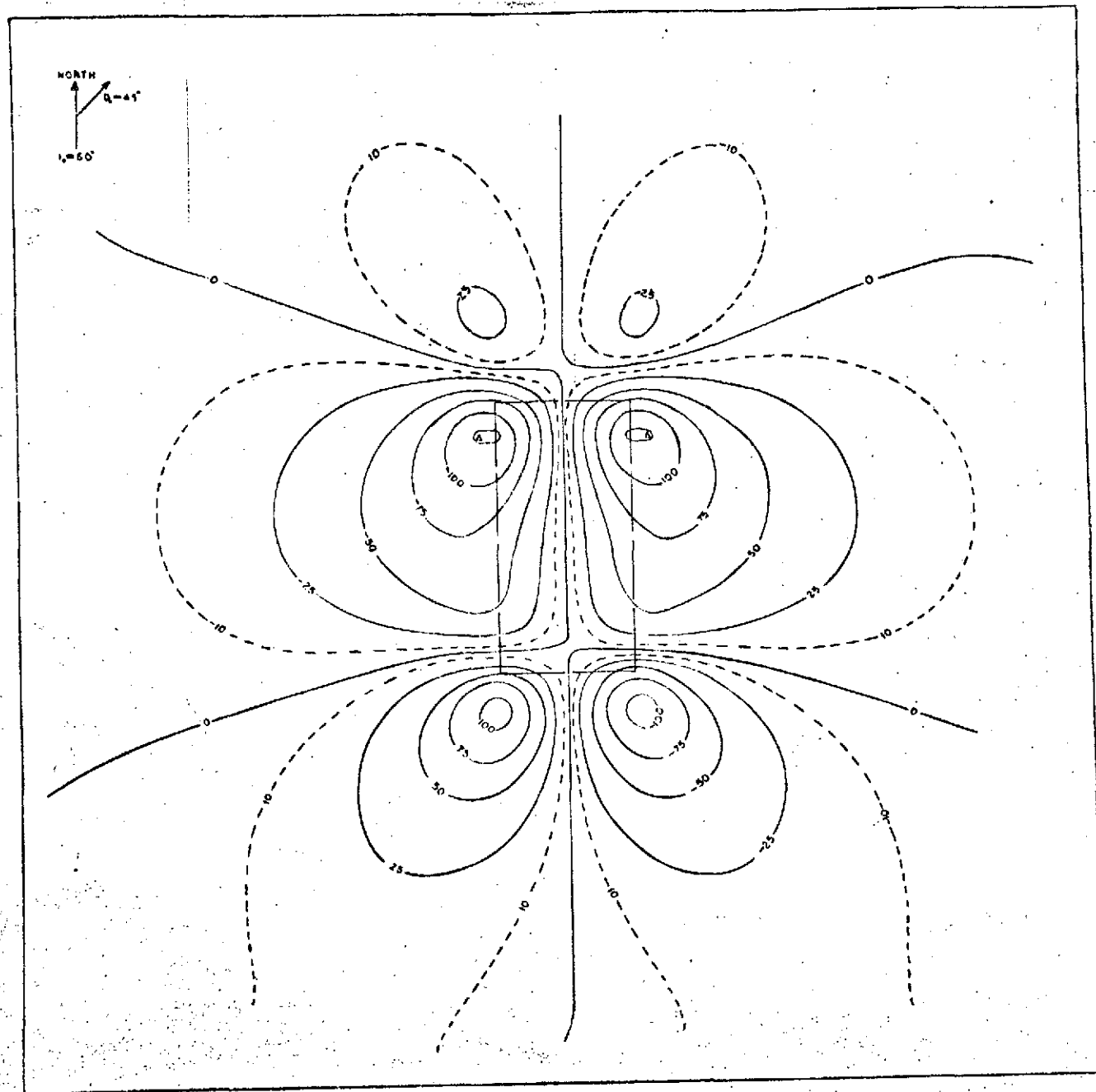


Figure 21

REPRODUCIBILITY OF THE  
ORIGINAL PAGE IS POOR.

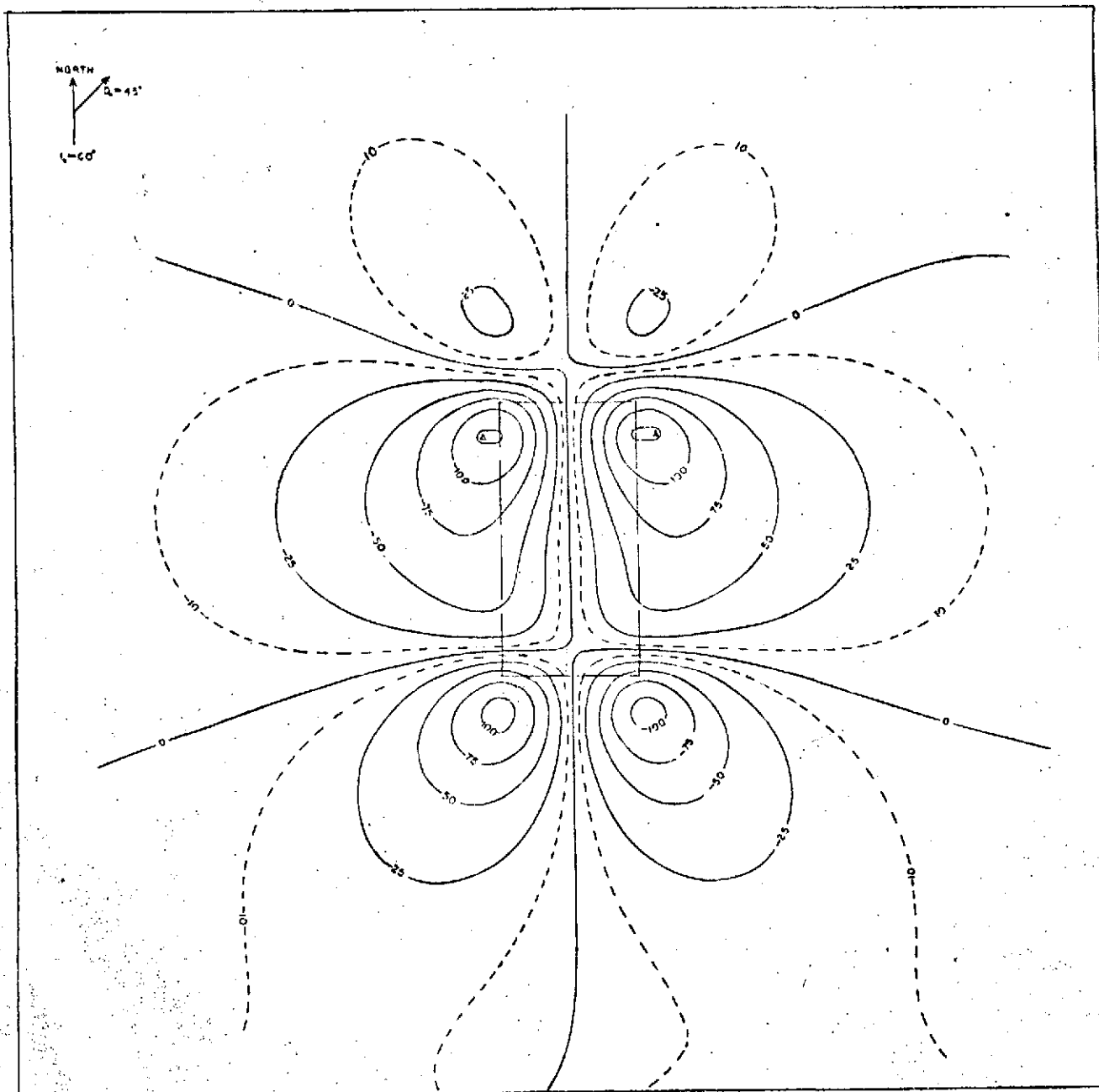


Figure 22

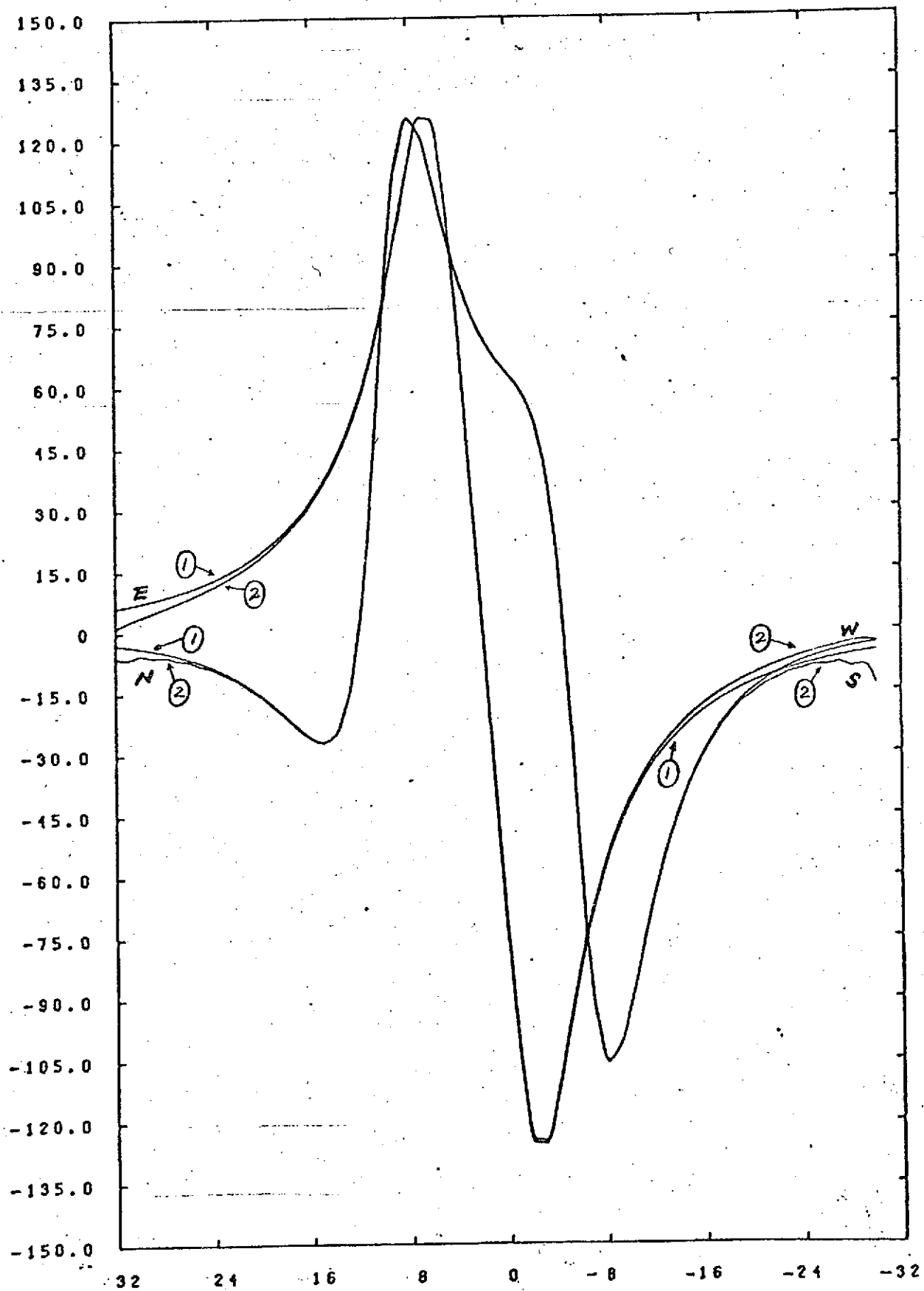
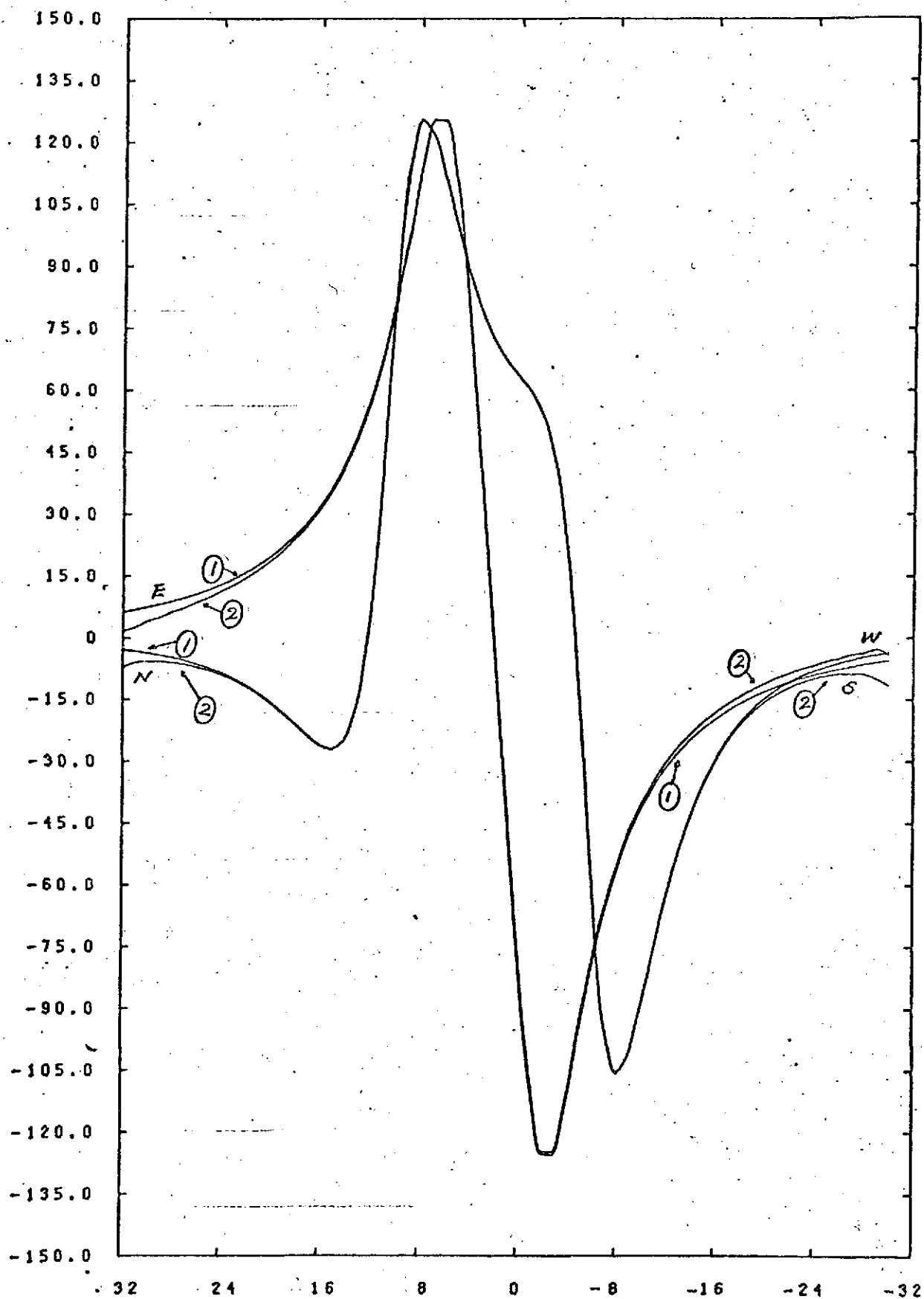


Figure 23



REPRODUCIBILITY OF THE  
ORIGINAL PAGE IS POOR

Figure 24

REPRODUCIBILITY OF THE  
ORIGINAL PAGE IS POOR

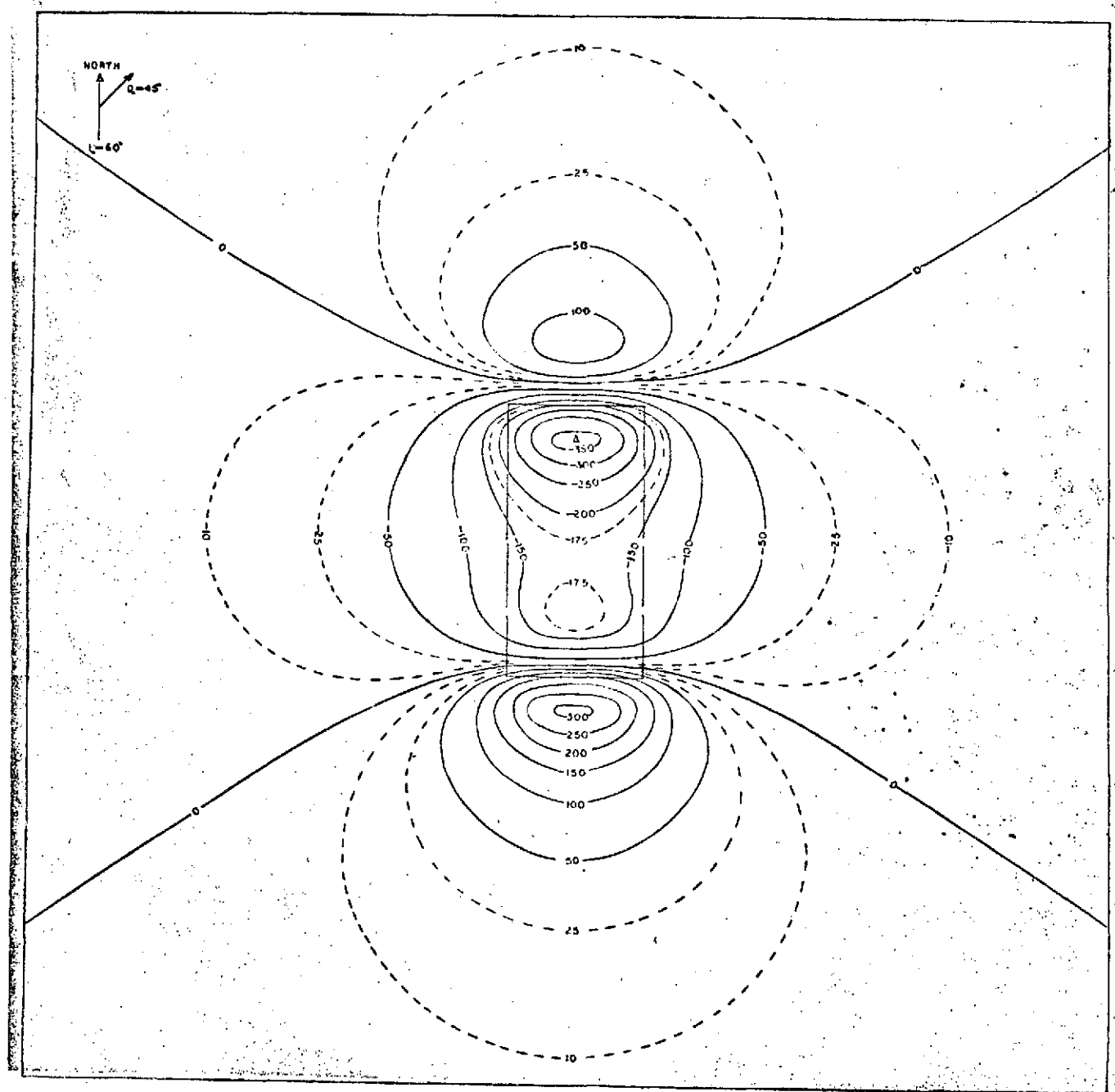


Figure 25

REPRODUCIBILITY OF THE  
ORIGINAL PAGE IS POOR

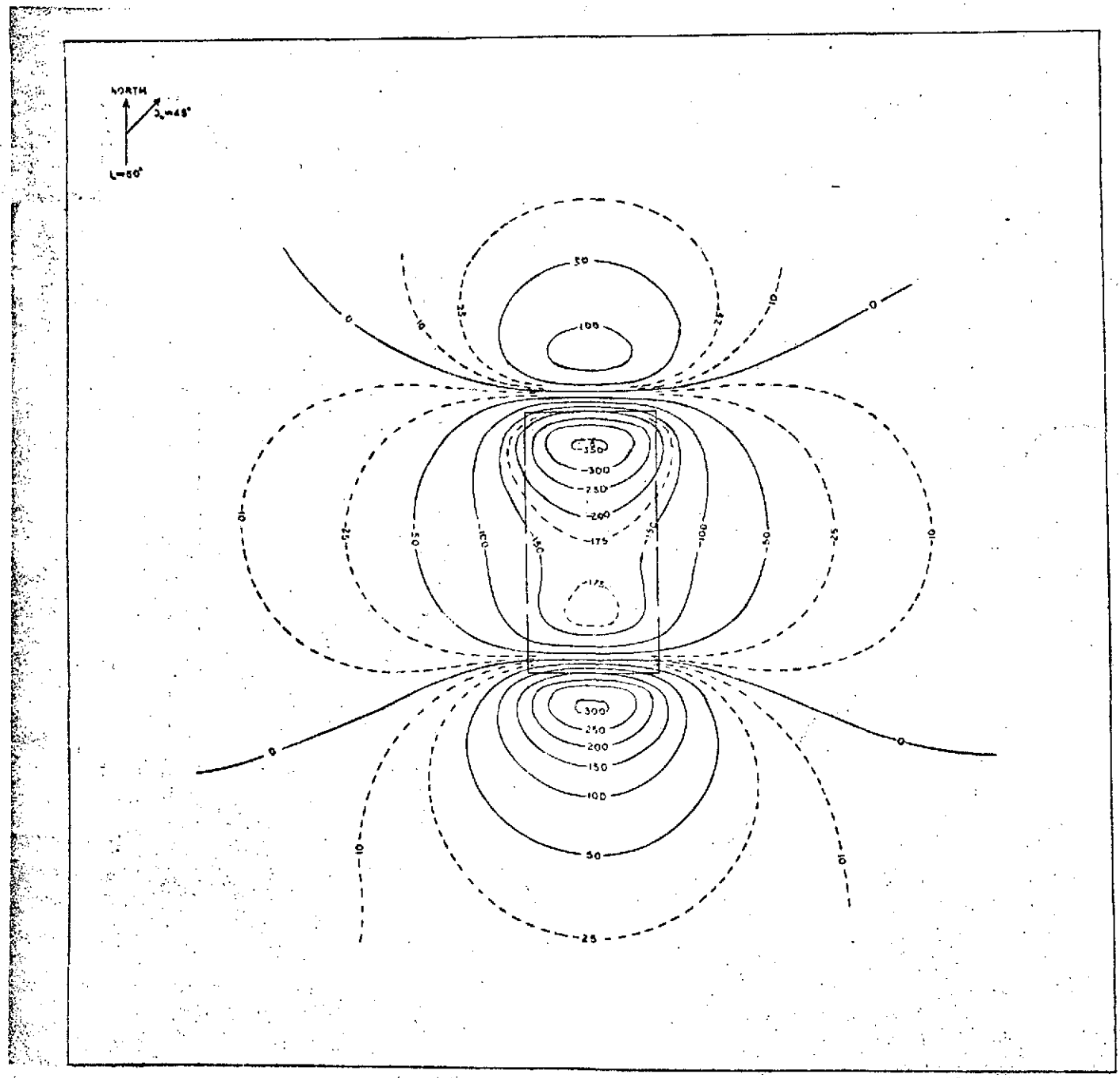


Figure 26



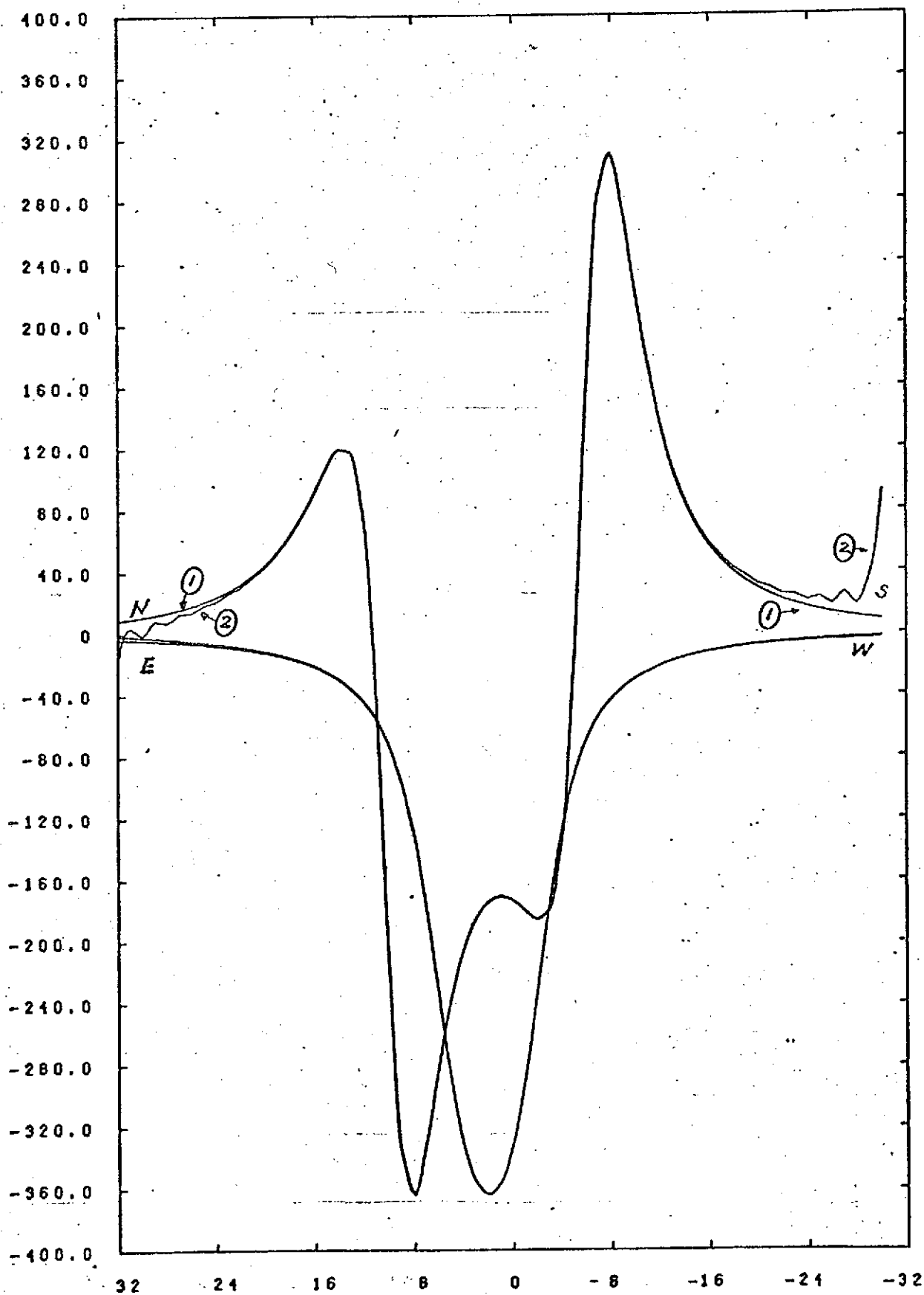


Figure 27

REPRODUCIBILITY OF THE  
ORIGINAL PAGE IS POOR

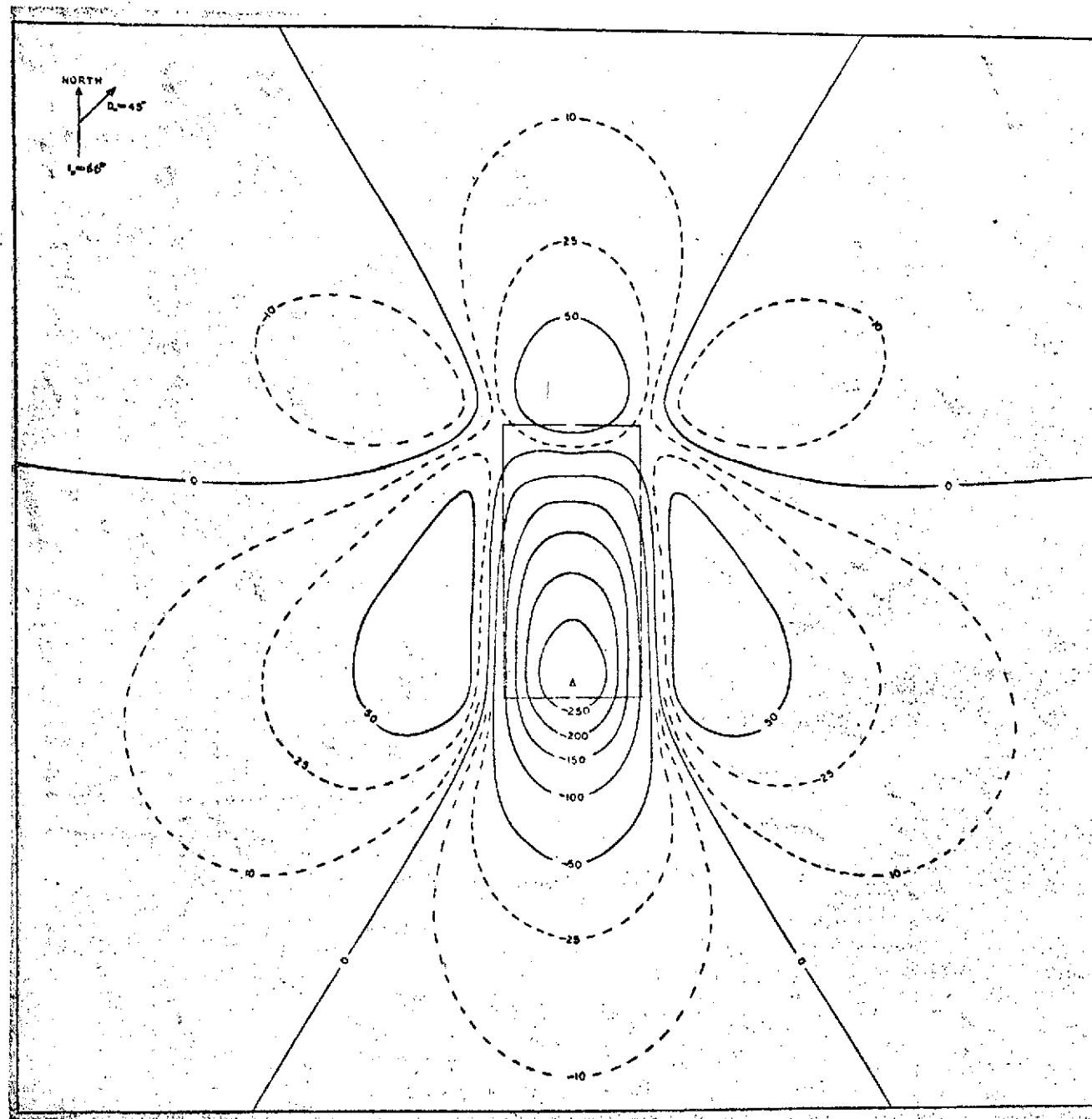


Figure 28

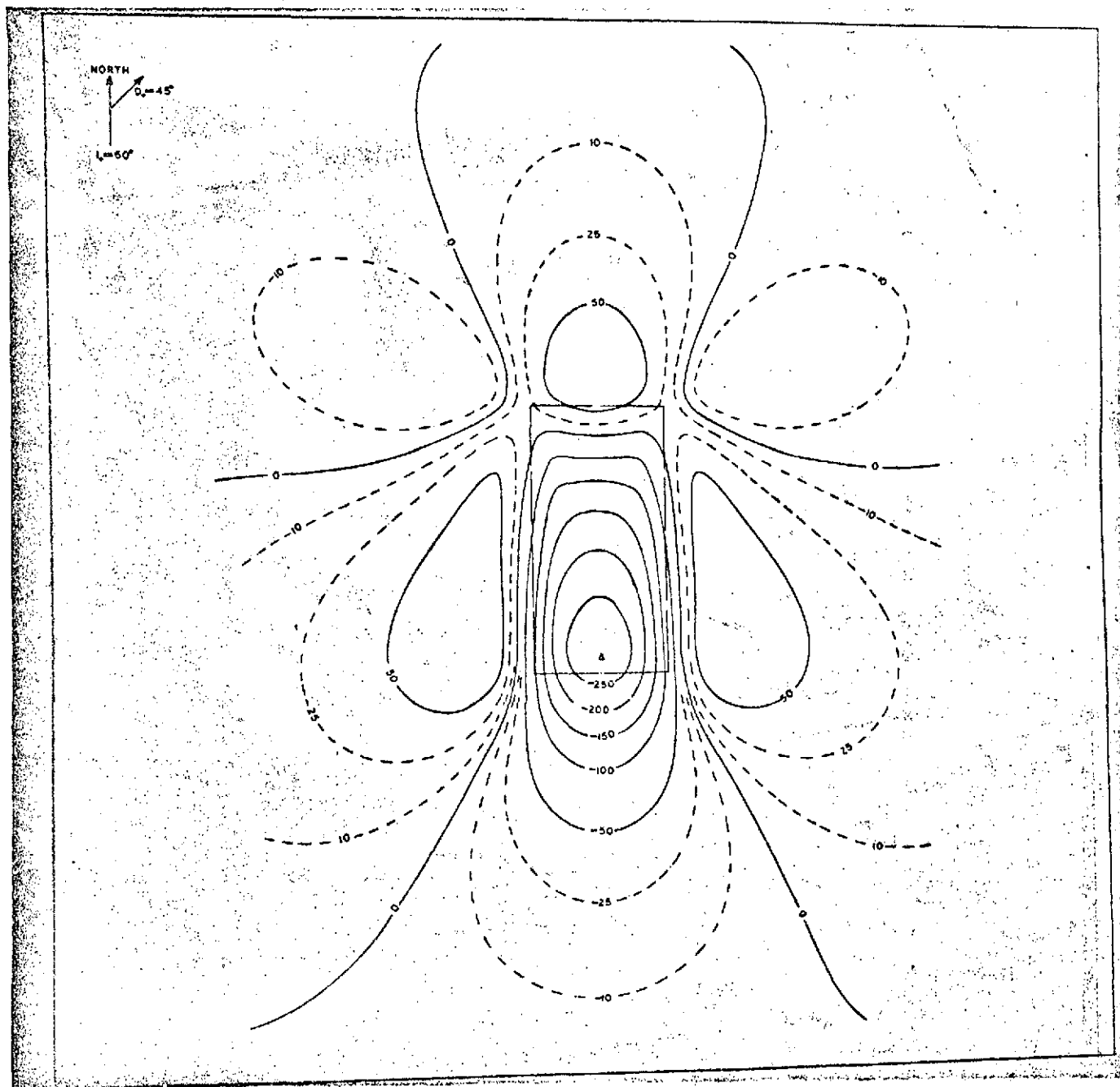


Figure 29

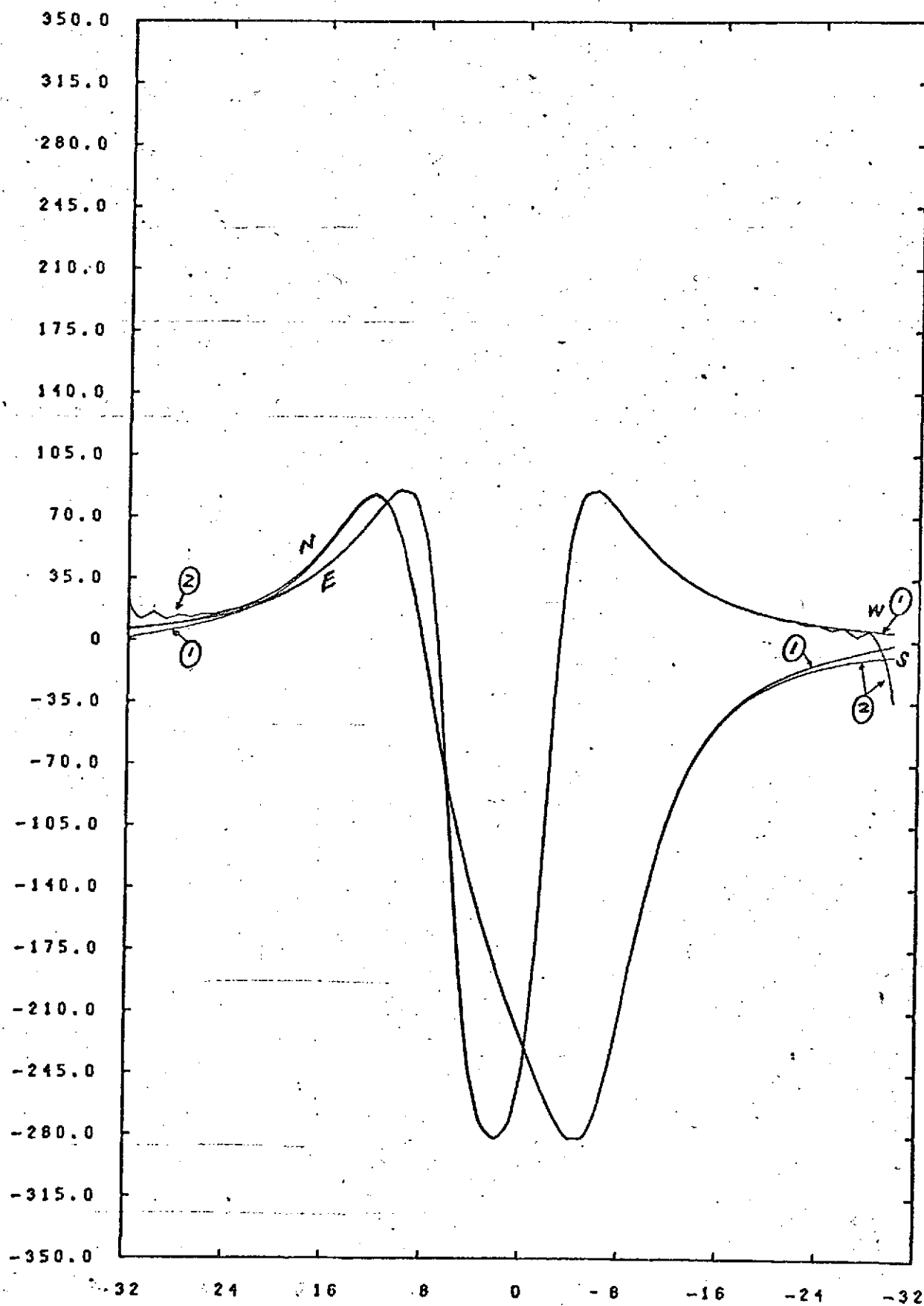


Figure 30

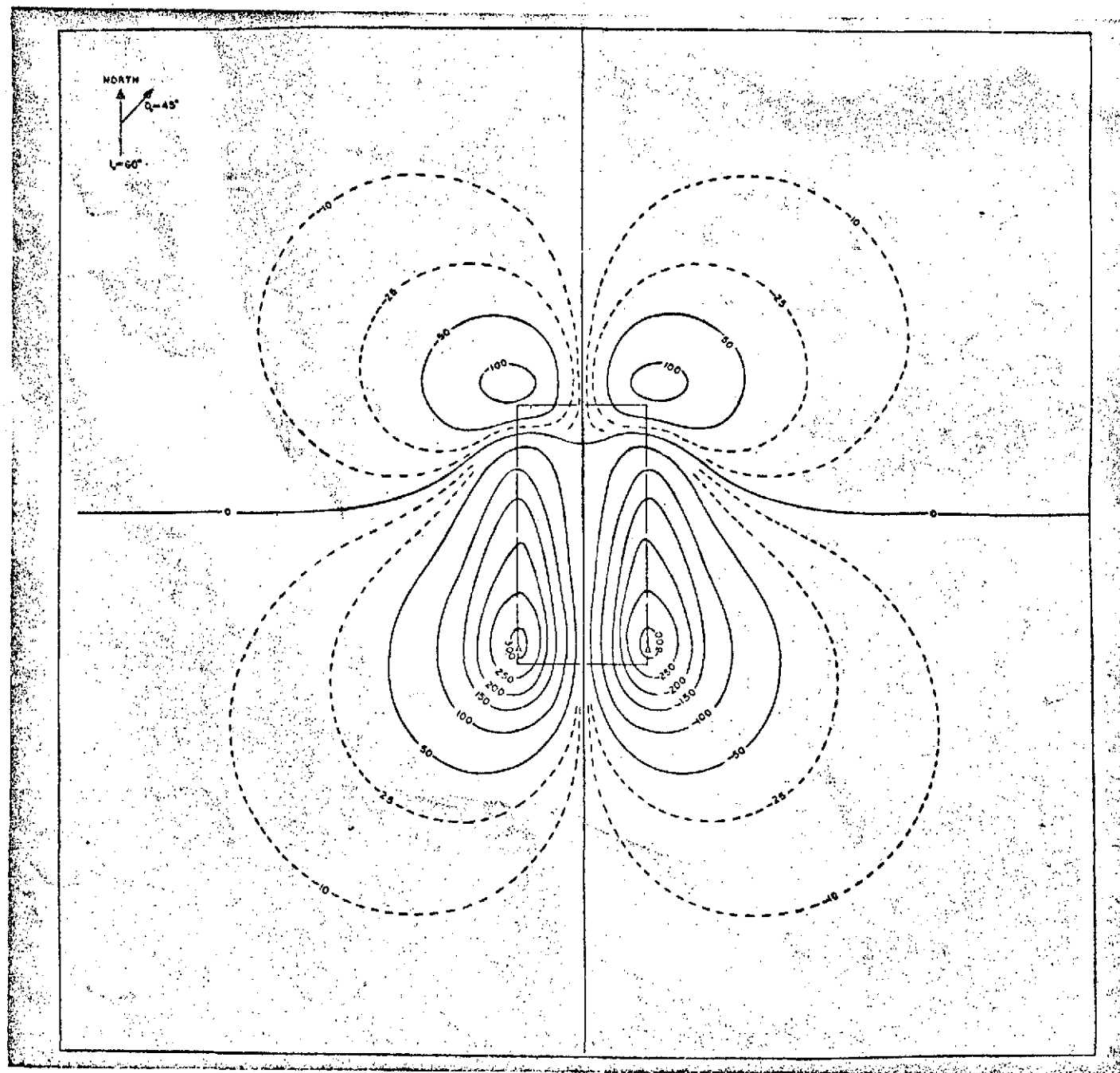


Figure 31

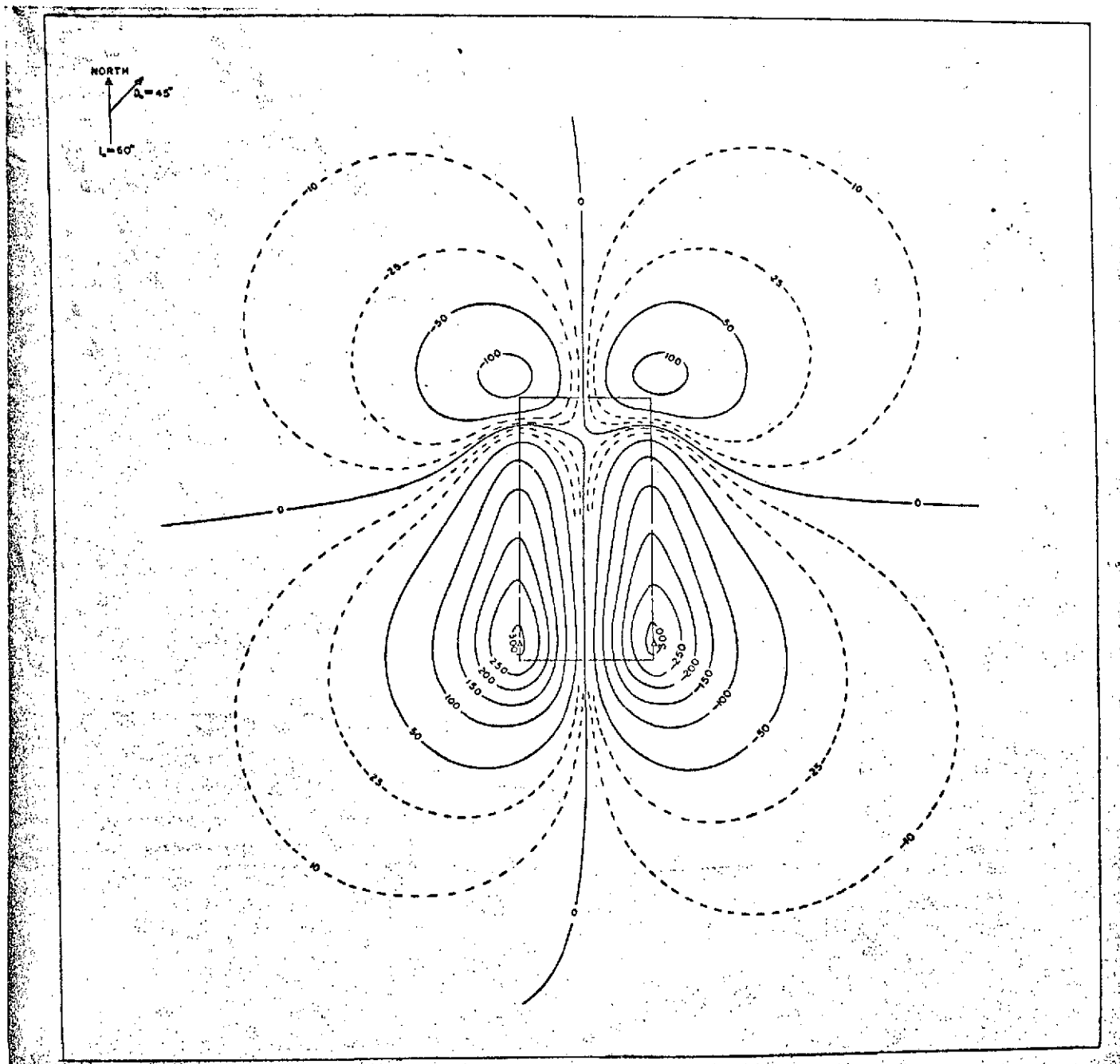


Figure 32

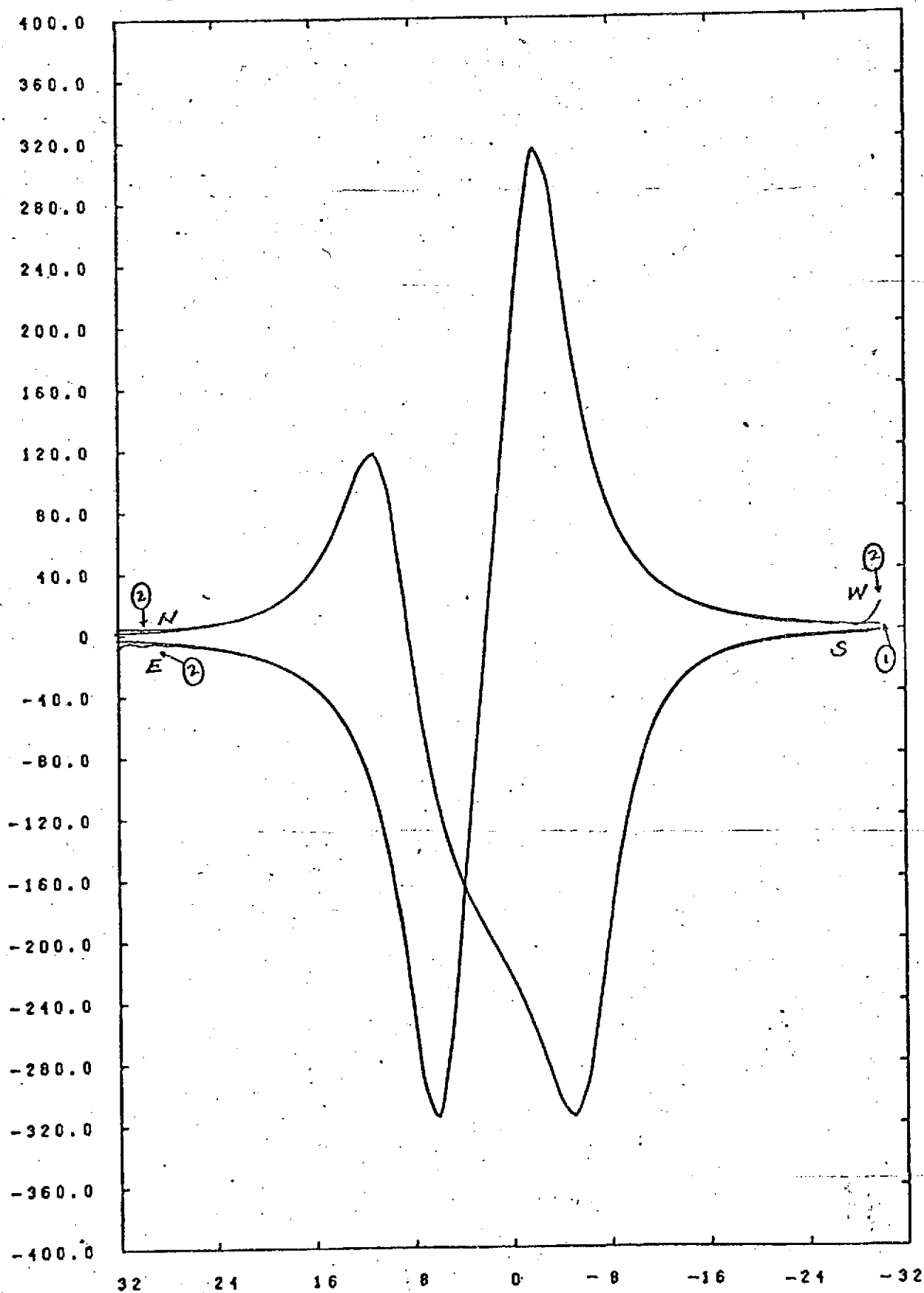


Figure 33

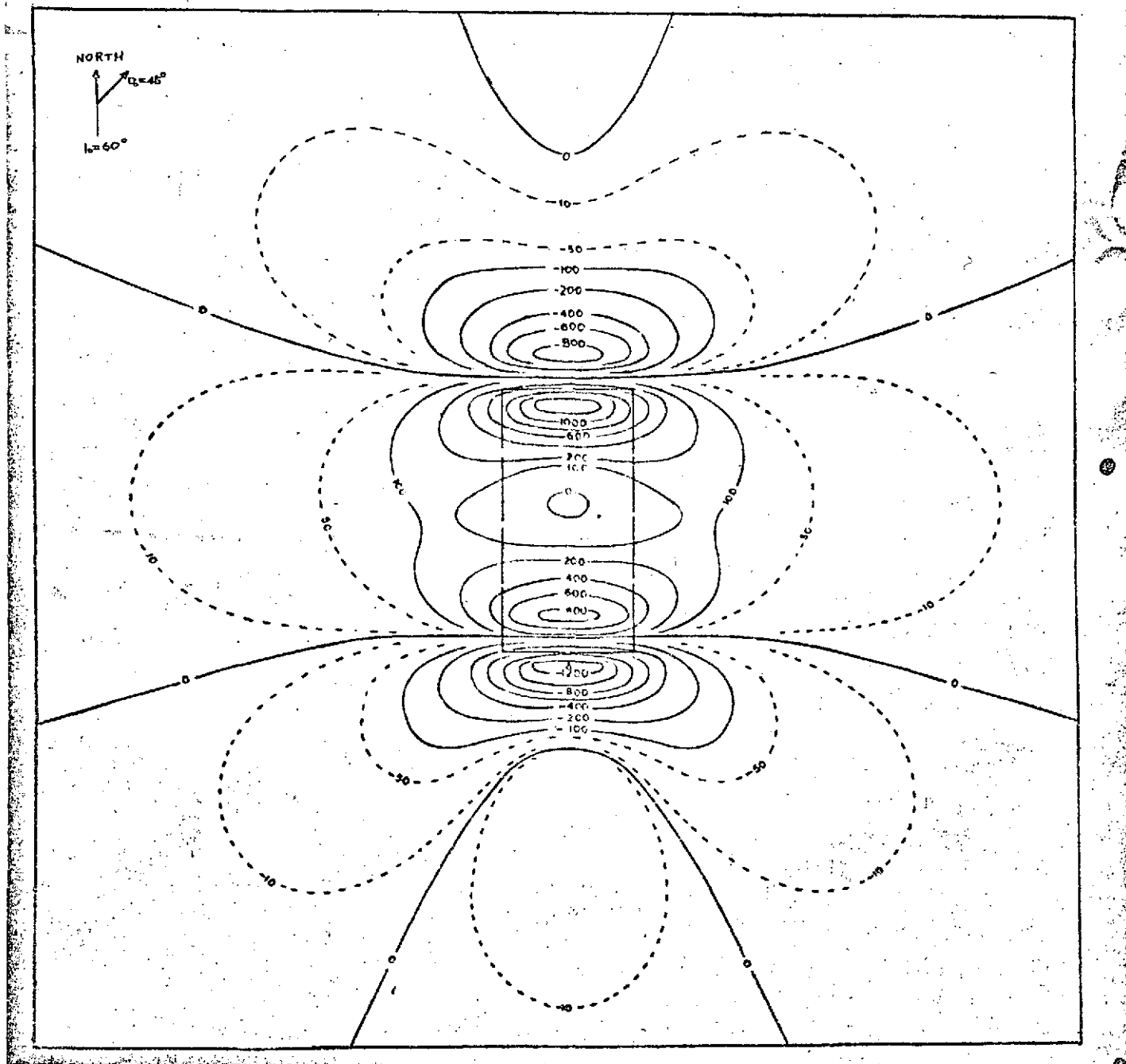


Figure 34



REPRODUCIBILITY OF THE  
ORIGINAL PAGE IS POOR

NORTH  
 $\theta = 45^\circ$   
 $\phi = 60^\circ$

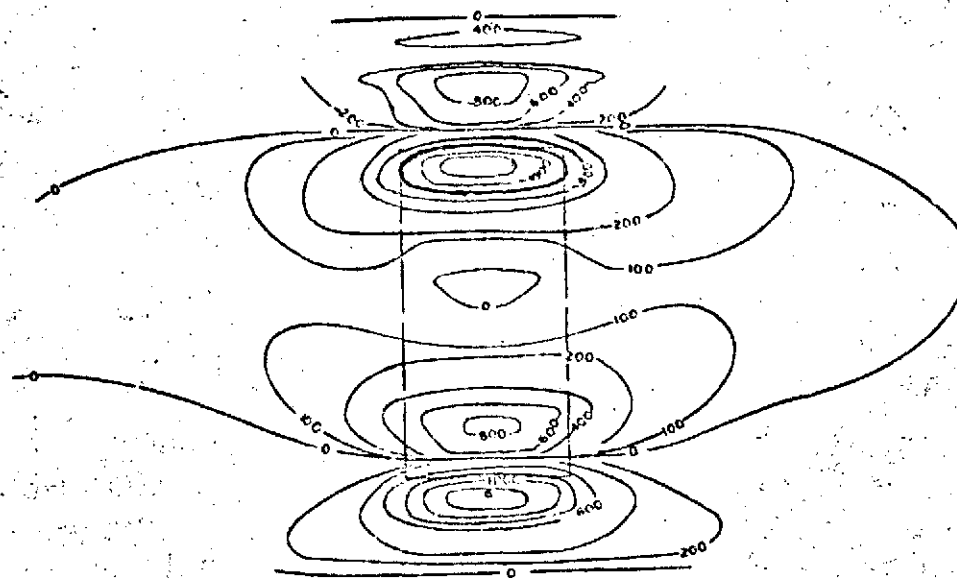


Figure 35

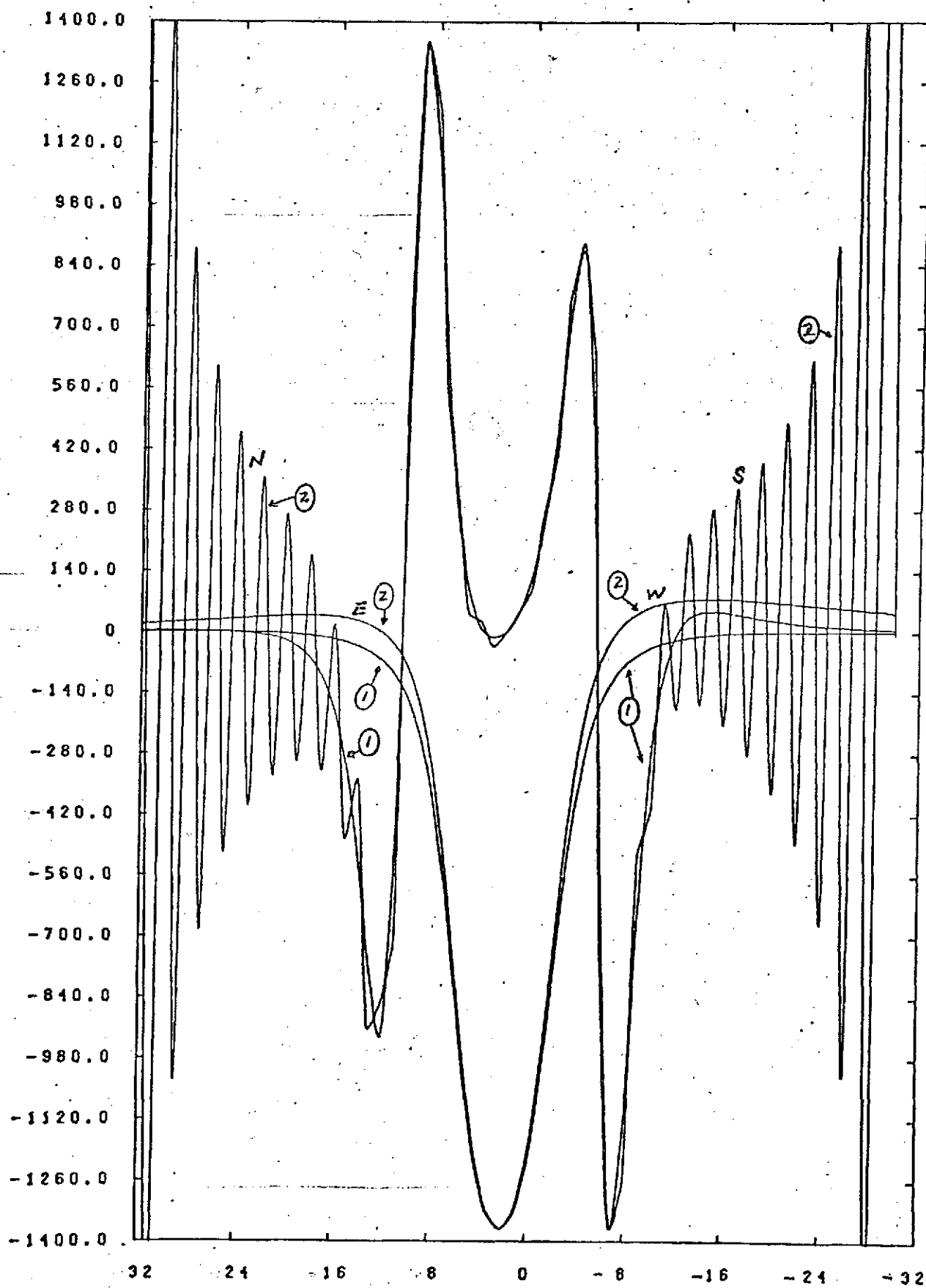


Figure 36

REPRODUCIBILITY OF THE  
ORIGINAL PAGE IS POOR

REPRODUCIBILITY OF THE  
ORIGINAL PAGE IS POOR

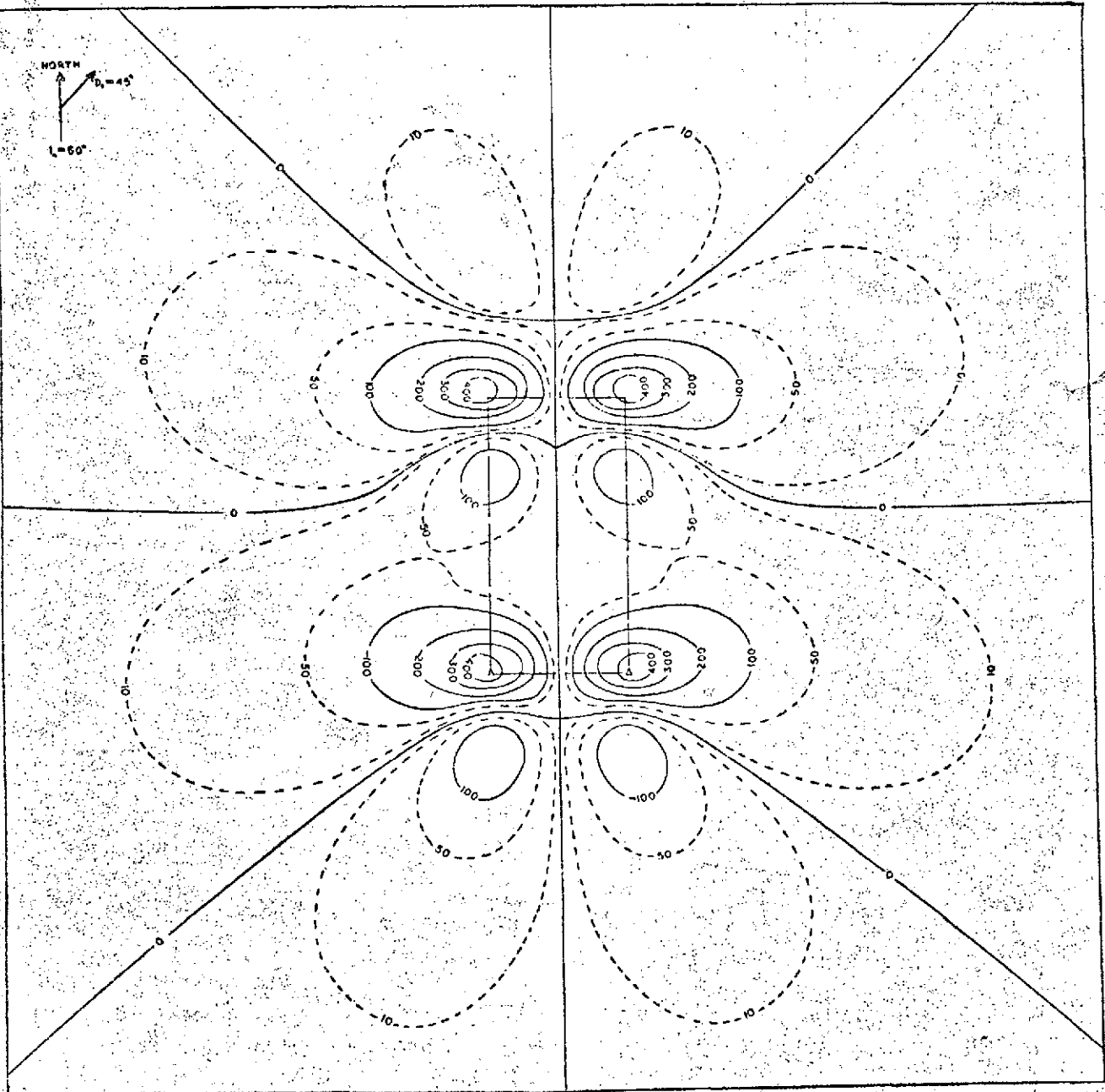


Figure 37

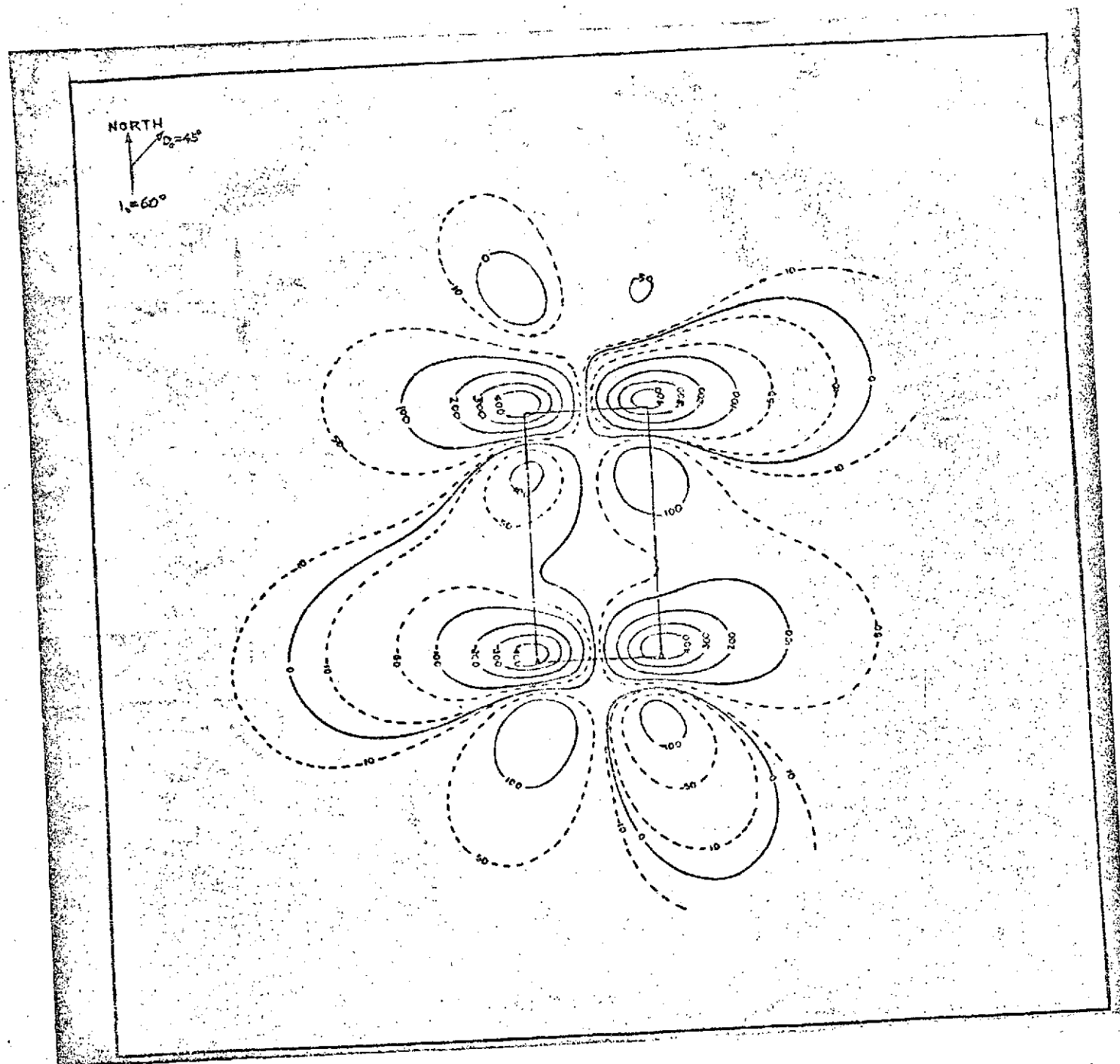


Figure 38

REPRODUCIBILITY OF THE  
ORIGINAL PAGE IS POOR

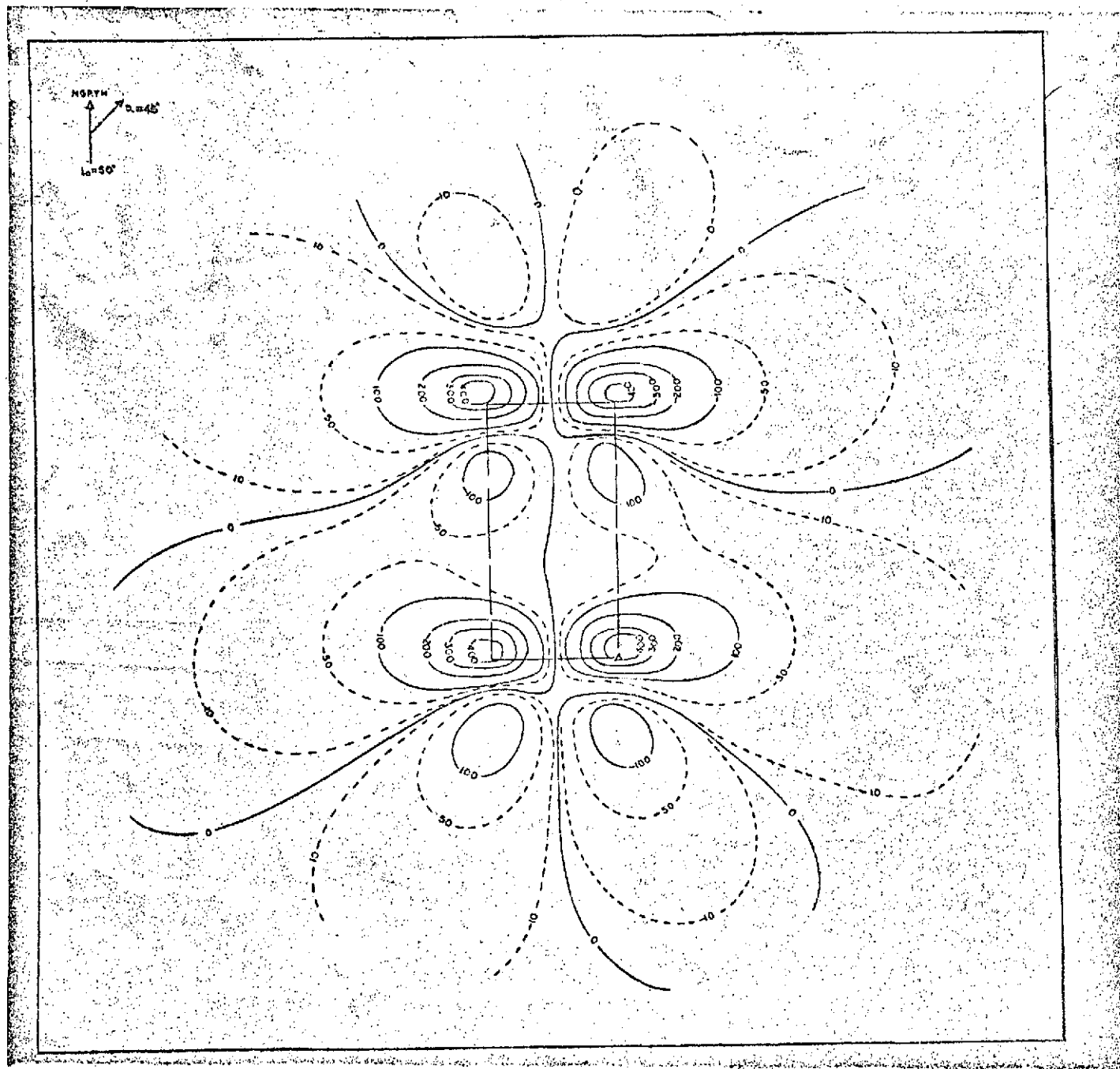


Figure 39

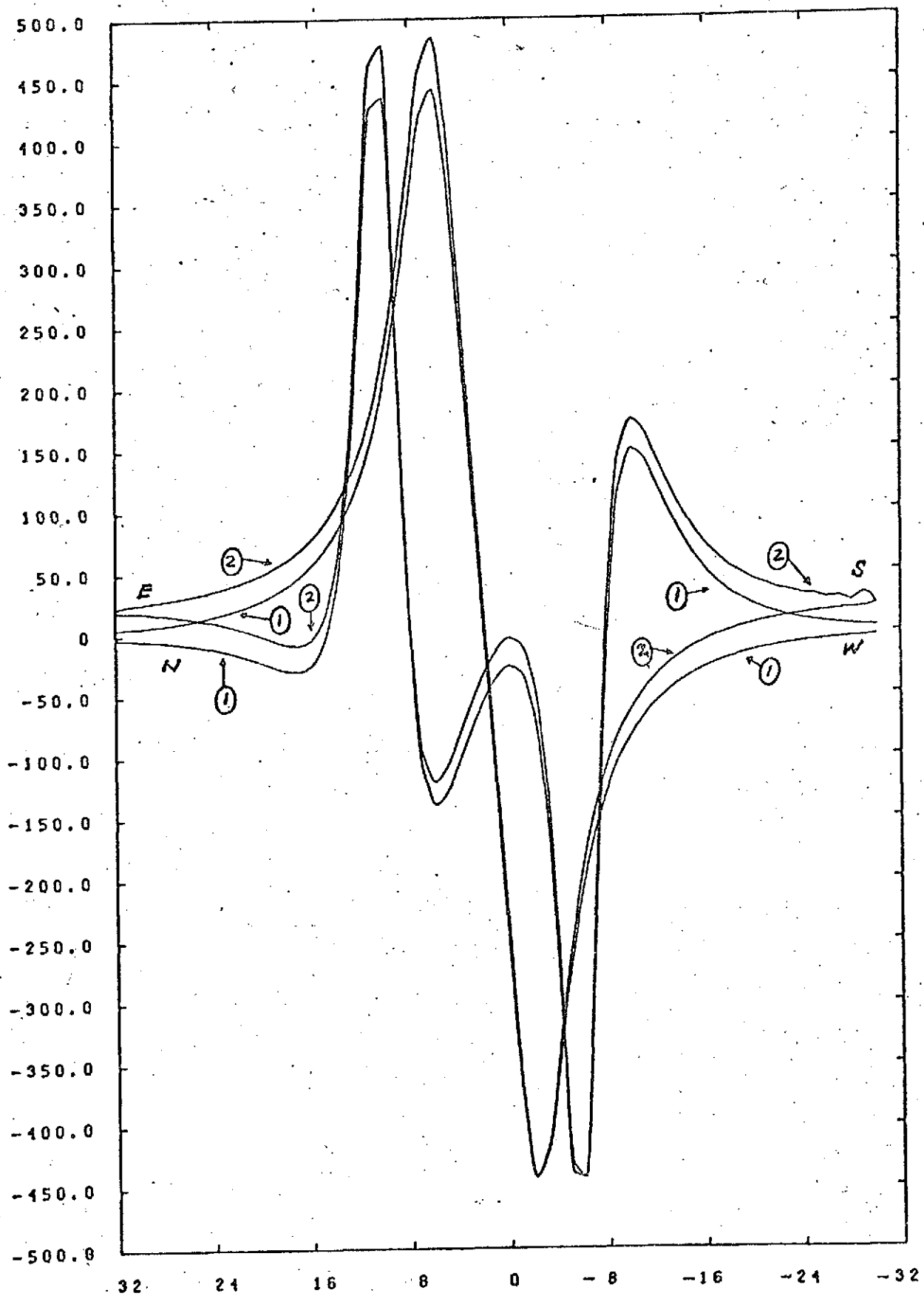


Figure 40

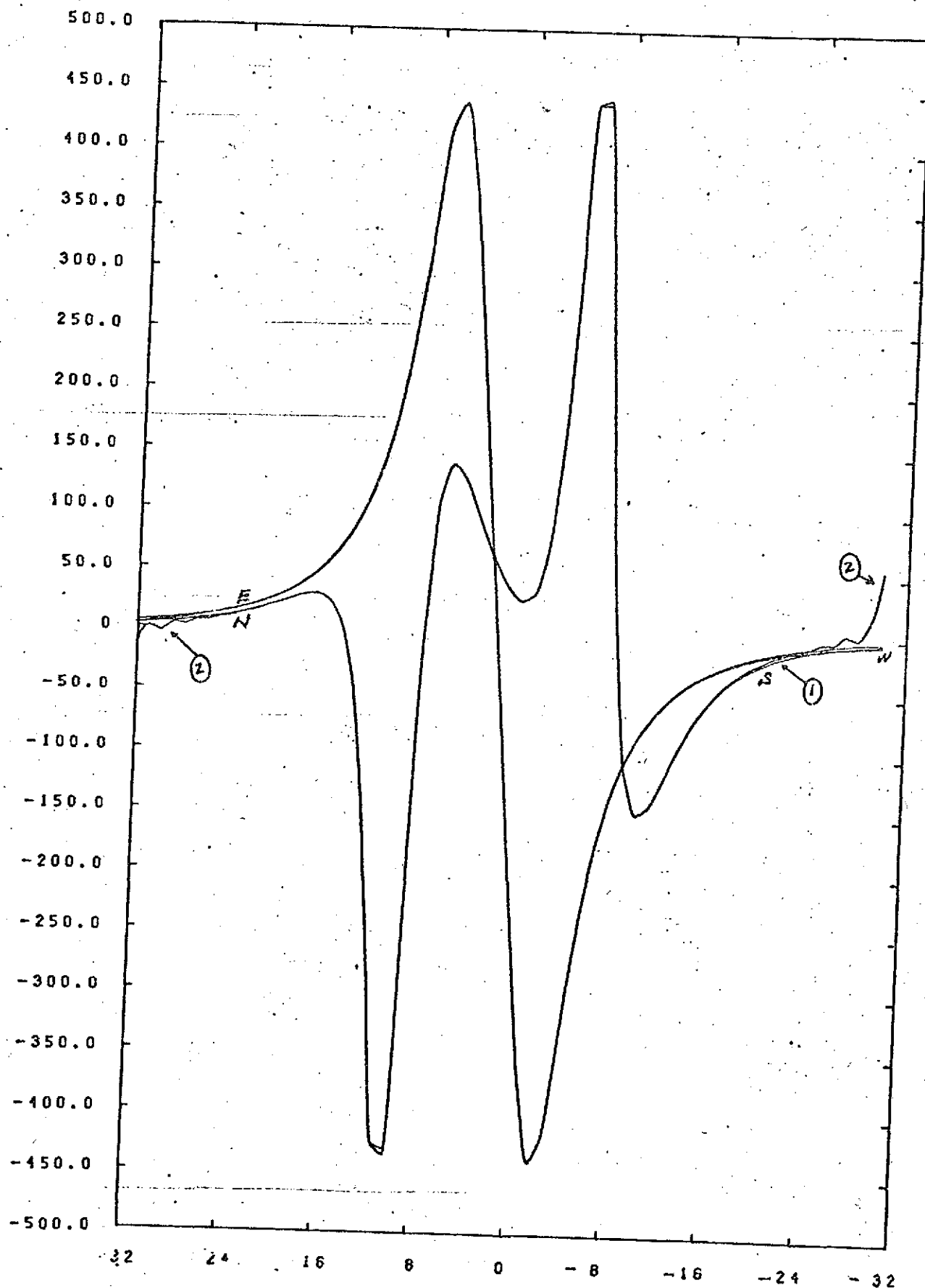


Figure 41

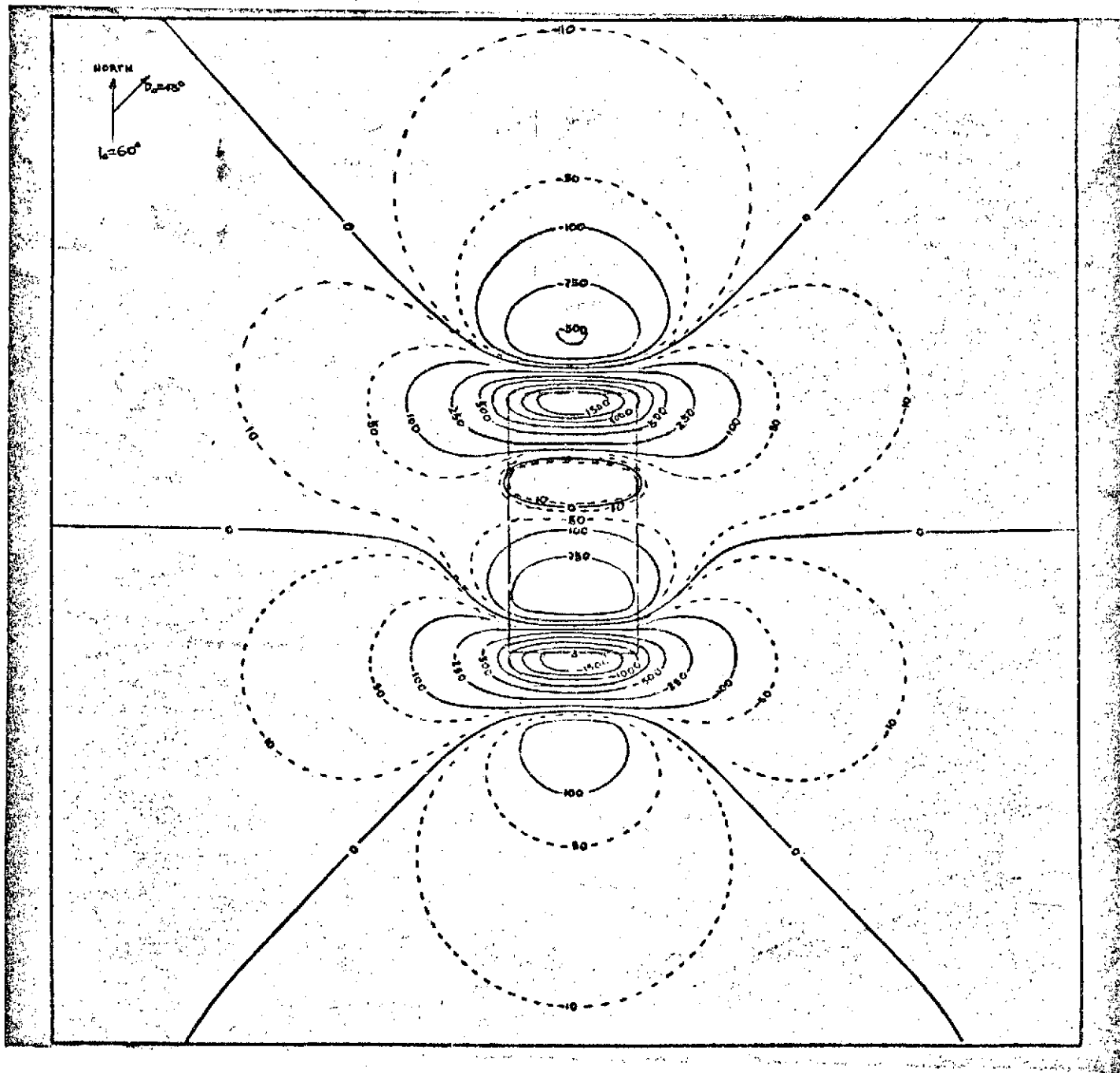


Figure 42



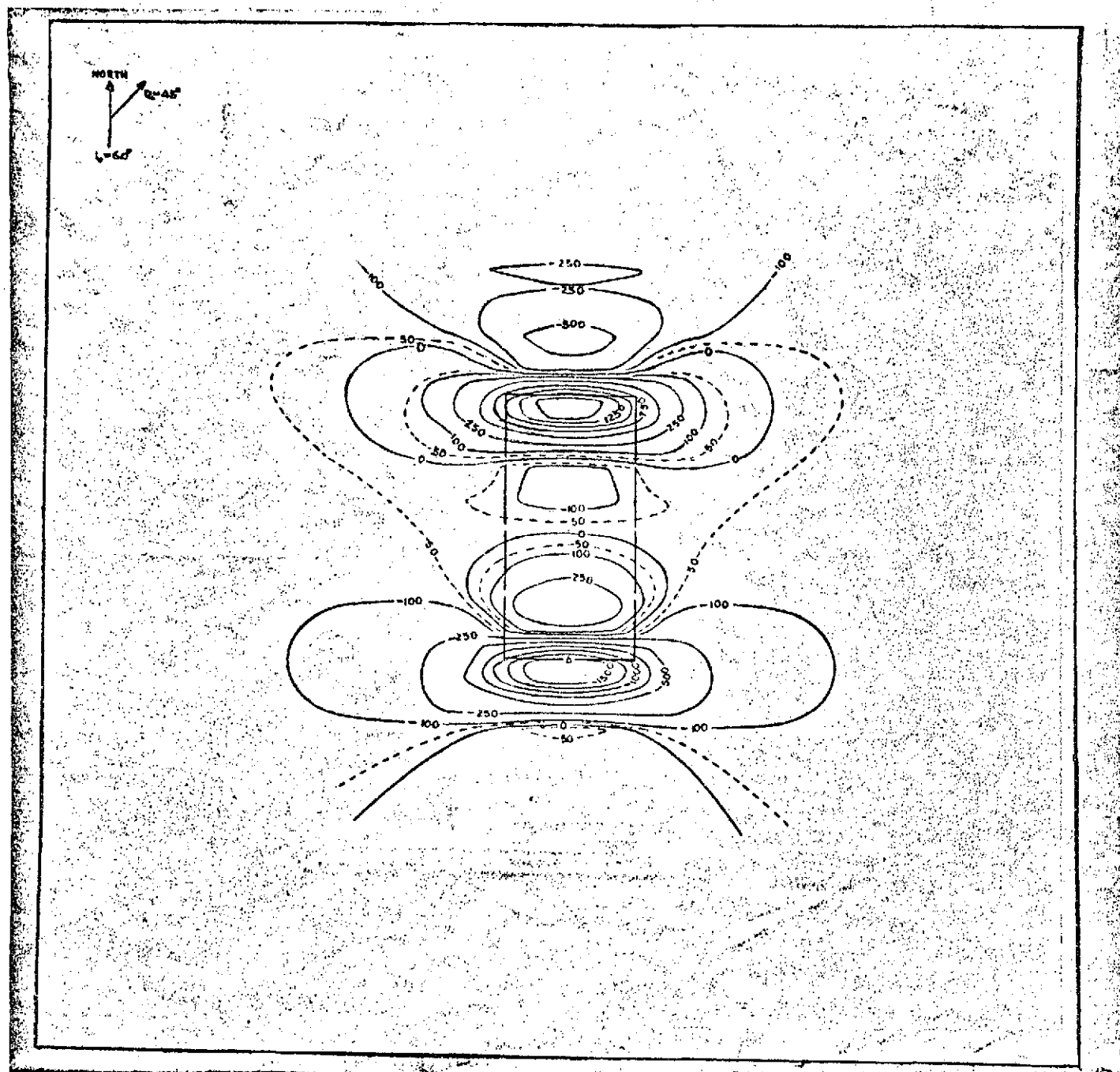


Figure 43

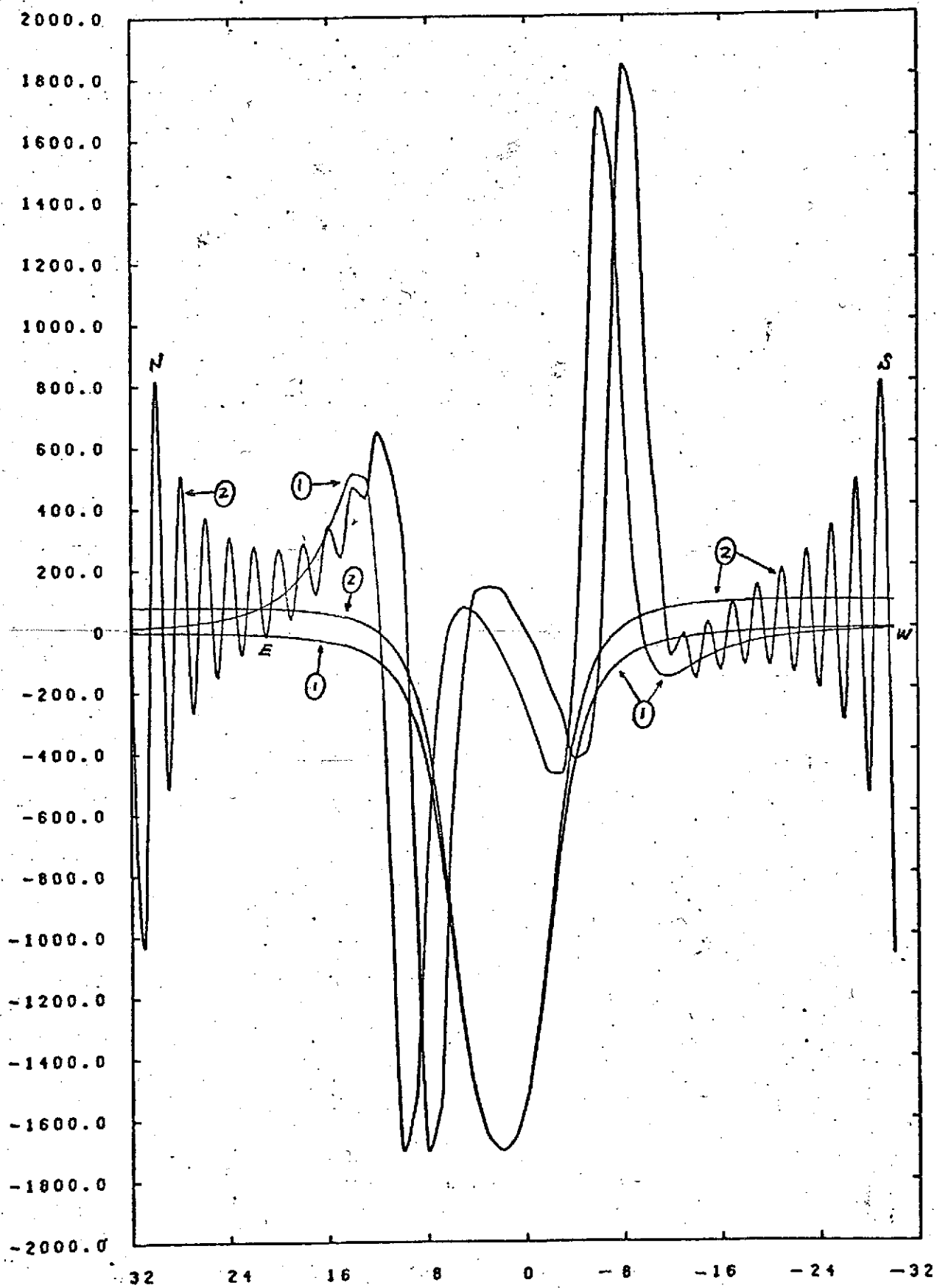


Figure 44

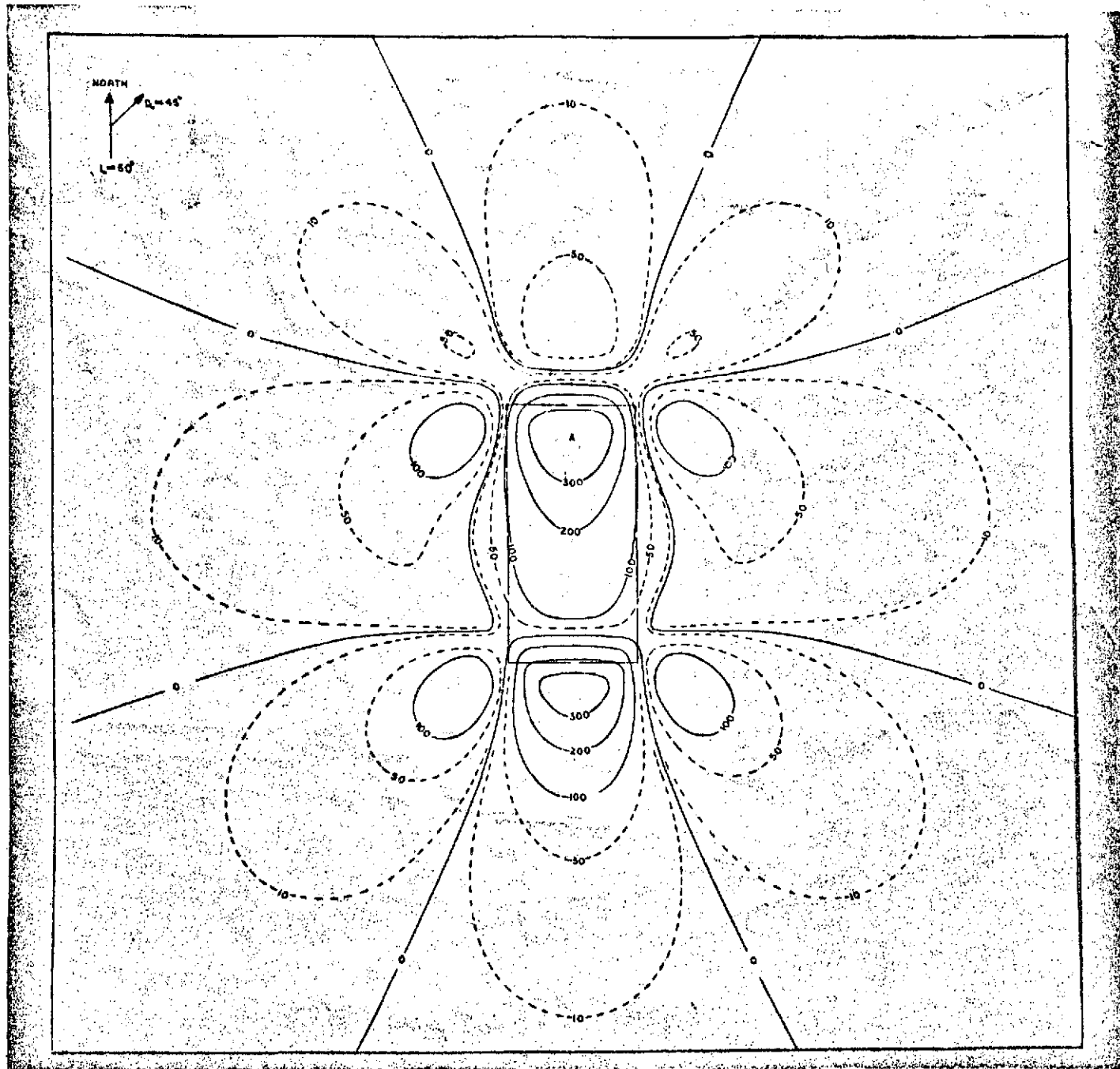


Figure 45

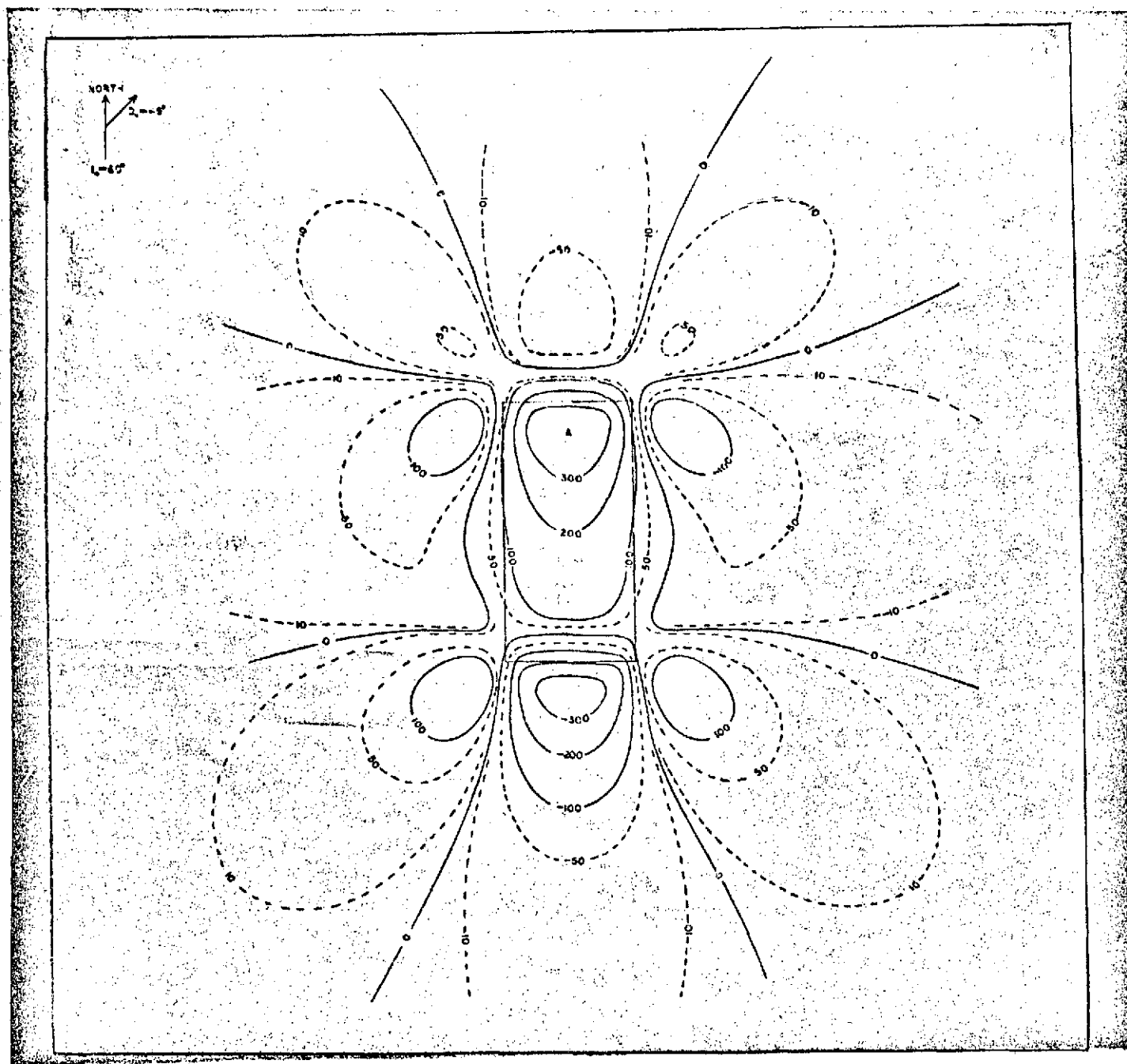


Figure 46

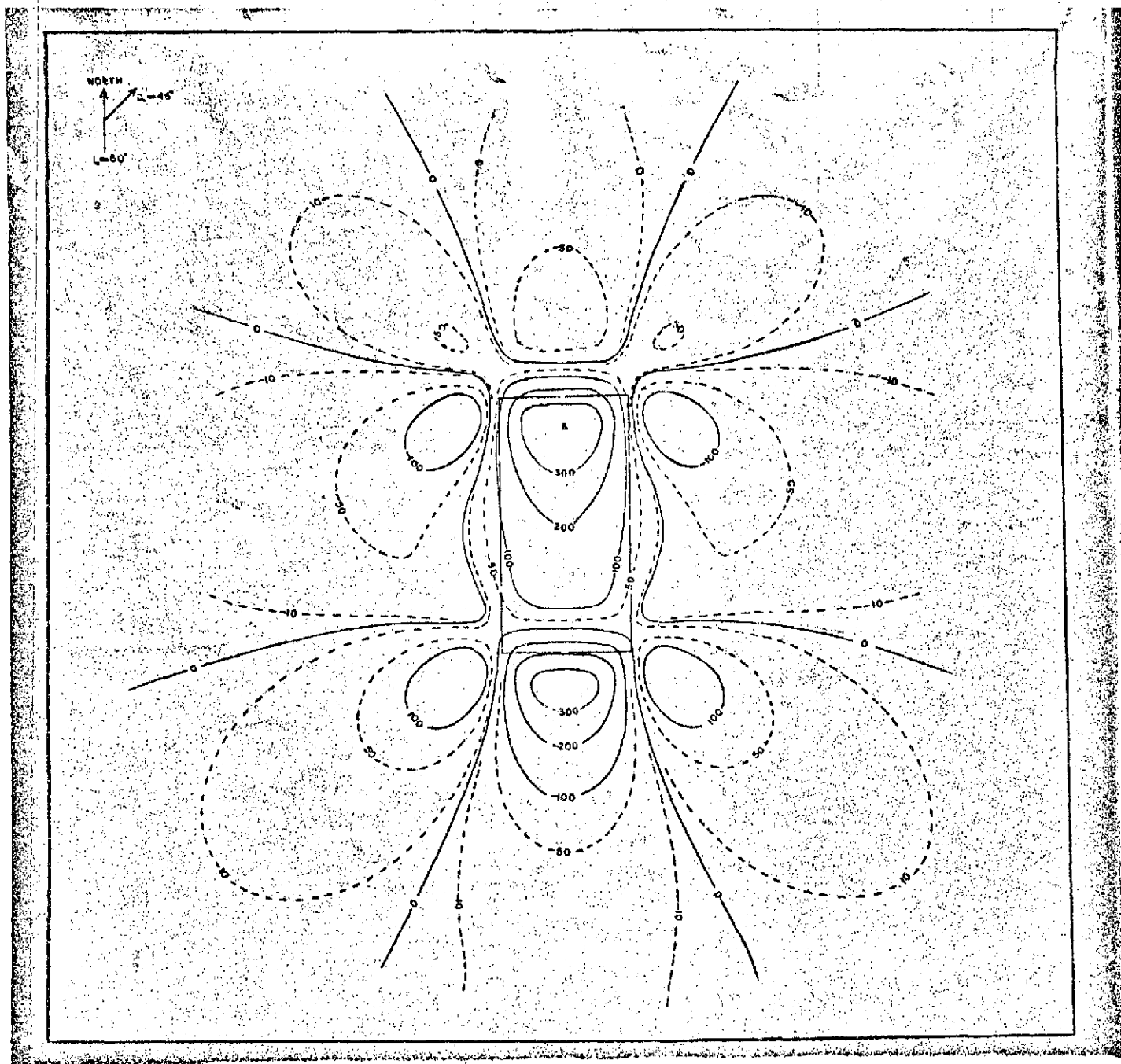


Figure 47

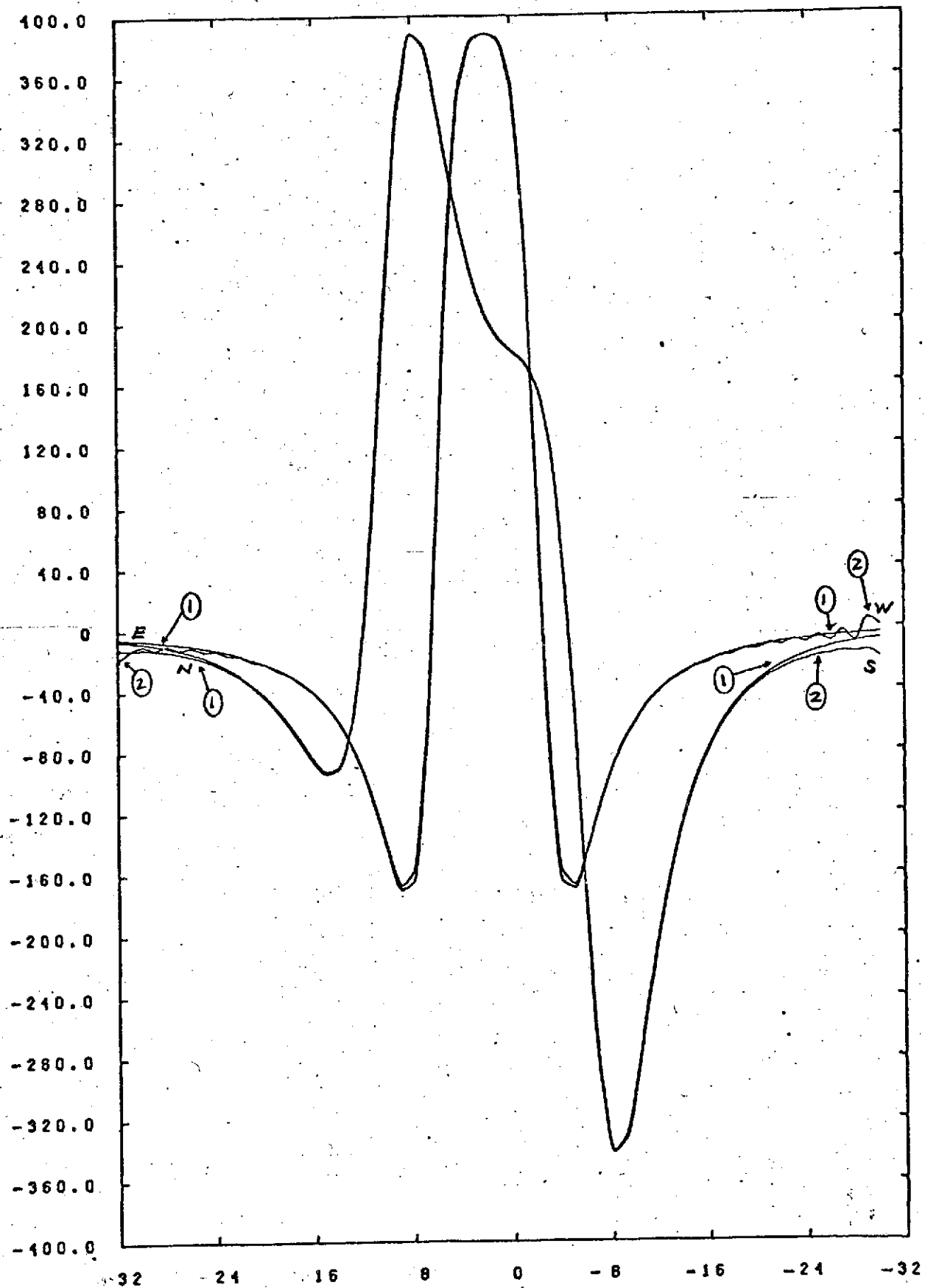


Figure 48

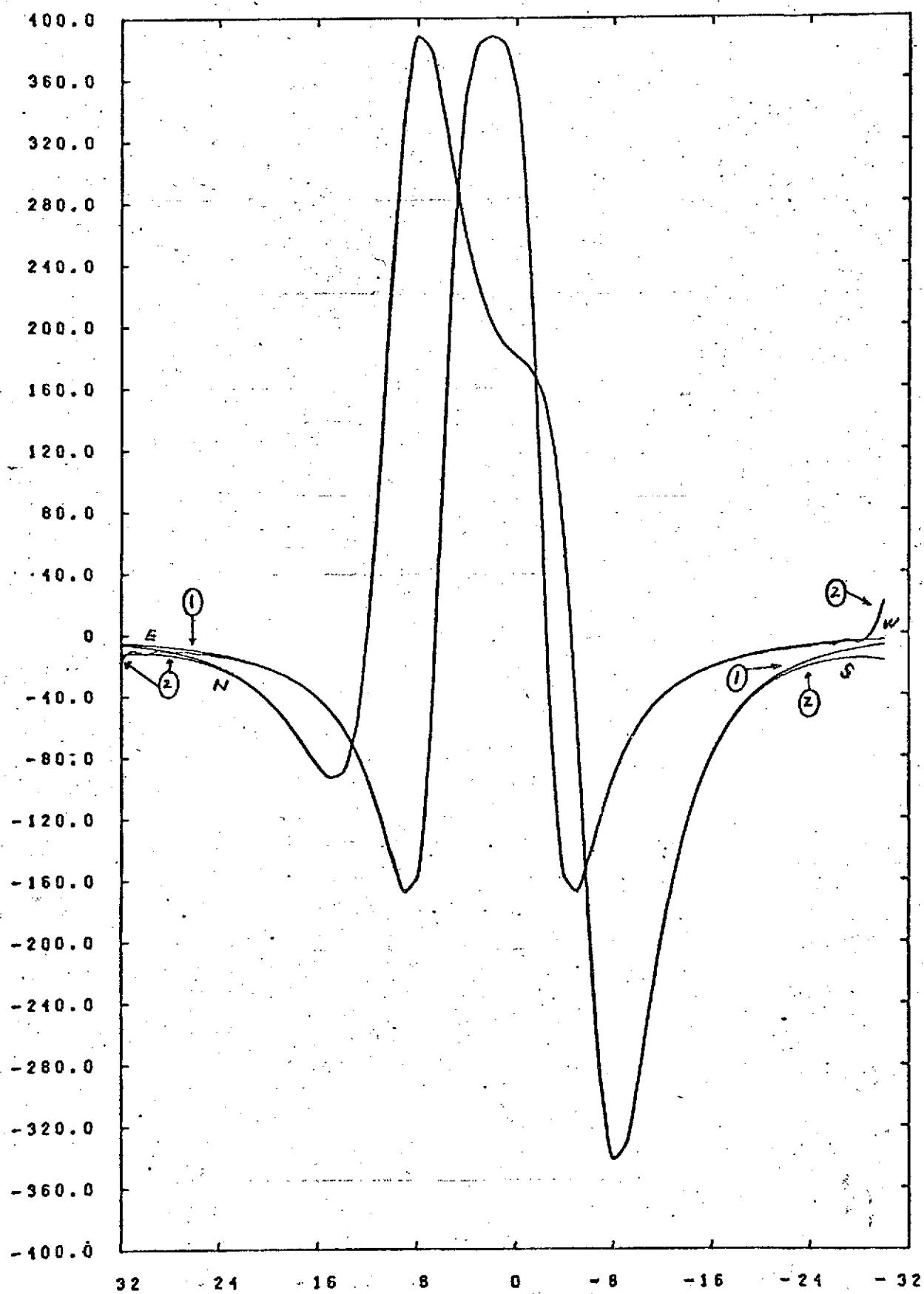


Figure 49

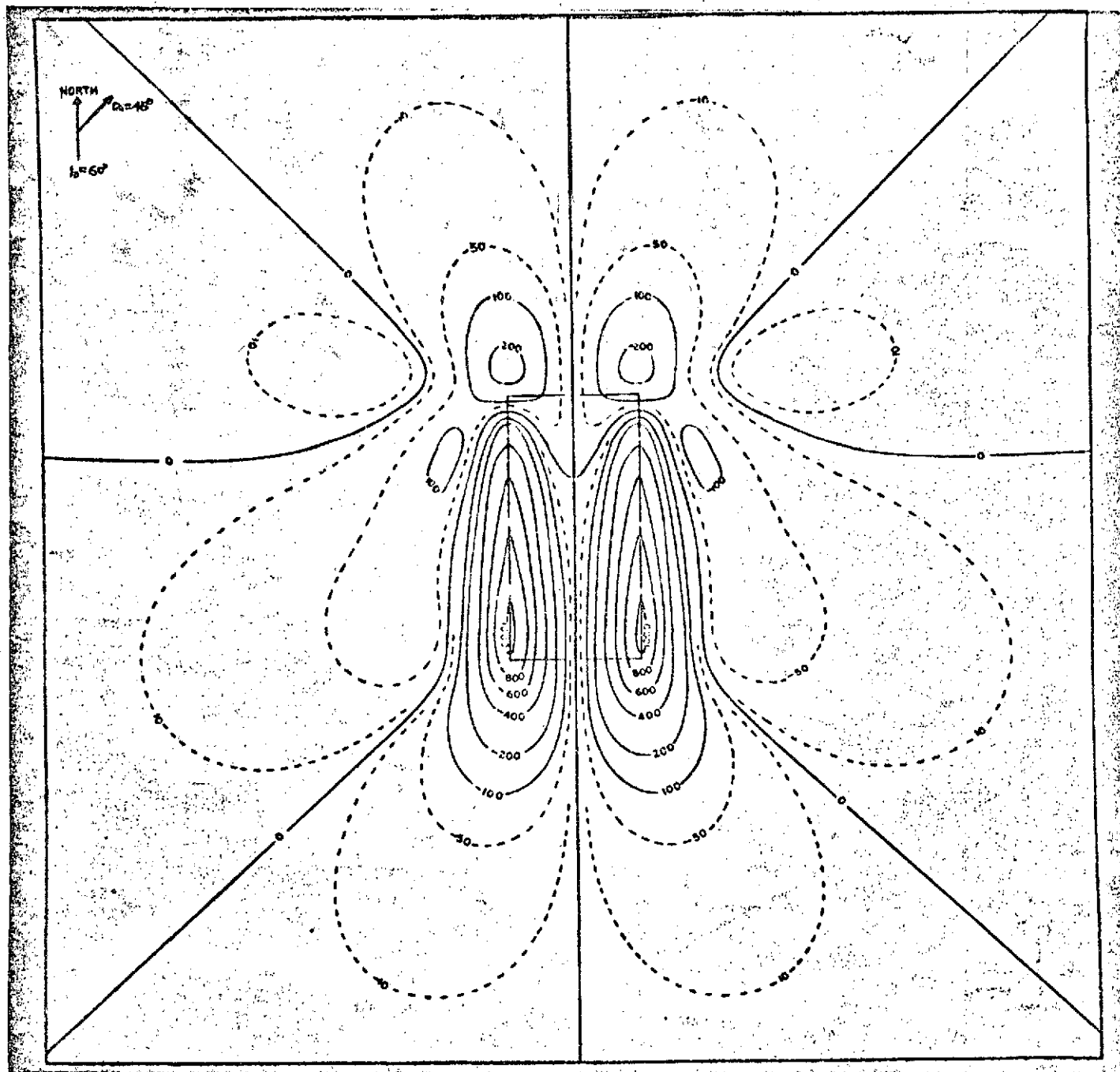


Figure 50



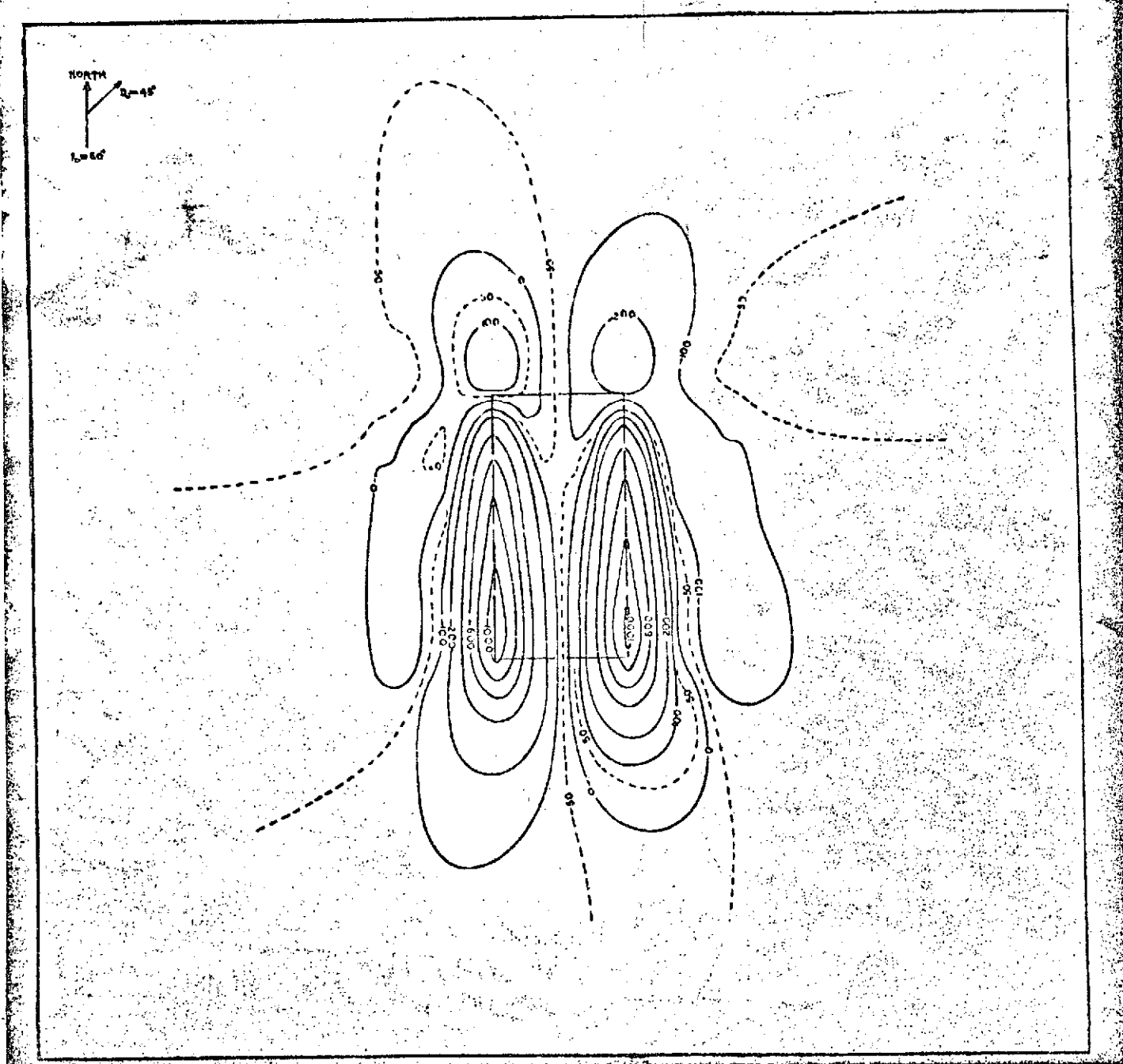


Figure 51

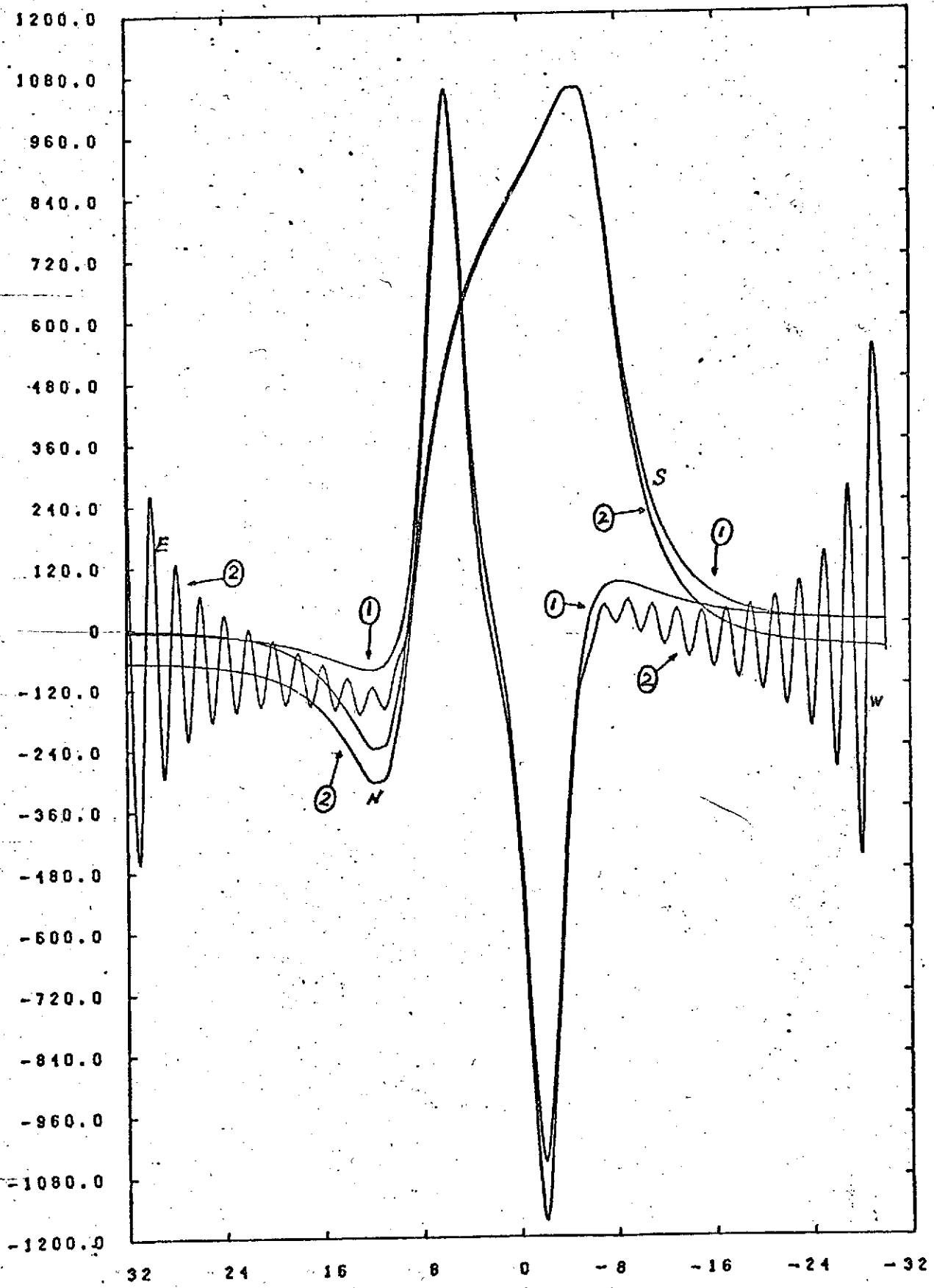


Figure 52

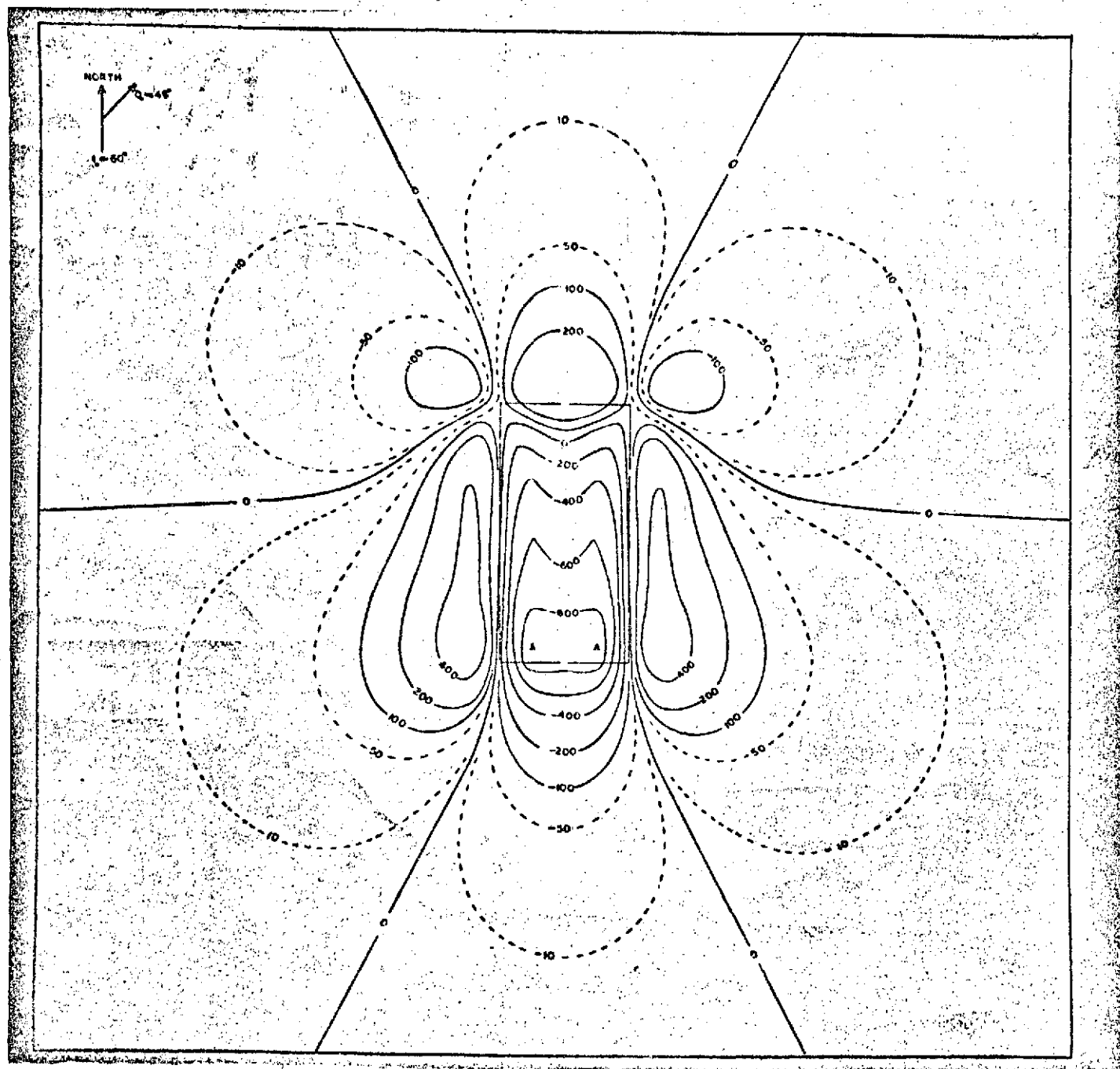


Figure 53

REPRODUCIBILITY OF THE  
ORIGINAL PAGE IS POOR

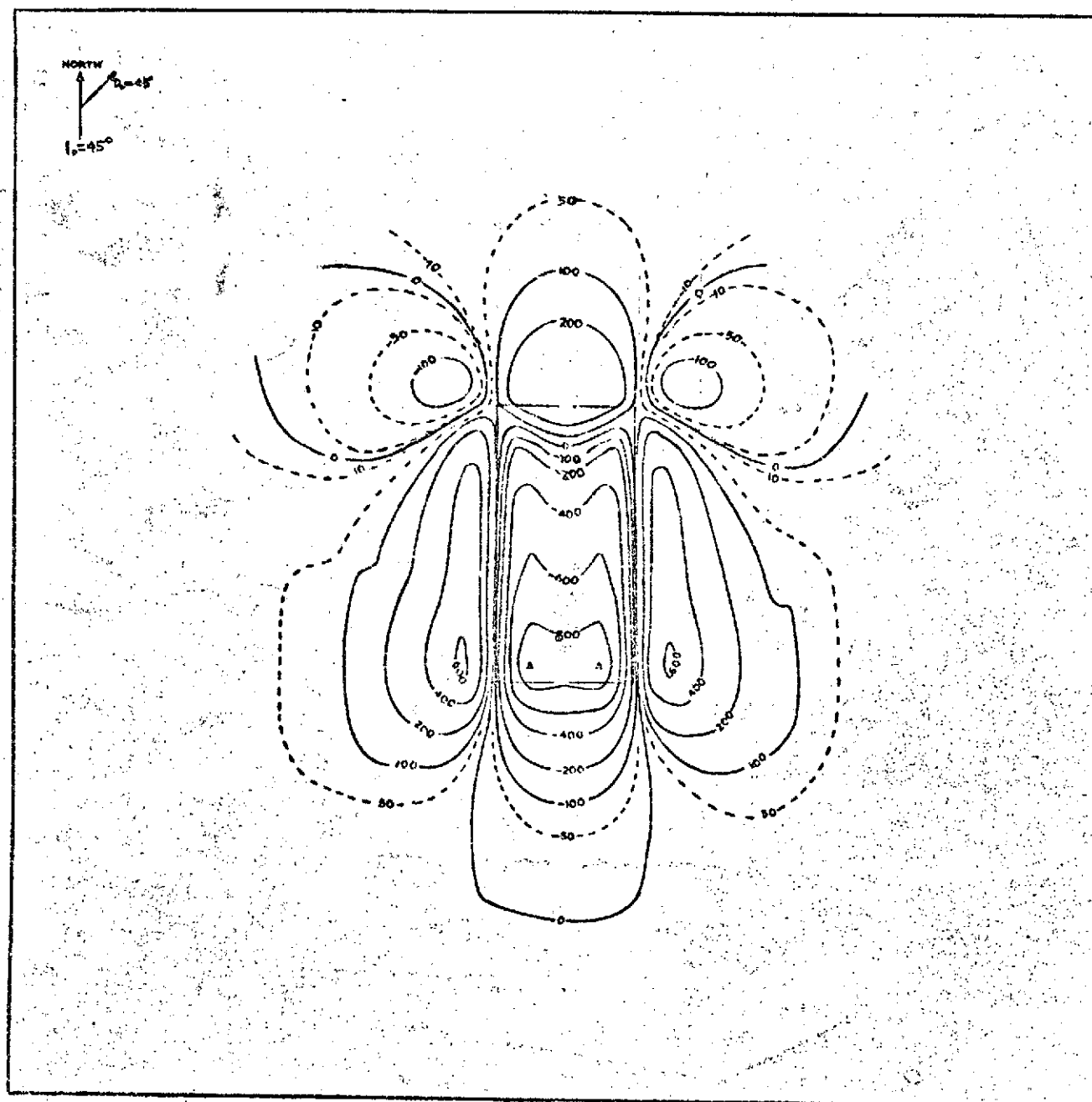


Figure 54

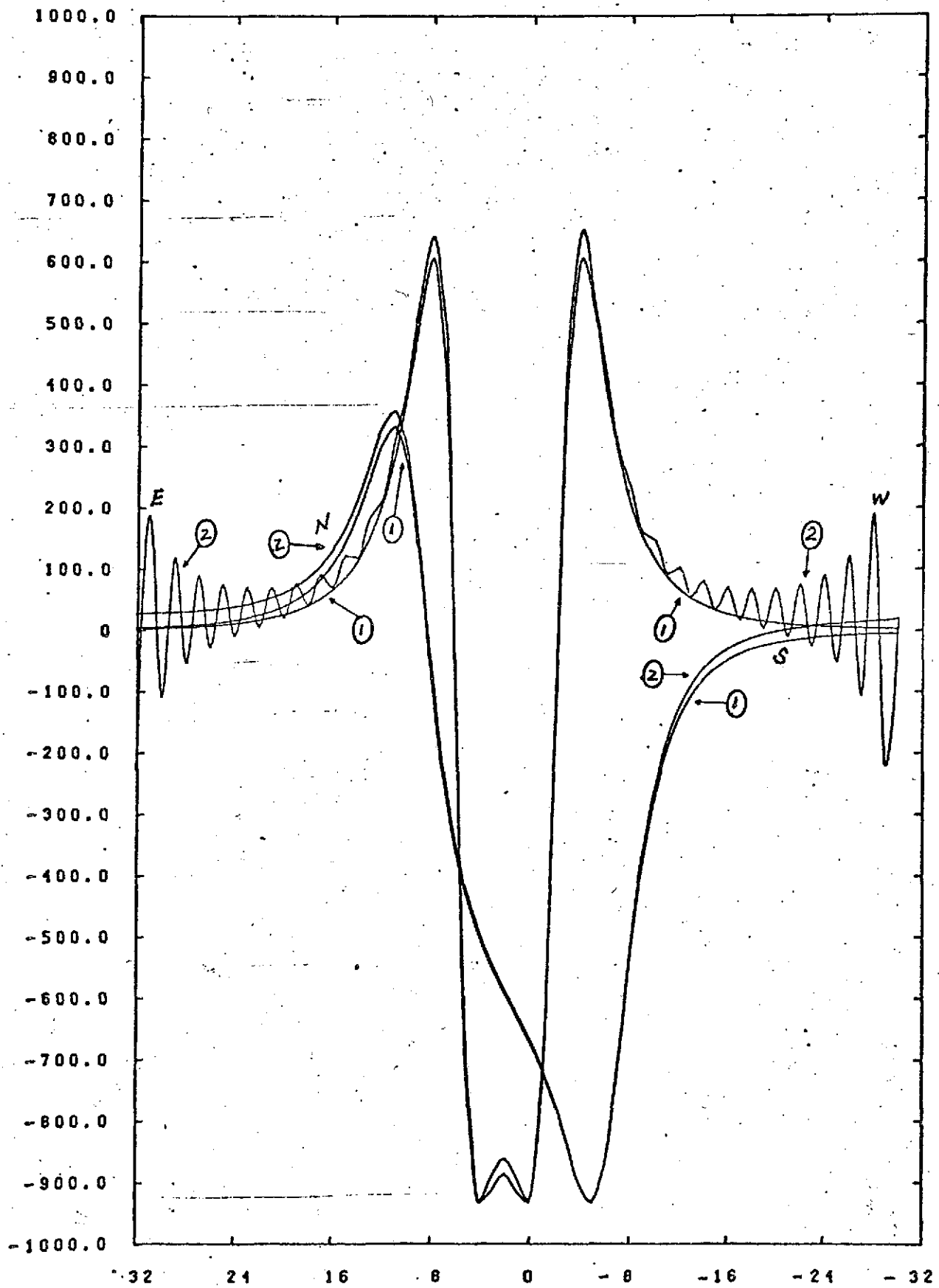


Figure 55

REPRODUCIBILITY OF THE  
ORIGINAL PAGE IS POOR

REPRODUCIBILITY OF THE  
ORIGINAL PAGE IS POOR

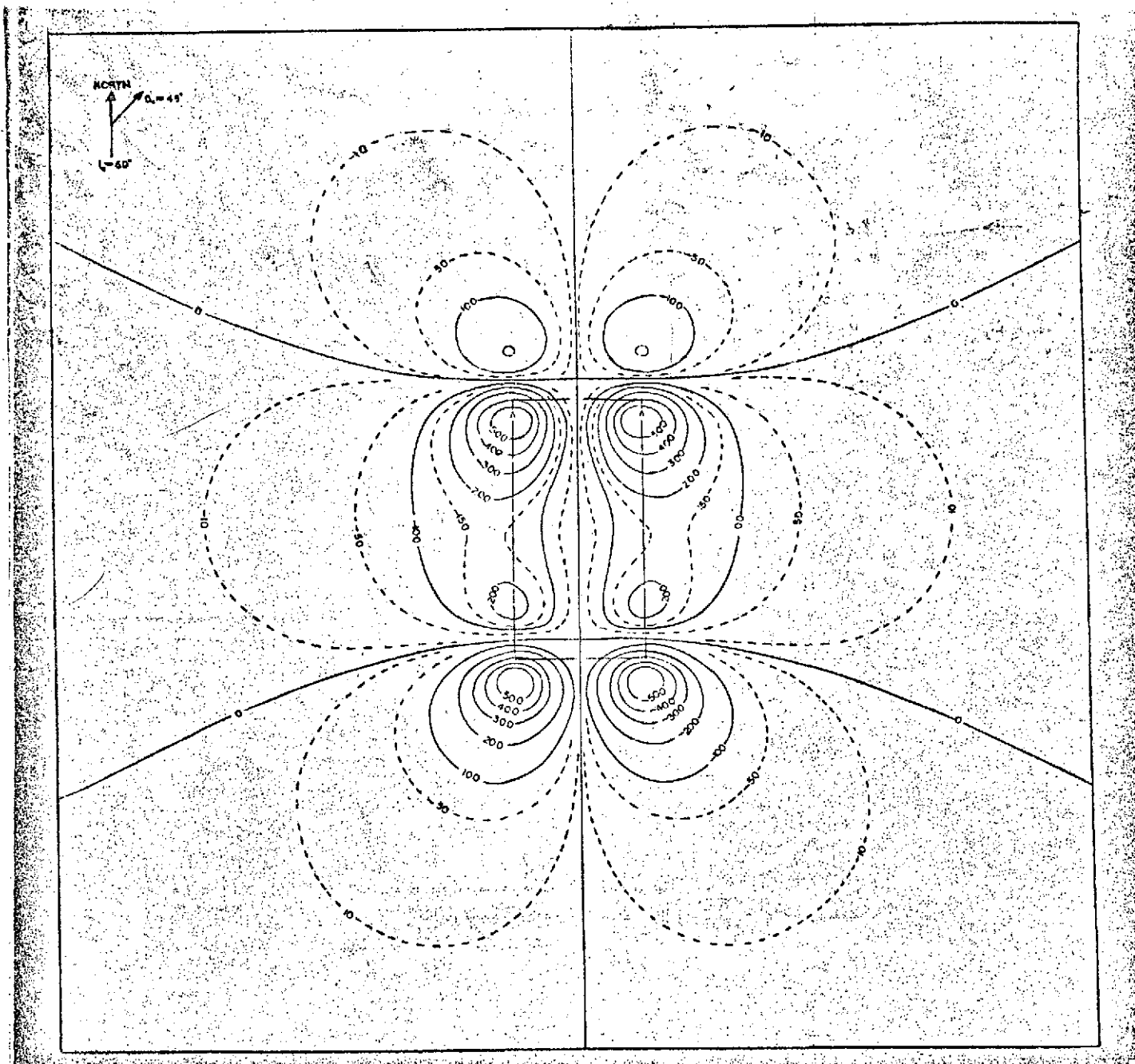


Figure 56

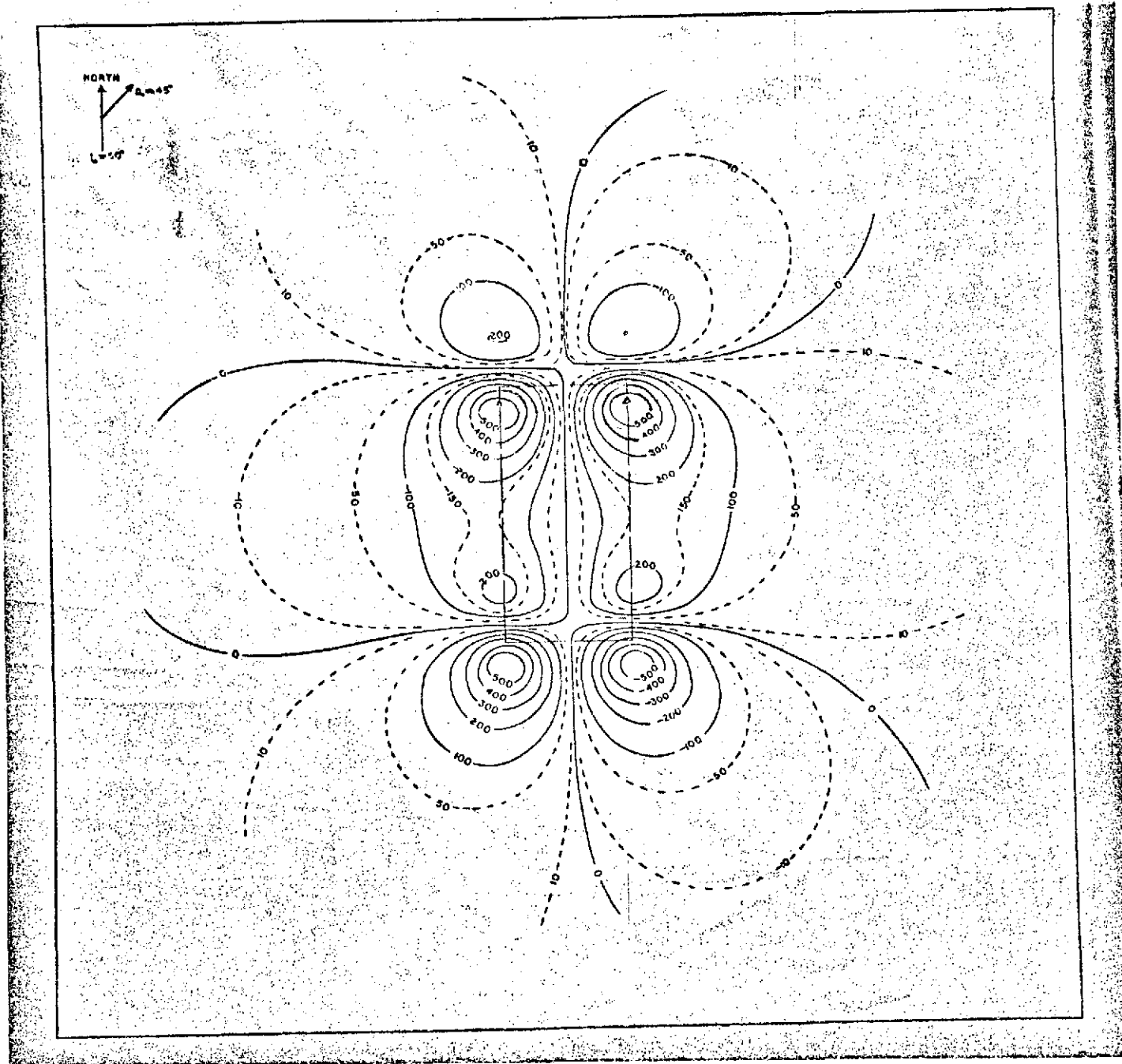


Figure 57

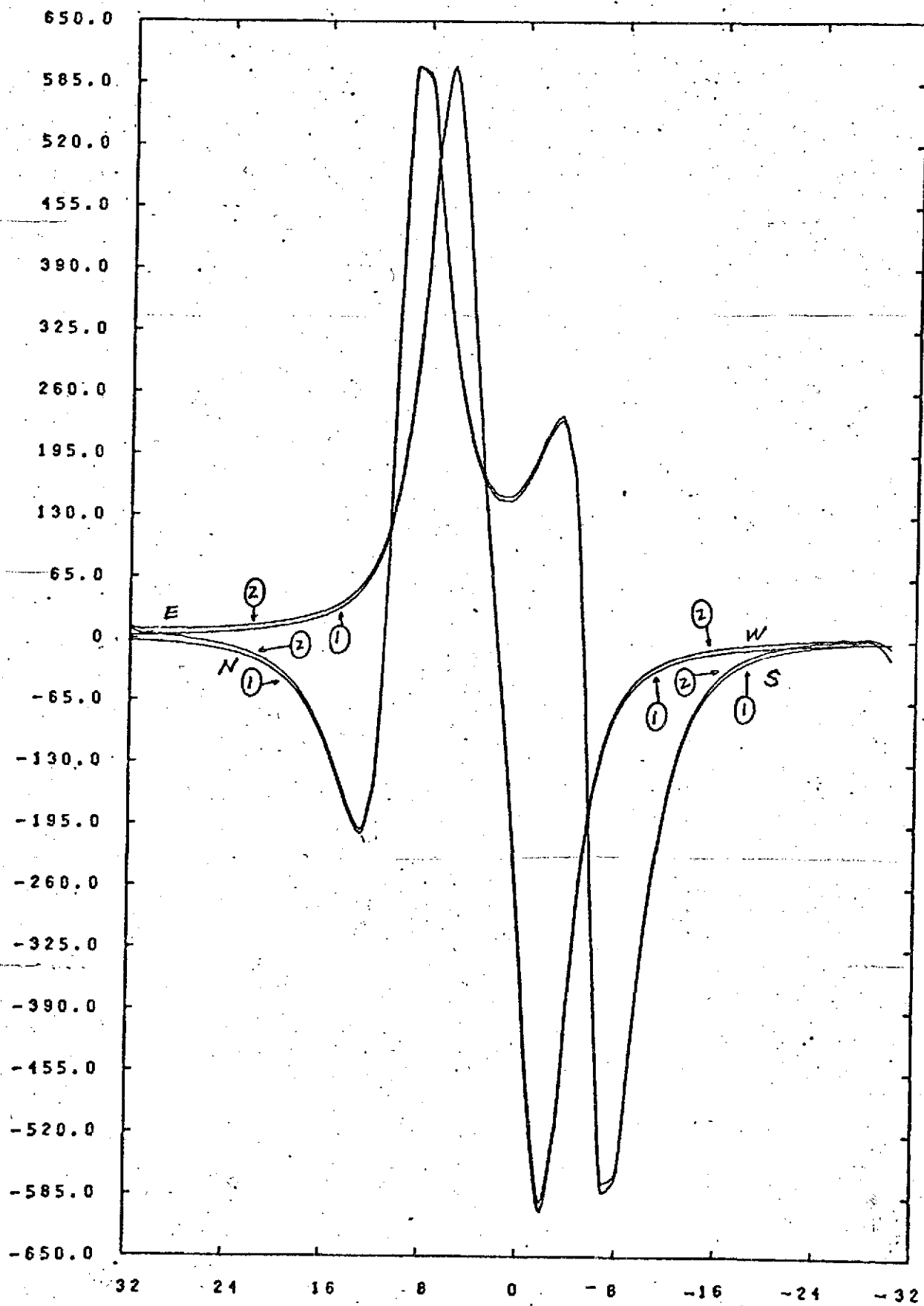
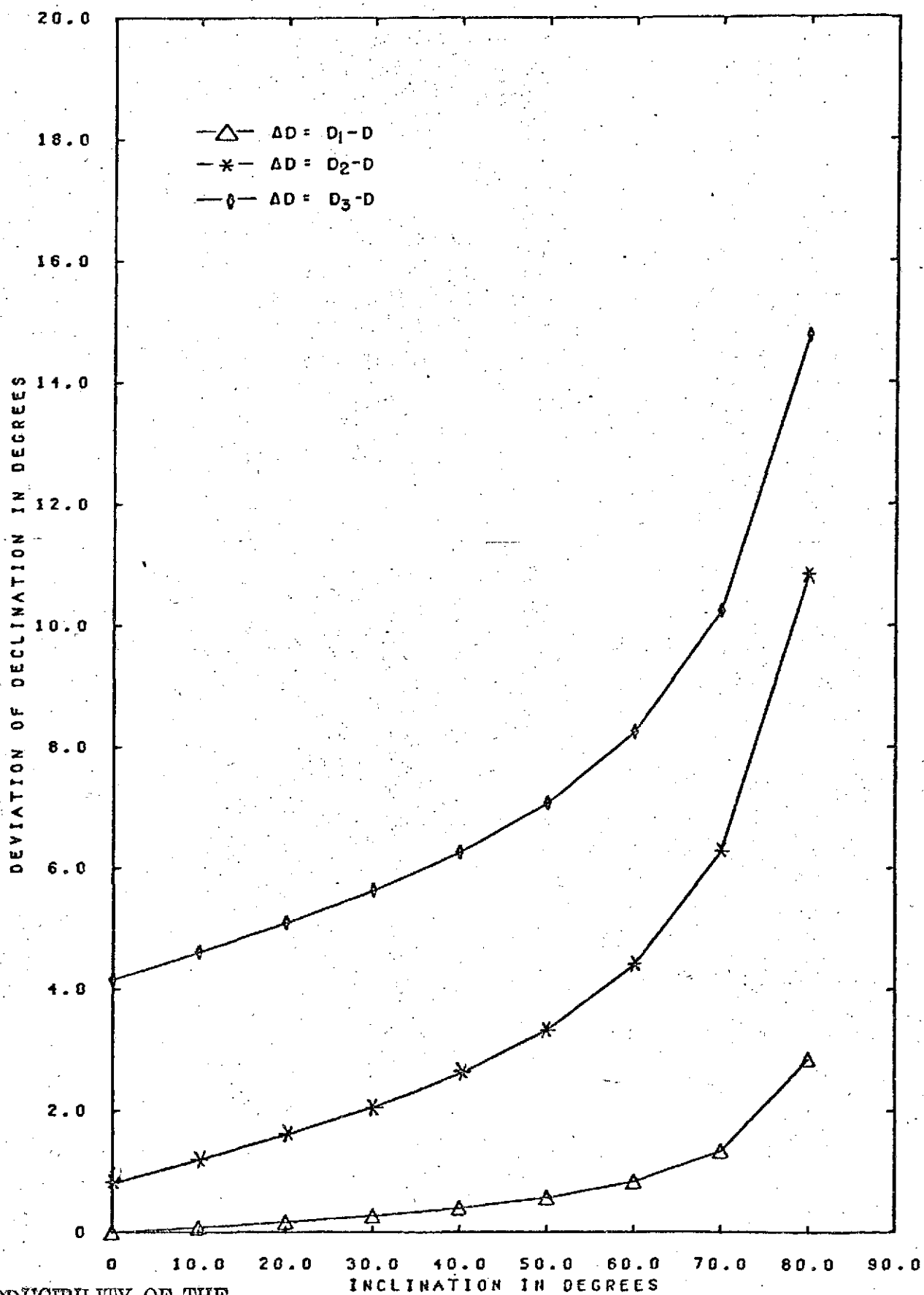


Figure 58

REPRODUCIBILITY OF THE  
ORIGINAL PAGE IS POOR





REPRODUCIBILITY OF THE  
ORIGINAL PAGE IS POOR

Figure 59

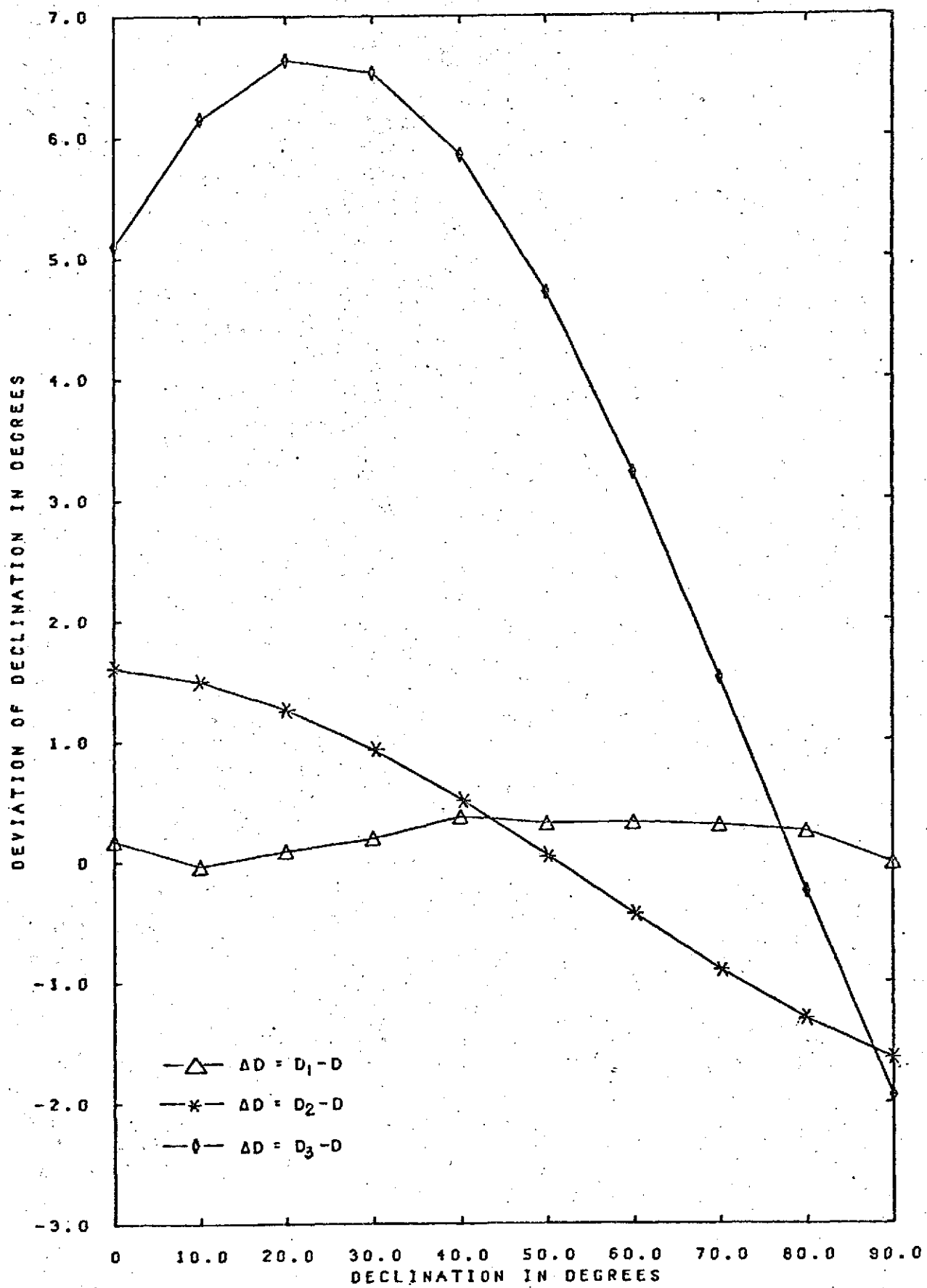


Figure 60

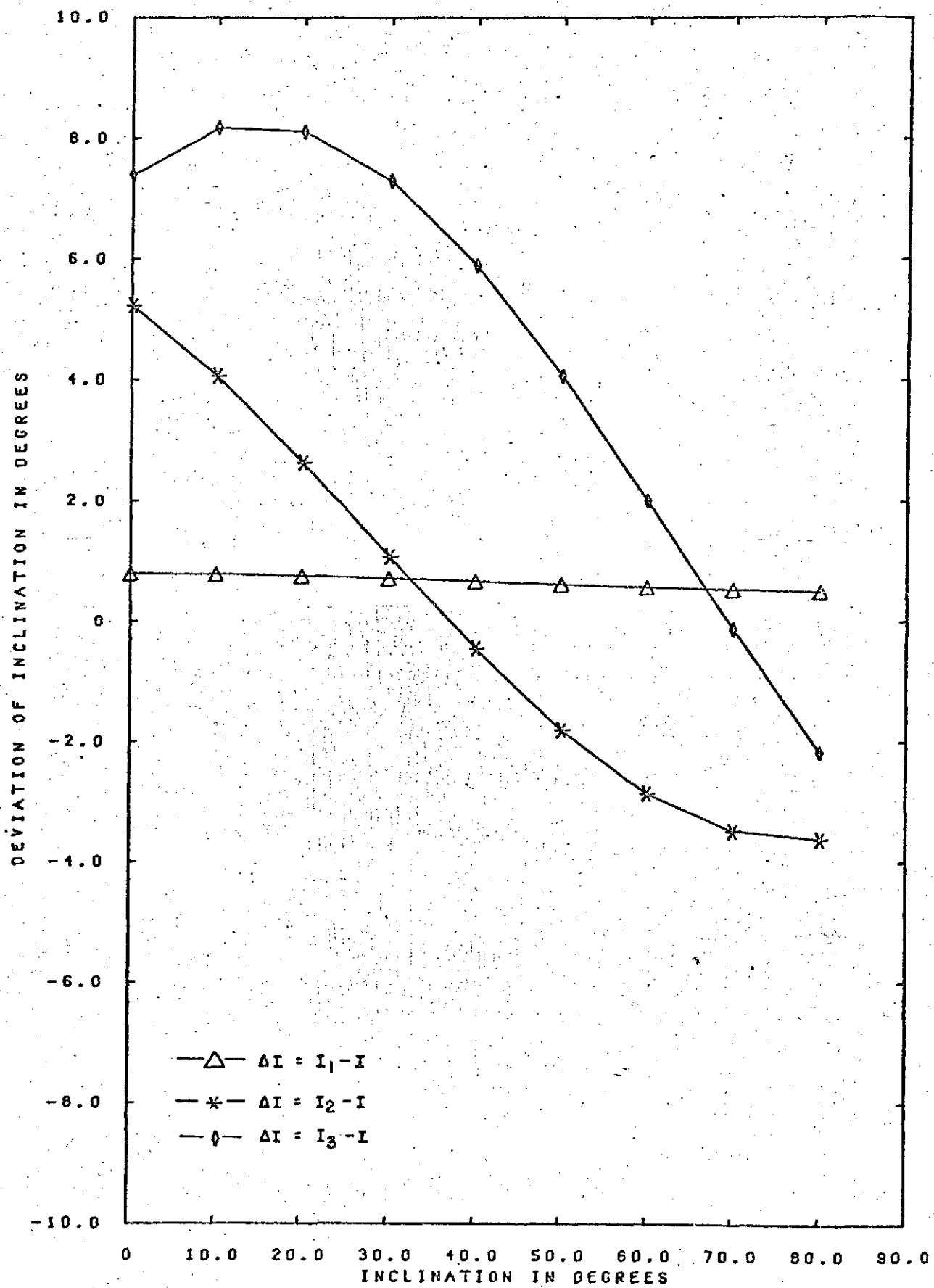


Figure 61.

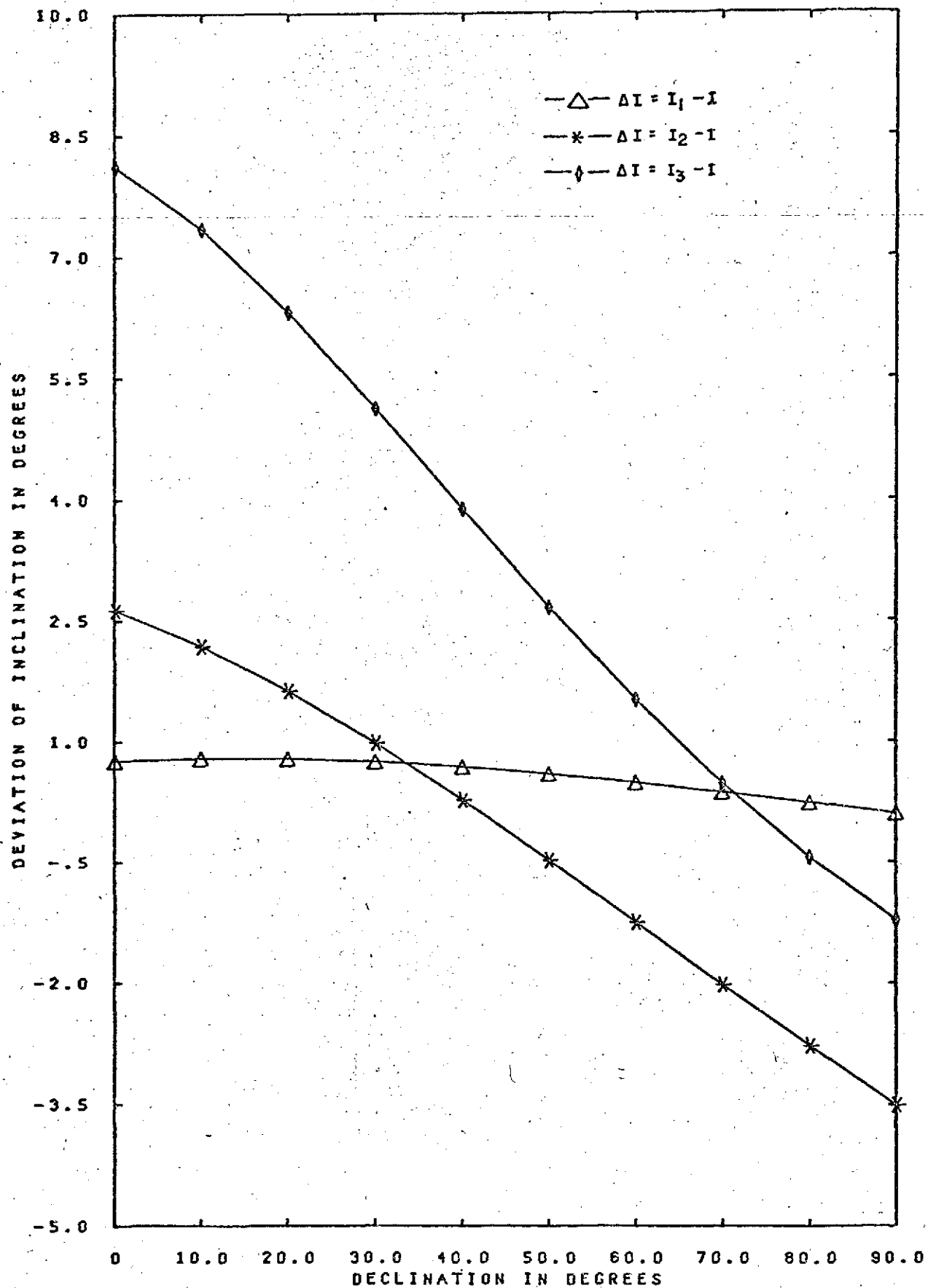


Figure 62